Anion Exchange Membrane optimization

Applying AC electric field to create "Ion highways"

Master MEP thesis
Kalaivanan Shanmugam Anandan

TUDelft

Anion Exchange Membrane optimization

Applying AC electric field to create "Ion highways"

by

Kalaivanan Shanmugam Anandan

to obtain the degree of Master of Science
at the Delft University of Technology,
to be defended publicly on Tuesday May 28, 2024 at 01:30 PM.

TUDelft

Preface

This report is the accumulation of my work in the last part of my academic journey as a student. The two years doing my Master's degree have flown by fast, with fun-filled moments, learning many invaluable skills and broadening my knowledge. I want to thank people who were important to me in the last two years and during my thesis.

First and foremost, I thank Dr. Hanieh Bazyar (main supervisor) and Dr. Thanos Papageorgiou (daily supervisor) for all the support and supervision I received during my thesis. It was an amazing experience for me as I had you both, who always listened to my new ideas and appreciated my curiosity while giving your feedback in leading and doing things during the project. I felt I could always come to you both for any questions or problems during my project.

I thank Dr. David A. Vermaas and Dr. Andres Hunt for being part of my defence committee and reading my report. I thank Aleksandra Kondakova, Stefan ten Hagen, Sietse Kuipers, and Chantal de Zeeuw for helping me a lot by providing training and help with all the technical work related to my thesis. I thank Daan Zwaneveld for sharing the template for this report.

Additionally, I thank my parents for showing me unconditional love and support to study at TU Delft, I am and will always be grateful for that. I thank all my friends who supported me with motivation (and food) throughout the project. Last but not least, I thank Jasna, my lab friend, for always supporting me throughout my thesis.

Kalaivanan Shanmugam Anandan
Delft, May 2024

Summary

This thesis works on improving the performance of the anion-exchange membrane water electrolysis process. The main limitations of this process were analysed, and improvement in ion conductivity appeared to be a viable research gap. This led to the main research question of improving the conductivity of anion-exchange membranes (AEM) by applying an alternating current electric field during AEM casting. The polymer AEMs were cast using a doctor blade setup where the parameters such as voltage, frequency and waveform were varied.

The electrochemical data of the membranes were obtained by doing ion conductivity, cyclic voltammetry (CV) and Electrochemical Impedance Spectroscopy (EIS) to determine the electrolyser performance. Finally, the membranes were characterised using mechanical, chemical, thermal and morphology techniques to measure the stability of the pristine and electrically aligned membranes.

The results show that applying a higher energy through high voltage, frequency or waveform aligned the polymer and gave a high hydroxyl ion (OH^-) conductivity. The final conductivity of the electrically aligned polymer increased by 300%. The ideal AC voltage to align the PCAP polymer is 1.6 V, 5000 Hz and square waveform.

After noticing an increase in electrochemical performance, the results from the characterisation techniques showed a slight decrease in mechanical stability. The chemical stability of the AEMs remained constant whereas the thermal degradation of the aligned membranes accelerated with increasing energy applied during casting.

Contents

Nomenclature

Abbreviations

#	Definition	#	Definition
AEM	Anion Exchange Membrane	LCOE	Levelized cost of electricity
AEMWE	Anion Exchange Membrane Water Electrolysis	LH2	Liquid Hydrogen
AFM	Atomic Force Microscopy	LOHC	Liquid Organic Hydrogen Carriers
AWE	Alkaline Water Electrolysis	LSTS	Lab Scale Testing System
BESS	Battery Energy Storage Systems	LSV	Linear Sweep Voltammetry
CAES	Compressed Air Energy Storage	ME	Modifying ElectricField Strength
CAPEX	Capital Expenditure	MEA	Membrane Electrode Assembly
CCM	Catalyst-Coated Membrane	MF	Modifying Frequency
CCS	Catalyst-Coated Substrate	MW	Modifying Waveform
CO2	Carbon Dioxide	OER	Oxygen Evolution Reaction
CP	Chrono Potentiometry	OPEX	Operational Expenditure
CV	Cyclic Voltammetry	PCAP	Poly (co-Aryl Piperidinium)
DC	Direct Current	PEM	Proton Excahnge Membrane
DI	Deionized	PEMWE	Proton Exchange Membrane Water Electrolysis
DMA	Dynamic Mechanical Analysis	PFSA	Perfluorosulfonic Acid
DMP	Di-Methyl Piperidinium	PHS	Pumped Hydropower Storage
DMSO	Dimethyl Sulfoxide	POP	Porous Organic Polymers
DSC	Differential Scanning Calorimetry	PSA	Pressure Swing Adsorption
DTG	Derivative Thermogravimetry	PTL	Porous Transport layer
EIS	Electrochemical Impedance Spectroscopy	QPPO	Quaternized Polyphenylene Oxide
ES	Energy Storage	R&D	Research and Development
FT-IR	Fourier-Transform Infrared Spectroscopy	RCM	Reinforced Composite Membranes
GDL	Gas Diffusion Layer	RE	Renewable Energy
GDP	Gross Domestic Product	RMS	Root Mean Squared
GHG	Green House Gases	RT	Room Temperature
HBE	Hydrogen Binding Energy	SPPO	Poly(2,6-dimethyl-1,4-Phenylene Oxide)
HER	Hydrogen Evolution Reaction	SR	Swelling Ratio
H-NMR	Proton-Nuclear Magnetic Resonance	TFA	Tri-fluoro Acetic acid
IC	Ion Conductivity	TGA	Thermogravimetric Analysis
IEC	Ion Exchange Capacity	TS	Tensile Strength
KOH	Potassium Hydroxide	UTM	Universal Testing Machine
LCA	Life Cycle Analysis	WAXS	Wide-angle X-ray Scattering

List of Figures

List of Tables

1

Introduction

In this chapter, Section 1.1 introduces the current global climate situation and the need for renewable energy technology. Section 1.2 explains the challenges of growing renewables, the need for storage technologies and their current barriers. Section 1.3 briefly gives an introduction to alternate fuels and the rise of the hydrogen economy. Section 1.4 contains a detailed introduction to the life-cycle of hydrogen and its current status. Finally, the prospects of hydrogen and hydrogen production are given in section 1.5

1.1. The urgent need for Renewable energy

1.1.1. Global warming: History and the consequences

With the advent of the industrial age, demand for products grew rapidly and the spending power of an average human increased worldwide. The birth of large industries pushed the costs down and decreased production time. The discovery of synthetic oil in 1847 by James Young [35] and commercial oil drilling by Edwin Drake in 1859 [36] led to a heavy financial spike in economies worldwide. This marked the beginning of the petroleum era, where the profits created a positive feedback loop that pushed the global economy to be strongly intertwined with the petroleum industries into multiple systems.

Current Global climate situation

Fossil fuels have become an integral part of our everyday life. More than just being used as transportation fuels, they are also used as feedstock in industries for heat, and by reassembling the hydrocarbon chains to simpler products such as paints, plastics, apparel, pesticides, and electronic devices [37]. Industrialisation, added to increasing agricultural productivity [38], led to the increase in the usage of petroleum products along with a strong postwar economy led to exponential population growth globally. These elements include a desire for improved well-being.

Scientists have unanimously agreed that the main cause of global warming is human activity and emissions [39]. Population growth and Gross Domestic Product (GDP) per capita have been identified as the strongest drivers of anthropogenic CO_2 emissions in the last decade. The ever-increasing energy demands due to these drivers have resulted in over-exploitation of oil and oil products.
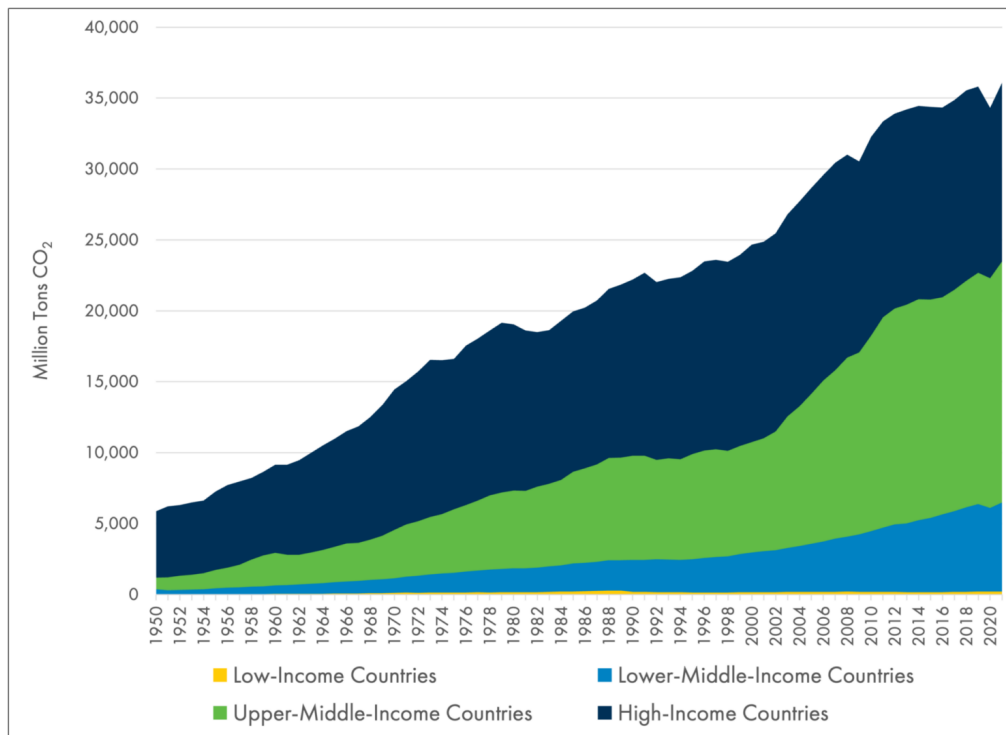
Figure 1.1: CO_2 emissions by Income level, 1950-2021 [1]

The increase in the rate of production and consumption of fossil fuels and their by-products has led to a significant increase in global CO_2 concentration as shown in Fig 1.1. This accumulation of CO_2 in the atmosphere (fig 1.2) has been far above the natural CO_2 recovery rate by the atmosphere. The Copernicus Climate Change Service which is part of the European Centre for Medium-Range Weather Forecasts, determined that 2023 was the "Hottest Year on Record" [40], with temperatures reaching $1.48°$ C above the pre-industrial levels (1850-1900).
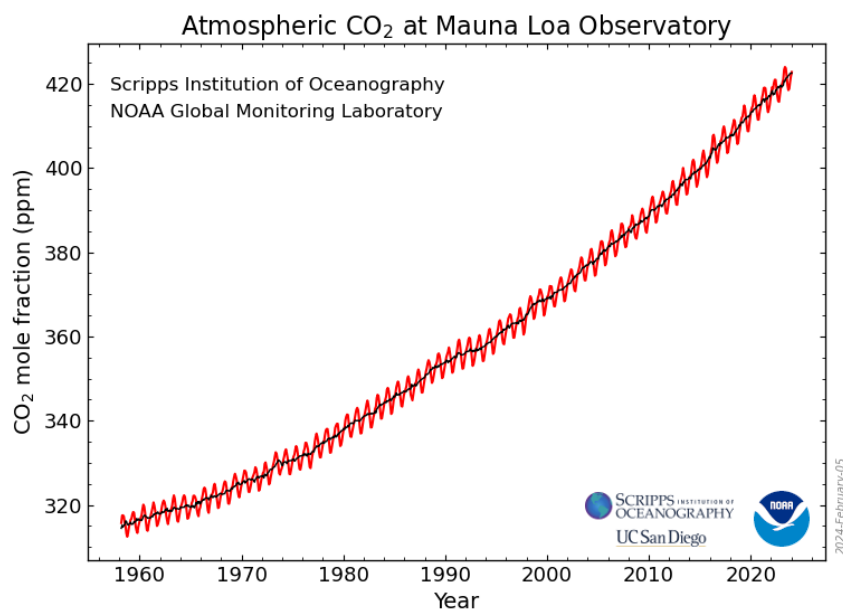
Figure 1.2: Atmospheric CO_2 levels between 1954-2024 [2]
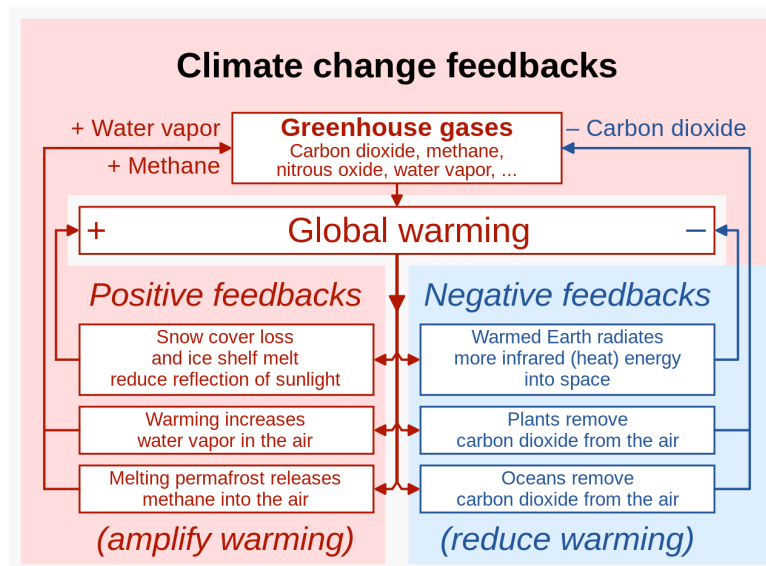
Figure 1.3: Feedbacks affection global warming and climate change [3]

It has become increasingly clear that human activities have irrefutably caused global warming primarily through emitting CO_2, a Greenhouse Gas (GHG). The rise in anthropogenic CO_2, due to human activity has been undeniably linked to the formation of a positive feedback loop, as shown in fig 1.3, beginning with an increase in $CO2$ concentration levels, which then elevates global surface temperatures. As a result, these changes have led to increasing sea levels and, in turn, boosted the frequency of extreme weather events occurring worldwide every year [39].

1.1.2. Renewable Energy: current trends and challenges

The [39] summary says that, a swift and immediate reduction in greenhouse gas emissions must be called for in all sectors this decade. Among all modelled pathways to bring an actionable change, the adaptation of Renewable Energy (RE) technologies has emerged as a key solution. It has to be noted that, the window of opportunity to act and secure a livable future has been rapidly closing every year [41] , and this has pushed governments to fast-track climate action efforts before we cross the tipping point.

The energy sector, including the industrial, GHG emissions during energy production such as industries, transportation, and buildings account for approximately 75.6% [42] of the annual GHG emissions. Governments worldwide have begun showing interest in finding a solution to tackle climate change. They have concluded that global warming cannot be stopped by just making mitigation efforts. An active adaptation plan must also be implemented. The range of CO_2 mitigation technologies available is vast, and each technology's impact on overall mitigation has been identified.

The main pathway in reducing emissions is to transition from a fossil fuel-dependent economy to a renewable energy-dependent economy. Renewable Energy (RE) technology is used as a collective term that is used for producing energy from various renewable sources such as Solar, wind, Nuclear, Hydro, Geothermal, tidal, and biomass. The potential of these various RE technologies has been mapped globally in this figure 1.4.
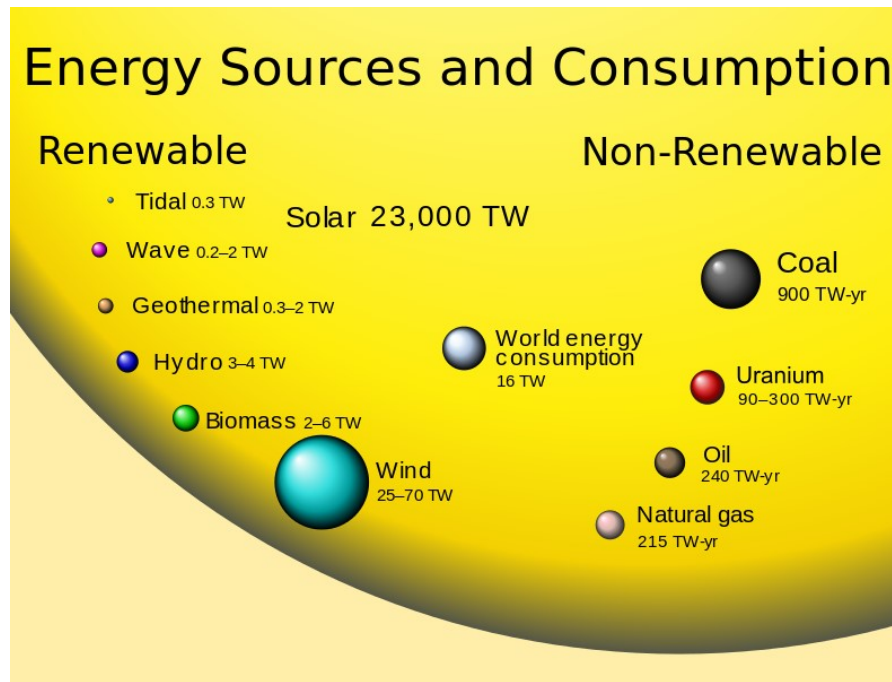
Figure 1.4: Global renewable energy potential in comparison with non-renewable sources [4]

At present, the overall share of RE technologies is around 3382 GW, as shown in 1.5 and it is expected to grow to 7300 GW by 2030 [43]. As RE sources produce useful energy in the form of electricity, countries worldwide must begin with the electrification of different sectors such as transportation, building heating, chemical production, industries, etc.
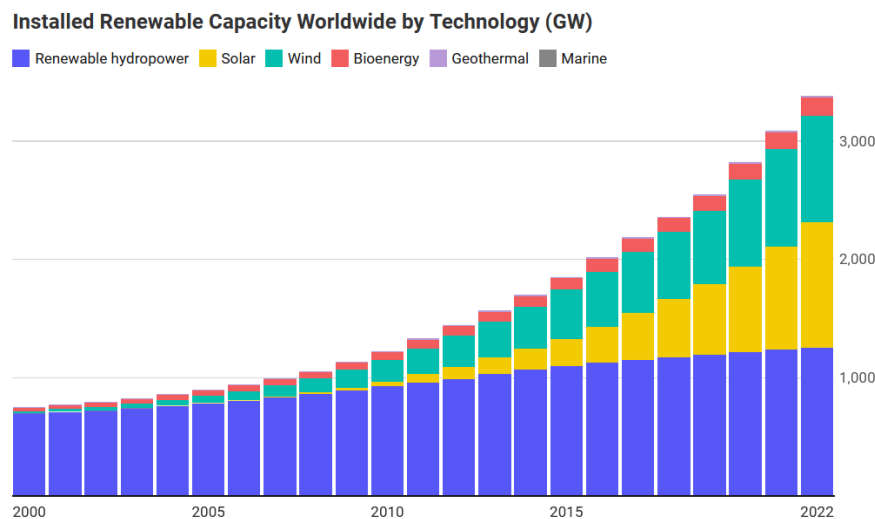
Figure 1.5: Installed Renewable capacity worldwide by technology [5]

1.2. Challenges of Renewable energy

1.2.1. Need for Energy storage technologies

Implementation of the renewable energy-filled future is filled with many challenges and obstacles, One such obstacle during the development and adaptation of RE technologies is the intermittency and the uncertainty of the energy output. The intermittency and uncertainty come from the periodic fluctuations in wind speed and the day-night cycle for solar energy production. This decreases the system's reliability and increases the risk towards adaptation of RE technologies.

Conversely, Inverters that operate outside their ideal conditions cause small imbalances in a decentralized grid due to injecting power into the grid at many places. Power ripples and harmonics [44] caused due to this result in damaging electric devices and producing heat in motors.

Balancing the energy supply and demand at all times plays an important role in managing the reliability of the energy system. Unlike the polluting, fossil fuel-powered base-load technology, RE sources have to be either anchored around a battery or multiple RE sources to increase the overall grid reliability. The reliability of the grid system is being improved at a small scale using techniques such as load shifting, smart grid optimization, and demand side management [45] on the consumer side by incentivizing them to modify their energy consumption patterns.

Smart grids play an important role as they assist in the transformation to a decentralized energy system. They monitor energy production by various RE technologies and manage the transport of electricity to consumers. Their operation focuses on the principle of minimizing the cost and environmental damages while maximizing the reliability of the energy infrastructure.

Battery Energy Storage Systems (BESS) store the surplus during RE production to be used at different timescales as shown in fig 1.6. The overall grid reliability can be increased mainly by setting up different BESS technologies (tab 1.1) at a large scale. The key significance for their growth and importance are [46],

- **Storing Surplus Energy:** Batteries help store the excess energy during low demand and inject power into the grid at high demand to reduce the stress on the grid and increase profits during the arbitrage.
- **Enabling Grid Stability:** They act as a reliable source to maintain smooth operations of the grid and help prevent blackouts.
- **Increasing Energy Independence:** Homes and buildings equipped with a RE source coupled with a battery enable the consumer to be self-reliant and lower their carbon footprint.
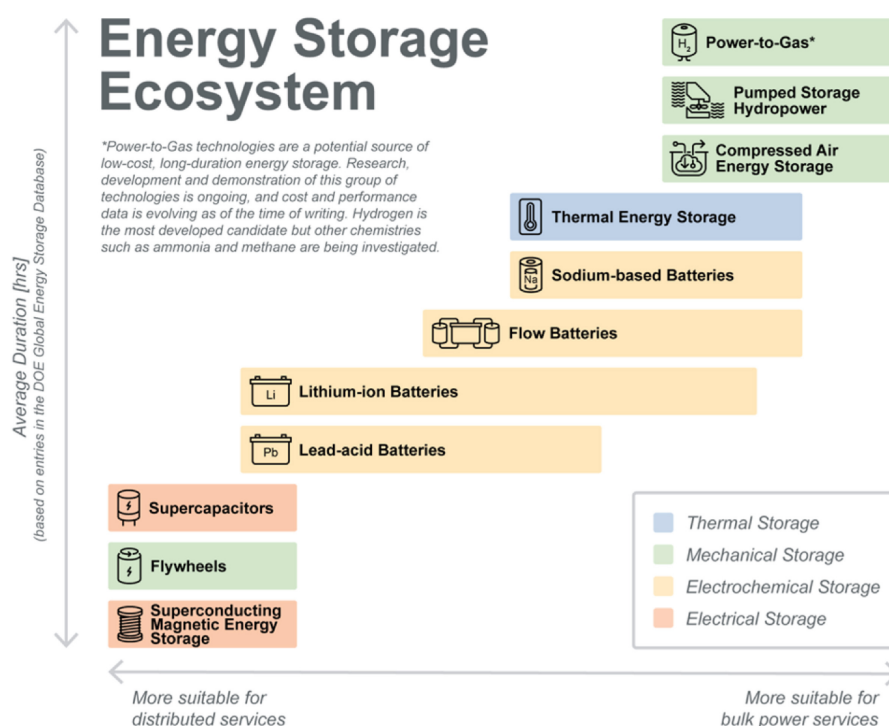
Figure 1.6: Battery Energy Storage Systems (BESS) suitable for timescales [6]

Table 1.1: List of Energy storage technologies and its technical specifications

Technology	Energy density (Wh/L)	Levellized cost of storage ($/kWh)	Discharge time	Lifespan (Years)	Round-trip Efficiency (%)	Response time (S)
Lithium-ion [47]	200-400	0.314	1min ro 8h	1000-10,000 cycles	85-95%	Millisecond
Lead acid [47]	50-80	0.15-0.3	1min to 8h	6 - 40 years	80-90%	Millisecond
Flow battery [47]	10-25	0.2-0.6	5h-10h	>12,000 cycles	60-85%	1 second
PHS [48]	0.5-1.5	0.054	4h to 16h	30 - 60 years	70-80%	Seconds to minutes
CAES [48]	55-60	0.12-0.21	1h to 24h	>10,000 cycles	41-75%	3 - 10 minutes
Flywheel [47]	470-490	0.146-0.189	15 sec to 10 min	200,000 cycles	70-95%	Millisecond to seconds
Molten Salt [48]	75-200	0.127-0.255	1h to 12h	4500 cycles	87%	Milliseconds to seconds
Supercapacitors [48]	300-4000	0.193	0.1 sec to 1 min	20 years	80-95%	Millisecond
Hydrogen [6]	1250	0.207-0.277	1 sec to –	5 - 15 years	34-62%	Second

We conclude that Energy Storage (ES) will be the main component in meeting the future mismatch in RE production and consumption. Although the short-term mismatch can be reduced using smart grids, demand management, and load shifting, energy storage must be implemented on a large scale to increase the reliability of the grid at all timescales.

1.2.2. Barriers in Energy storage

The main barriers to deploying a large-scale energy storage system such as batteries are costs, lack of incentives, loose policy framework, and market disruptions. The large upfront costs for purchasing the technology Capital Expenditure (CAPEX) and operational Expenditure (OPEX) are associated with the maintenance and operation of the system. The lack of incentive options makes BESS harder to implement.

The availability of raw materials and ores needed for energy storage systems has multiple supply chain constraints ranging from geopolitical interests to ethical concerns. Although the cost of lithium-ion batteries has gone down in recent decades, the lithium and cobalt supply chain has been facing issues such as disruptions and increases in project risk due to competition from electric vehicle manufacturers and other geopolitical world problems [49].

The current electricity grid, designed for centralized operation has to be replaced with a stronger and decentralized grid that could handle multiple injection points. Subsidiaries, supporting policies, and a clear regulatory framework from governments are necessary for the seamless integration and deployment of large-scale energy storage systems.

Public perception and acceptance of large-scale energy storage systems also play an important role in many countries worldwide. The safety and environmental impact factors have to be calculated with proper risk assessment and Life Cycle Analysis (LCA) for every project before execution.

1.3. Alternate fuels

1.3.1. Exploring different Alternate fuels

Energy storage must be implemented for both the short and long-term timescales as shown in fig 1.6. Long-term energy storage solutions must be used on top of short-term energy storage solutions. The timescale of handling mismatch with short-term energy storage is between a few seconds to hours, whereas with long-term energy storage, it is between a few days to weeks. Table 1.2 shows the ideal use of different technologies in different timescales.

Table 1.2: Energy storage technology classification for different timescales [6]

Timescale	Technology
Short-term	Lithium-ion batteries, lead-acid batteries, flow batteries, nickel-cadmium batteries, supercapacitors, flywheels, PHS, CAES, gravitational energy storage, metal-air batteries, phase change energy storage, molten salt thermal energy storage.
Long-term	PHS, CAES, ammonia, hydrogen, bio-methanol, sustainable aviation fuels

Long-term energy storage technologies are needed in countries where the surplus in energy has to be stored over a few days to weeks. It is assumed to have full capacity value since it could discharge continuously for many days. In that scenario, conventional short-term energy storage technologies cannot be used as the cost of installing devices such as lithium batteries increases steeply with an increase in size. Alternate fuels such as hydrogen, methanol, and ammonia are possible solutions for long-term energy storage. All the long-term options are listed in table 1.3.

Table 1.3: Comparison of different long-term energy storage technologies

Technology	LCOE ($/kWh)	Efficiency	Advantages & disadvantages
PHS [47]	0.5-1.5	70-80 %	✓Very large capacity and high efficiency – Scarcity of available sites with two large reservoirs
CAES [47]	0.12-0.21	41-75%	✓High scalability – The process of compressing and expanding air is not perfectly efficient.
Ammonia [6]	0.167-0.20	10-50%	✓High energy density combined with the presence of an existing infrastructure. –Direct toxicity and release of harmful NOx gases while combustion
Methanol [6]	0.144-0.148	15-26 %	✓Existing fossil fuel infrastructure can be easily switched to methanol – Corrosivity, Toxicity, and GHG gases produced are its major obstacles.
Hydrogen [6]	0.207-0.277	25-35 %	✓Could be used directly as fuel or as feedstock for various energy-intensive processes – Very low well-to-wheel efficiency and the increasing need for rare earth metals.

1.3.2. Rise of the Hydrogen Economy

Our world has been moving towards a clean and decarbonized society due to impacts brought by global warming as seen in 1.5. Different ideas have emerged for different sectors towards achieving the sustainable future goal, like electric cars and heat pumps for transportation and heating.

The idea of a hydrogen economy emerges from the fascinating role hydrogen contributes towards phasing out fossil fuels in energy-intensive sectors such as steel, cement, aviation, shipping and transport [50]. Here we see a potential role for hydrogen and low-carbon electricity working towards decarbonizing major polluting sectors.

The hydrogen economy comprises the life cycle of hydrogen (from production to consumption) and the financial part of hydrogen. Implementation of the hydrogen economy would need a new or redeveloped gas infrastructure. Hydrogen has the potential to be directly used as fuel or as feedstock for other industrial processes.

1.4. Hydrogen as a potential solution

1.4.1. Hydrogen Life-Cycle: Production to Utilization

The life cycle of hydrogen starts with the energy used for producing hydrogen. The energy is used to produce hydrogen at different pressures and purity. The produced hydrogen is purified and stored as

liquid hydrogen (LH2) or at high pressure. The stored hydrogen is transported across different regions on pipelines, roads and ships. Some of it is also converted to alternate fuels such as ammonia, to be used later. Once the hydrogen reaches the end user, it is used as a fuel for transportation, feedstock for energy-intensive industries, and energy production.

Hydrogen Production

At present, the energy required for hydrogen production is supplied as electricity or from other sources such as natural gas, oil, coal, biomass and heat. Nearly 95% of the hydrogen produced is from fossil fuels and is set to change in the future [51]. Energy combined with water is used to produce hydrogen. Although hydrogen can be produced from various methods, hydrogen is mainly produced using these five production pathways as shown in Table 1.4. The energy consumption per Kg for different production pathways is given for an easier comparison.

Table 1.4: Hydrogen production and energy consumption for different pathways [33], [34].

#	Production pathways	Energy Required (KWh/Kg H2)	Energy Source
1	Steam reforming	19.67	Water, Natural gas, Oil
2	Coal gasification	47.06-80	Water, Coal
3	Biomass reforming	30.97	Water, Biomass
4	Electrolysis	55.8	Water, Electricity
5	Electrolysis	55.87	Sea Water, Electricity

Hydrogen produced from various sources can be briefly classified and associated with colours on the Hydrogen colour spectrum. However, instead of only focusing on the colours of hydrogen without indicating their respective carbon intensities, adding this information as shown in Fig 1.7 should facilitate a better understanding and comparison.

The Hydrogen Colour Spectrum

COLOUR	DESCRIPTION: FEEDSTOCK	Kg CO2/ Kg H2
	Grey: Natural gas reforming without CCUS	10.9
	Black: Brown coal (lignite) as feedback	51.9
	Blue: Natural gas reforming with CCUS	2.6
	Green: Electrolysis powered through renewable electricity	0.6
	Pink: Electrolysis powered through nuclear energy	0.4
	Turquoise: Methane pyrolysis	4.4
	Yellow: Electrolysis powered through electricity from solar	0.6
	Orange: Electrolysis powered through electricity from wind	0.4
	White: Obtained from natural processes	0

Figure 1.7: The Hydrogen colour spectrum with carbon intensity values taken from [7].

Hydrogen Purification

Hydrogen purification plays a crucial role in hydrogen production and consumption in large-scale applications such as fuel cell vehicles. Low-cost and highly efficient purification technologies are needed for the development of the hydrogen economy. Hydrogen purification methods can be broadly classified as physical and chemical methods [52].

Physical purification includes adsorption methods, membrane separation methods and low-temperature methods. Metal hydride separation method and catalysis method fall into the chemical purification category. Among these methods, the four main purification methods are briefly mentioned here.

Pressure Swing Adsorption (PSA) method

The PSA method is based on physically binding the gas molecules to the adsorbents. The separation of gases is related to the difference in binding forces with the adsorbent material. The four basic processes are adsorption, depressurization, regeneration and repressurization. Typically, PSA operates at a constant temperature and uses the effect of alternating pressure and partial pressure to perform its adsorption and regeneration processes.

Some examples of adsorbent materials are zeolite sieves, activated carbon, alumina and silica gel. To provide a continuous hydrogen supply and a high recovery rate 4 or more adsorber vessels are used. The purity of PSA varies from 99.2% to 99.9991% under different operating conditions [52].

Membrane separation methods

This is a simple and efficient gas separation technology that uses different membranes to purify gases. Differences in pressure, concentration and potential drive the separation process by allowing hydrogen to pass through the selective membranes.

Metal membranes made of palladium and their alloys show excellent hydrogen permeability, but they face problems such as expensive manufacturing costs and embrittlement. Polymer membranes, on the other hand, show a high selectivity in exchange for low permeability. Emerging membranes like mixed matrix membranes and metal-organic framework membranes offer a higher selectivity while retaining permeability.

Cryogenic distillation

Cryogenic distillation operates by using the relative volatility of different component in gases. The low-temperature distillation process has a purity rate greater than 99.999%. The main drawbacks of cryogenic distillation are the need for a clean gas to prevent blockage, its high costs and energy consumption due to the operation of gas compressors and coolers.

Metal hydride separation method

The purification method operates under the principle of absorbing and desorbing hydrogen in metal alloys. The metal alloys catalyse the hydrogen molecules into H atoms. These H atoms are absorbed into the bulk with impurities in the form of metal hydrides by increasing the pressure and decreasing the temperature.

The impurities and other gases are released when the pressure is decreased and the temperature is increased. Finally, when additional heat is supplied pure hydrogen is released. Hydrogen obtained at a purity greater than 99.9999% has attracted a lot of attention to this method [53].

Hydrogen Storage

Currently, most hydrogen produced is consumed on-site. This is set to change as the world moves forward with the concept of the hydrogen economy, where hydrogen helps decarbonize different sectors. The key factor after the production of hydrogen is storage before transportation. Hydrogen is stored at different pressures and temperatures using the process stated below. Hydrogen could be stored as a gas, liquid or in other materials. The main classifications of hydrogen are physical storage, adsorption storage and chemical storage.

Physical storage

1. **Compressed hydrogen storage:** Hydrogen is stored under pressures ranging from 200 bars to 1000 bars, with a volumetric energy density of 25-30 Kg/m^3. It is a mature technology with fast charging and discharging rates, but a major drawback would be the heat management and safety issues [54].

2. **Liquid hydrogen storage:** Hydrogen is liquefied using the Joule Thompson (JT) expansion and stored in an insulated vessel at -253 $^\circ$ C, with a volumetric density of 50 Kg/m^3. It has a very high volume density, but it is energy-intensive and costly. A major drawback is low stability due to the conversion from ortho to para which leads to boil-offs [55].

3. **Cryo-compressed hydrogen storage:** Increasing the pressure of liquid hydrogen prevents boil-off. The volumetric density of hydrogen increases, but the energy needed becomes even more intensive with a need for expensive tanks.

Chemical storage

1. **Ammonia:** Hydrogen is reacted with nitrogen in the haber-bosch process to produce ammonia. It has a volumetric energy density of 107 Kg/m^3. Combustion of ammonia in retrofitted gas turbines is a great option.

2. **Liquid Organic Hydrogen Carriers (LOHC):** Hydrogen is stored in the form of chemical bonds in organic molecules, with a volumetric density of 60 Kg/m^3. This has a lot of potential to be used in the existing infrastructure.

3. **Metal hydrides:** Hydrogen is stored in metals and metal alloys when they are absorbed into the bulk and stored between the interstitial sites. They have one of the highest volumetric densities 50-175 Kg/m^3. The system has lower investment needs and does not need high pressure, but the drawback is the need for high operating temperatures.

4. **Methanol:** Hydrogen is stored in the form of methanol, which falls into the C1 molecule category. A major advantage of methanol could be made from CO2 and hydrogen with a volumetric density of 100 Kg/m^3, but the main drawback is the inevitable of CO2 back into the atmosphere. This form of storage could be adapted in the early stages of the hydrogen economy as we have an existing infrastructure with internal combustion engine vehicles.

Adsorption storage

1. **Porous organic polymers (POPs):** Hydrogen storage is done when the gas is adsorbed on the surface area of the polymer. These POPs have a very high surface area and low density. Some advantages are the high surface area and low density shown by POPs due to the absence of heavy metals.

2. **Carbon based materials:** Hydrogen is stored in carbon based materials such as graphene, carbon nanotubes, nanofibers and activated carbon. Hydrogen gas is adsorbed on carbon materials with a high surface area of 2900 - 5100 M^2/g.

Hydrogen Transport

Currently, the infrastructure for hydrogen does not exist because most of the hydrogen produced is on the demand site. Hydrogen pipelines, refuelling stations, compressed hydrogen tube trailers, and hydrogen transport ships are some key components in adapting the hydrogen economy.
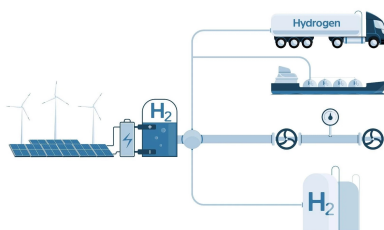
Figure 1.8: Hydrogen transportation infrastructure [8]

Hydrogen pipelines

Hydrogen pipelines are crucial as they are the cheapest mode of moving hydrogen from the hydrogen production point to the point of demand. The technology is proven, but hydrogen pipeline has two main disadvantages, hydrogen embrittlement and high costs. Hydrogen embrittlement happens when hydrogen enters the structure from welding joints and surface defects and alters the property of the material and decreasing fracture resistance.

Hydrogen trailers

At the initial stages, to meet the demand at hydrogen refuelling stations a collection of hydrogen trailers can decrease the initial cost of refuelling stations [56]. Hydrogen transportation trailers can be classified into compressed hydrogen trailers and liquid hydrogen trailers. Each trailer can transport 300-600 kg of hydrogen at 450 bars.

Hydrogen highways

Along with hydrogen pipelines, a network of hydrogen refuelling stations must be deployed to meet the demand for fuel cell vehicles. Although the initial stages of demand could be met with hydrogen trailers, a detailed hydrogen pipeline connecting all the refuelling stations must be installed along highways.

Hydrogen ships

Globally, countries are emerging as hydrogen producers and as hydrogen consumers with vast distances between them spanning oceans and continents. The only solution to this problem would be the development of global hydrogen transportation fleets. Hydrogen is cooled to - 253 $^\circ$ C before it is loaded onto the vessel. The initial concentration of ortho and para hydrogen makes a big impact on long term stability of hydrogen shown in Fig 1.9. Para hydrogen is the thermodynamically stable form of hydrogen and conversion of ortho hydrogen to para hydrogen is an exothermic process, this leads to a large boil-off [9].
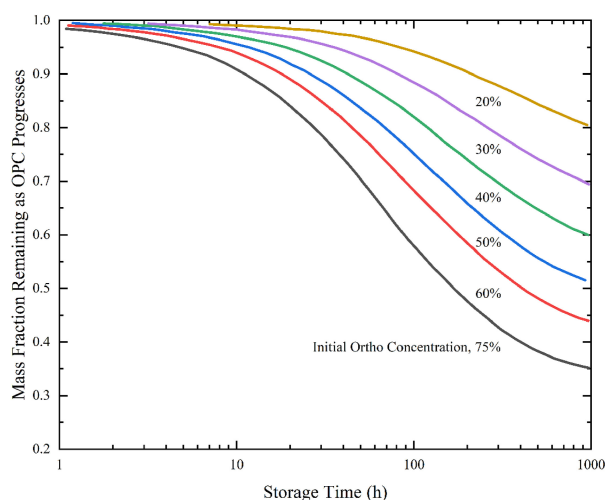
Figure 1.9: Mass fraction of liquid hydrogen remaining in the vessel [9]

Hydrogen Utilization
At present, hydrogen is consumed mainly by three sectors: Crude oil refining, ammonia production, and methanol production as shown in Fig 1.11. This trend is set to change in the coming future. Hydrogen can be used to decarbonize the transportation sector, electricity and heating sector, industrial sector and agricultural sector.

Transportation Sector
The transportation sector has five main polluters cars, trucks, flights, trains, and ships. At present, with the advent of electrification, most trains are electric. Cars can be equipped with fuel cells or hydrogen combustion engines. Ships can be converted to run on hydrogen or ammonia made from green hydrogen. Decarbonizing the transportation sector could lead to a 16.2% reduction in global GHG emissions [57].

Electricity and heating Sector
Energy used in the form of electricity and heat in residential buildings and commercial buildings can be decarbonized using green electricity and hydrogen. Heat pumps are being developed to use hydrogen to meet the heat demand for buildings. Hydrogen can be used to produce electricity using fuel cells and gas turbines.

Industrial Sector
The industrial sector, which accounts for 29.4% of the total GHG emissions, has some sectors that can be decarbonized using hydrogen. Hydrogen can replace natural gas and be burnt in cement kilns to produce heat. Hydrogen can replace coal in the blast furnace route and help in refining steel ores which would reduce nearly 7% of global GHG emissions [57]. Hydrogen can be used to supply continuous energy for industrial processes in an intermittent future filled with renewables.

Agricultural Sector
At present, we produce 235 million tons of ammonia every year which accounts for nearly 1.4% of the total energy consumption. Adding green hydrogen to the Haber-Bosch process would reduce approximately 1% of global GHG emissions [57].

1.5. Advancing towards a Hydrogen centric future
1.5.1. Current Hydrogen Status
Today, hydrogen is produced commercially as feedstock in the chemical industries, steel production and heat and power generation. At present over 95% of the world's hydrogen comes from fossil sources as shown in Fig 1.10. The production of hydrogen stands at around 120 Mt.H2/yr, with 75 Mt.H2/yr as pure hydrogen and the rest as a part of mixed gases [58].

Global Hydrogen production pathways, 2023
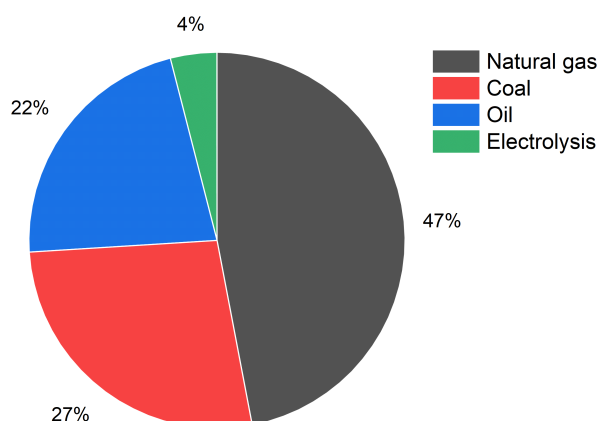
Figure 1.10: Current hydrogen production pathways, 2022, [10]

The present standards for hydrogen are being set by different hydrogen production and consumption industries with no common regulations. This also extends to the lack of proper certification schemes and their governance. The rise in these uncertainties due to a lack of standards and certification schemes could undermine the hydrogen market.

Hydrogen Consumption, 2023
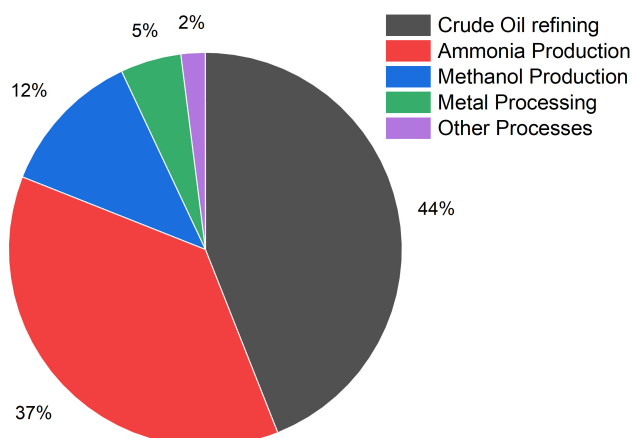
Figure 1.11: Current hydrogen consumption pathways, 2022, [10]

The current demand for hydrogen emerges from four main processes as shown in fig 1.11. The biggest share of hydrogen demand, taking up to 44% of the total hydrogen produced, comes from crude oil refining followed by ammonia production which takes up 37% of hydrogen produced to mainly manufacture fertilisers [51].

1.5.2. Future Hydrogen Status

As mentioned in fig 1.10 and Figure 1.11, the current hydrogen production relies on polluting fossil fuel sources, which has been predicted to continue until 2030. Between 2030 and 2040, a small yet gradual transition is expected from grey and black hydrogen to cleaner pathways for hydrogen production such as blue and green hydrogen [59]. After 2040, hydrogen production is predicted to be completely from clean pathways, and thereby only in the form of green hydrogen.

Established certification standards are assumed to be achieved for different grades of hydrogen. Hydrogen prices are expected to drop due to the economies of scale and market growth, and also due to the subsidiaries and programs from the government. The European Hydrogen Bank conducted the first hydrogen auction in 2024 to support renewable hydrogen producers [60].

As shown in section 1.4 green hydrogen would be used to meet the current hydrogen demand and in decarbonizing sectors, like transportation, heating and industries. The growth of renewable hydrogen opens up opportunities for international hydrogen trade. Implementation of a standardised hydrogen certification scheme to classify various forms of hydrogen is necessary for a smoother implementation of the hydrogen economy and cross-border trades.

Finally, the infrastructure required for the hydrogen economy has to be developed. Along with the physical infrastructure, the regulatory infrastructure must also be developed for the successful deployment of hydrogen on a large scale.

2

Electrolysis based hydrogen production

In this chapter, Section 2.1 gives an introduction to electrolysis and its history. Section 2.2 explains the traditional alkaline water electrolysis (AWE), Section 2.3 explains the commercial proton exchange membrane water electrolysis (PEMWE). Section 2.4 which gives an introduction to anion exchange membrane water electrolysis (AEMWE), followed by an introduction to the AEMWE components and challenges in Section 2.5. Section 2.6 gives an introduction to anion exchange membrane and PCAP. Finally, The research formulation with objectives and research questions are given in 2.7.

2.1. Introduction to Electrolysis

The process of producing hydrogen by applying a potential between two electrodes in water is called electrolysis. Water molecule is converted to molecular hydrogen and oxygen at a high purity during electrolysis. Hydrogen is produced at the cathode where the reduction of water occurs, whereas oxygen is produced at the anode where oxidation occurs.

The history of water electrolysis dates back to 1789 when an electrostatic generator was used to generate "combustible air". later the demand for hydrogen increased in the 1920s due to the introduction of the Haber-Bosch process to produce ammonia, and thereby fertilisers, This promoted a large growth in alkaline water electrolysis technology. In the later stages of the 20th century, steam methane reforming (SMR), a cheap hydrogen production technology replaced the water electrolysis technology [61].

Water electrolysis can be classified based on their operating temperatures, charge carriers, and the type of electrolyte used. The classification of electrolysis based on temperatures is given below.

- **Low-temperature (80-100° C) electrolysis**: Proton exchange membrane (PEM), Alkaline water and anion exchange membrane (AEM) water electrolysis technology [62].
- **High-temperature (600-1000° C) electrolysis**: Solid oxide (SO), proton conductive ceramic (PCC), and co-electrolysis with solid oxides (CoSO) water electrolysis technology [61].
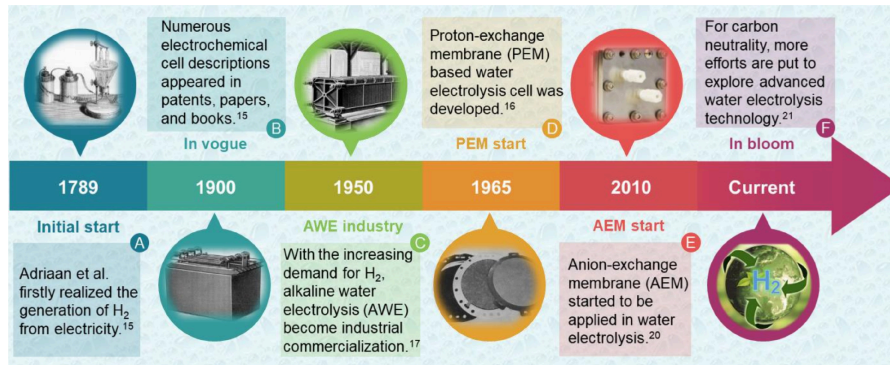
Figure 2.1: Timeline for the development of low-temperature water electrolysis technology [11].

Table 2.1: Comparison of the low-temperature water electrolysis technologies [16]

	Alkaline	**PEM**	**AEM**
Electrolyte	5-6 M KOH	perfluorosulfonic acid (PFSA)	1M KOH
Operating temperature °C	65-100	70-90	50-80
Charge carrier	OH^-	H^+	OH^-
Separator	Asbestos, Zirfon	Nafion, PFSA	QPPO, PCAP
Current density (A/cm^2)	0.2-0.5	0.8-2.5	0.2-7.8
OER catalyst	Ni/Fe or Ni/Co based	Ir based	Ni based
HER catalyst	Ni based	Platinum based	Ni based
Current collector	Ni	Ti	Stainless steel, Ni
Hydrogen purity %	99.3-99.9	99.9999	99.99
Market potenital	Ready	Ready for small scale	R&D

2.2. Traditional approach: Alkaline Water Electrolysis (AWE)

Alkaline water electrolysis is the most mature and reliable technology for hydrogen production. It uses Nickel and cobalt oxides as the anode and cathode respectively with a 30-40% potassium hydroxide (KOH) aqueous electrolyte. A separating porous diaphragm is installed between the anode and the cathode chambers for conducting the hydroxyl ions. This separator made of asbestos and polymers prevents gas crossover and ensures high operation efficiency. A schematic diagram of an alkaline water electrolyser cell is shown in fig 2.2 and the half-cell reactions are given below.
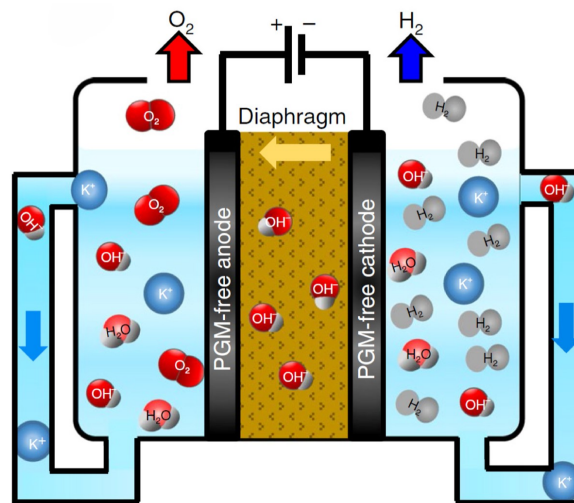
Figure 2.2: Schematics of a Alkaline water electrolysis cell [12]

Anode (Oxidation): $2OH^- \rightarrow H_2O + \frac{1}{2}O_2 + 2e^-$
Cathode (Reduction): $H_2O + 2e^- \rightarrow H_2 + 2OH^-$

Alkaline electrolysis has benefits such as its ability to use inexpensive non-platinum group metals (PGM). They have low over potential and are stable in alkaline media. The overall resistance of AWE could be split into three categories [63].

1. Electrochemical reaction resistances - R_{Anode} and $R_{Cathode}$
2. Transport related resistances - $R_{O_2 Bubble}$, $R_{H_2 Bubble}$, R_{Ions}, and $R_{Membrane}$
3. Electrolca resistance - $R_{Electric}$

High impedance across electrolytes and porous membranes combined with these resistances causes large ohmic losses via heat generation. This results in lower operating current densities, and a drop in energy efficiency. K_2CO_3 is formed due to the reaction between the electrolyte (KOH) and atmospheric CO_2, The K_2CO_3 produced reduces the performance of AWE by decreasing the hydroxyl ion concentration, reducing the electrolyte ion conductivity, and blocking the ion-conducting pores and channels [16].
When operating the AWE at low current densities and high-pressure regimes, the diffusion of OH$^-$ ions through the porous bipolar membrane (Zirfon) leads to the movement of electrolytes with dissolved hydrogen. The crossover of hydrogen from the cathode compartment to the anode compartment (greater than 4% hydrogen in oxygen) leads to the formation of an explosive gas mixture [63].

2.3. Proton Exchange Membrane Water Electrolysis (PEMFC)

PEM water electrolyser is a promising technology for the production for high-purity hydrogen, operating efficiency and low temperatures between 70-990 °C [62]. This setup consists of an Iridium Oxide anode and a Pt black cathode catalyst, ensuring efficient electrolysis. An acidic solid polymer electrolyte, Nafion, is used to conduct the hydrogen ions from the anode to the cathode while preventing gas crossover [64]. A PEM electrolyzer cell schematic diagram as shown in fig 2.3 and the half-cell reactions are given below.
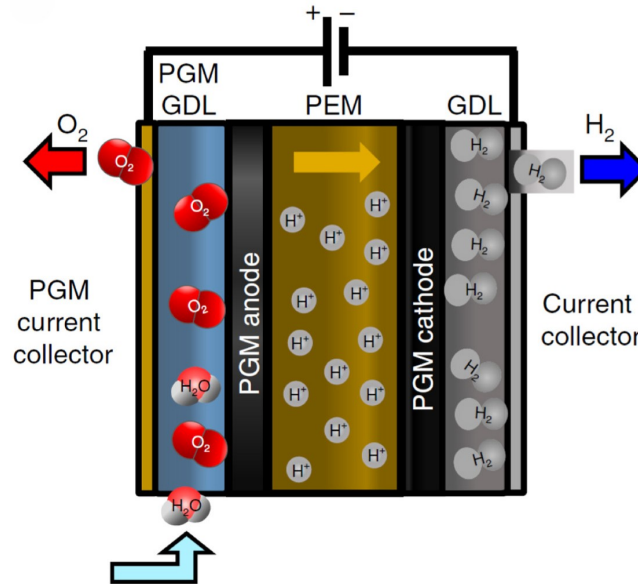
Figure 2.3: Schematics of a PEM electrolysis cell [12]

Anode (Oxidation): $H_2O \rightarrow \frac{1}{2}O_2 + 2H^+ + 2e^-$
Cathode (Reduction): $2H^+ + 2e^- \rightarrow H_2$

The PEM operates at a high current density of 2000 mA/cm^2 with a voltage of 2.1 V [12]. PEM electrolysers have a faster response time and high efficiency when compared to conventional alkaline electrolysers. This is due to the fast kinetics of hydrogen and oxygen production at the electrodes, facilitated by the acidic nature of the electrolyte and the abundance of protons available on the metallic surfaces [16]. TH kinetics of hydrogen evolution reaction (HER) is faster due to the availability of higher concentrations of H_3O^+ in an acidic environment. Lower hydrogen binding energy (HBE) of Pt combined with Hydrogen adsorption on the catalyst surface is crucial for a faster HER [65].

2.4. Anion Exchange Membrane Water Electrolysis (AEMWE)

AEM water electrolysis is the most recently developed water electrolysis technology 2.1. This technology combines the advantages of AWE and PEM electrolysis. The zero-gap AEMWE technology uses non-PGM catalyst materials like nickel and cobalt oxides, and a low-concentration alkaline solution can be used as an electrolyte which makes the system less corrosive. The AEMWE process can produce gases with high purity and operate at high pressure with low ohmic losses.
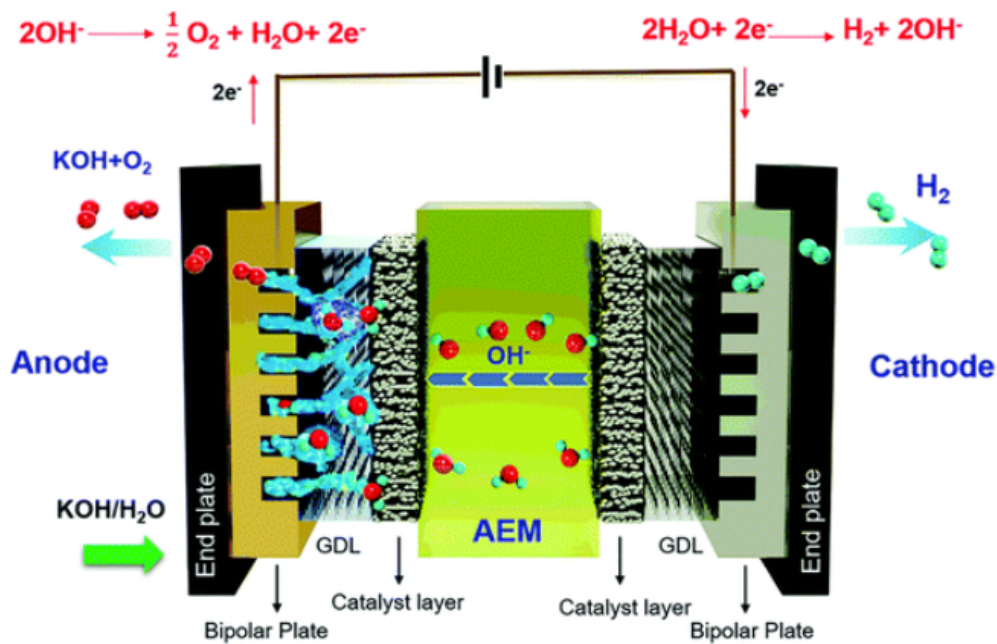
Figure 2.4: Schematics of an AEM water electrolysis cell [13]

The anode and cathode catalysts are separated by an anion exchange membrane (AEM), which conducts hydroxyl groups from the cathode to the anode. The AEM also acts as a separator that prevents the mixing and crossover of hydrogen and oxygen gases. The membranes used in AEMWE are less polluting when compared to Nafion membranes used in PEMWE, as they do not have any 'forever' chemicals. The polymer AEM membranes are also cheaper than membranes used in PEMWE and AWE. AEM uses gas diffusion layers and bipolar plates made of stainless steel and Nickel, whereas PEM uses expensive metals such as Titanium. Despite these advantages, AEMs have low durability as the polymer membrane is susceptible to degradation [16].

2.4.1. Chemistry of AEMWE

The operating principle of AEMWE is shown in fig 2.4. The system electrochemically splits water to generate hydrogen and oxygen when a voltage between 1.8-2.5 V is applied [66]. When an external source, under an applied potential, injects electrons into the surface of the cathode electrocatalyst, water molecules near the cathode undergo, a water-splitting, hydrogen evolution reaction (HER). This is a reduction reaction where the hydrogen ion (H^+) gains an electron from the cathode electrocatalyst surface to form hydrogen gas (H_2).

$$HER : 4H_2O + 4e^- \rightarrow 2H_2 + 4OH^-$$
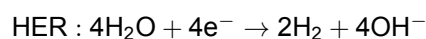
The AEM facilitates the movement of the produced hydroxide ions (OH^-) from the cathode side to the anode side. On the anode side, oxygen gas (O_2) is produced during the oxygen evolution reaction (OER). The OH^- anions reacts on the anode electrocatalyst, forming OH^* and OOH^* intermediates, eventually producing O_2 gas and 4 electrons. The electrons produced are absorbed through the current collector and eventually sent to the cathode to complete the circuit [63].

$$OER : 4OH^- \rightarrow O_2 + 2H_2O + +4e^-$$
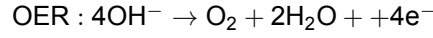
The two half-cell reactions in the electrodes and the overall cell reaction in the AEMWE cell are given below [66],

$$\textbf{Anode} : \mathbf{4OH^- \rightarrow O_2 + 2H_2O + +4e^-; E_0 = 0.401V}$$
$$\textbf{Cathode} : \mathbf{4H_2O + 4e^- \rightarrow 2H_2 + 4OH^-; E_0 = 0.828V}$$
$$\textbf{Overall} : \mathbf{4H_2O \rightarrow 2H_2 + O_2; E_0 = 1.23V}$$
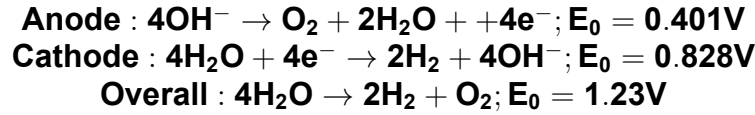
2.4.2. Thermodynamics of AEMWE

The water-splitting reaction is not thermodynamically favourable, as the required Gibbs free energy is positive, +273 kJ/mol, at standard conditions. This shows that external energy is needed to move forward with the non-spontaneous reaction.

The Gibbs free energy is given by the equation $\Delta G = \Delta H - T\Delta S$, where the H, T and S stand for enthalpy, temperature and entropy respectively. In addition to the +237 kJ/mol of electrical energy supplied the system needs +48.6 kJ/mol of heat to operate at standard conditions [63].

$$\Delta G = -nFE_{cell}$$

The required energy (ΔG) is supplied to the system by applying an electric potential. In this equation F, n, and E_{cell} represent the Faradaic constant, number of moles, and electric cell potential respectively. When only the electrical energy of +273 kJ/mol is supplied by an external source, the potential we obtain is the equilibrium cell voltage of +1.23 V. But, when the total energy of +321.6 kJ/mol is supplied using electrical energy then a voltage of 1.48 V called thermo-neutral voltage is applied [16].

2.4.3. AEMWE kinetics

HER and OER are the two main reactions happening during the AEMWE operation. The rate-limiting step in HER is the breaking of the H-OH bond to generate H*. Compared to an acidic medium, HER is more sluggish in an alkaline medium due to water dissociation.
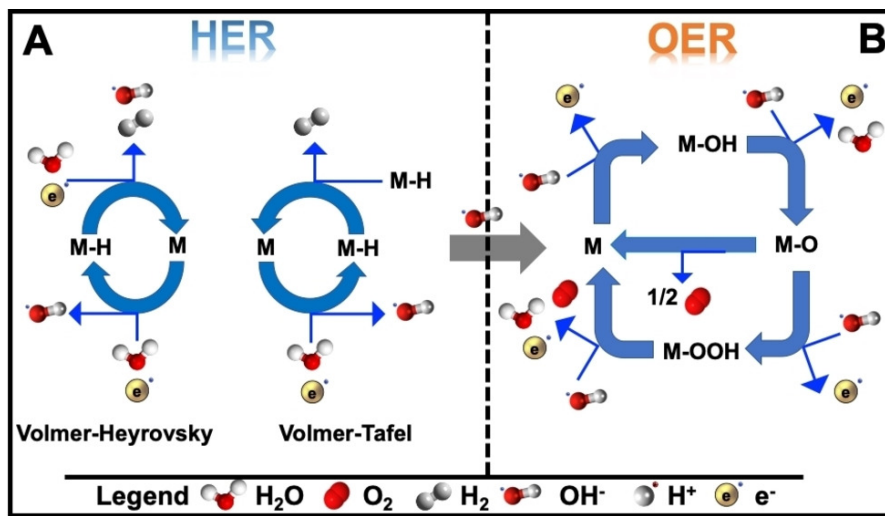
Figure 2.5: Schematics of HER and OER reactions in AEMWE process [14]

Hydrogen evolution (HER) occurs in two steps as shown in fig 2.5A. First, the Volmer reaction occurs where water molecules are dissociated into OH^- ions and $M-H_{ads}$. The second step either occurs electrochemically through the Heyrovsky step or chemically through the Tafel step [66].

$$\text{Volmer step: } H_2O + M + e^- \rightarrow M - H_{ads} + OH^-$$
$$\text{Heyrovsky step: } M - H_{ads} + H_2O + e^- \rightarrow H_2 + OH^-$$
$$\text{Tafel step: } 2M - H_{ads} \rightarrow H_2 + 2M$$
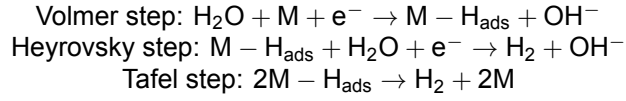
Oxygen evolution (OER) occurs through a 4-step process as shown in Fig 2.5B [14]. First, the OH^- ions that migrate from the cathode side adsorb on the catalyst surface to form an M-OH intermediate. Second, M-OH is converted to M-O intermediate when it reacts with an OH^- ion. The Third step has two pathways either forming O_2 gas or by forming an M-OOH intermediate. Finally, MOOH reacts with another OH^- ion to form O_2 [66].

$$\text{First step: } M + OH^- \rightarrow M - OH_{ads} + e^-$$
$$\text{Second step: } M - OH_{ads} + OH^- \rightarrow M - O + e^- + H_2O$$
$$\text{Third step: (1) } M - O + OH^- \rightarrow MOOH^* + e^-$$
$$\text{Third step: (2) } 2M - O \rightarrow O_2 + 2M$$
$$\text{Fourth step: } MOOH^* + OH^- \rightarrow O_2 + M + e^- H_2O$$
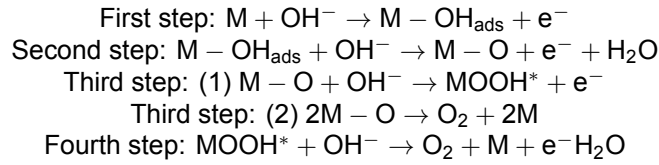
Further developments should be focused on improving the adsorption properties and doping the catalyst to introduce new sites for HER catalysts. Whereas, for OER catalysts, the lattice oxygen mechanism and the surface reconstruction of the catalyst must be studied further [66].

2.4.4. Resistances and overpotential

The operating cell voltage (E_{Cell}) of AEMWE is obtained by adding the reversible cell potential with different overpotentials. The potential distribution of the polarization curves is given in fig 2.6.
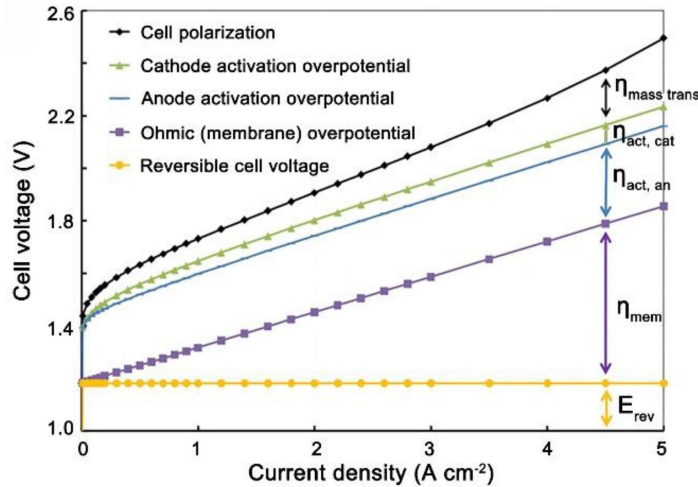
Figure 2.6: Overpotential distribution in polarization curves [11]

$$E_{Cell} = E_{reversible} + \eta_{activation} + \eta_{ohmic} + \eta_{mass}$$

The ohmic overpotential (η_{ohmic}) represents the electrical and ionic resistance of the membrane, is found using the high-frequency resistance (HFR) values obtained from electrochemical impedance spectroscopy [11]. The activation overpotential ($\eta_{activation}$) is based on the catalyst activity and the MEA behaviour of anode and cathode electrocatalyst is derived from the Tafel plot. Finally, the mass transfer overpotential (η_{mass}) that occurs due to the reduction in the supply of electrolyte to the electrocatalyst surface, the formation of bubbles, could be estimated using the Nernst equation [15].

2.4.5. Operation of AEMWE

In addition to the electrolyte and catalyst layer affecting the AEMWE performance, some parameters affecting the AEMWE performance such as operating temperature, pressure, current density, and voltage are given below.

Current density

As the current density of the AEMWE process increases, we get an initial increase in yield, but once the current density crosses a certain threshold, the fast rate of bubble production would reduce the electrolyte-catalyst contact and hence increase the overpotential of the cell as shown in fig 2.6. The Typical operating current density of the cell is maintained between 0.1-0.5 A/cm^{-2} [12].

Operating temperature

The AEMWE normally operates between the range of 50-80 °C. A higher activation energy barrier in AEM, when compared to PEM, shows that higher operation temperatures improve ion transport [15]. Fig 2.7(A) shows that the AEMWE cell displays a higher current density at elevated temperatures [12].
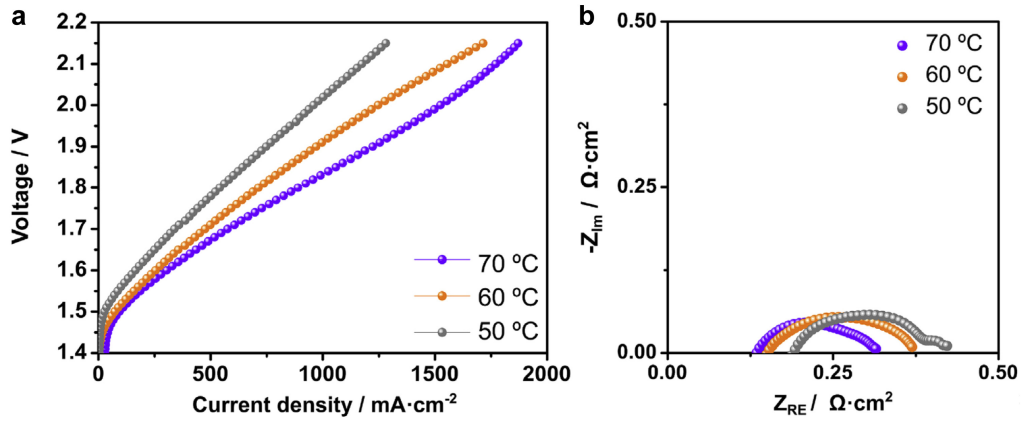
Figure 2.7: Polarization curves and Nyquist plots of AEMWE at different operating temperatures [12]

An increase in temperature could increase catalyst activity, reduce ohmic resistance by accelerating electrons, and reduce ionic resistance by improving mass transport during the AEMWE operation as shown in fig 2.7. Therefore, an increase in temperature from 50 to 70 °C improves the AEMWE process by decreasing the overpotential of the electrolysis process [12].

Operating pressure

A high operating pressure increases the E$_{cell}$ according to the Nernst equation. Although there is an increase in energy consumption, as shown in fig 2.8, AEMWE operation at pressures up to 15-40 bars produces high-pressure H$_2$ gas [15].
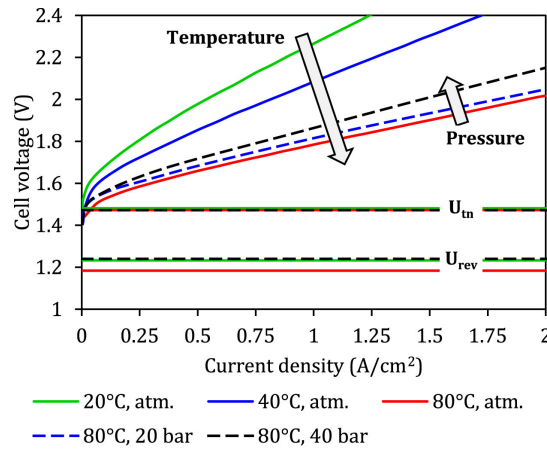
Figure 2.8: Polarization curve based on different operating temperatures and pressures [15]

This reduces the energy needed for compression, and studies show that operating at high pressures has the additional advantage of lower water content in the produced hydrogen. The crossover rate of hydrogen gas from the cathode to the anode chamber is significantly lower [12].

2.5. AEMWE components

The components of the AEMWE setup are briefly explained below. The anode catalyst layer, AEM, and the cathode catalyst layer combine to form a membrane electrode assembly (MEA).
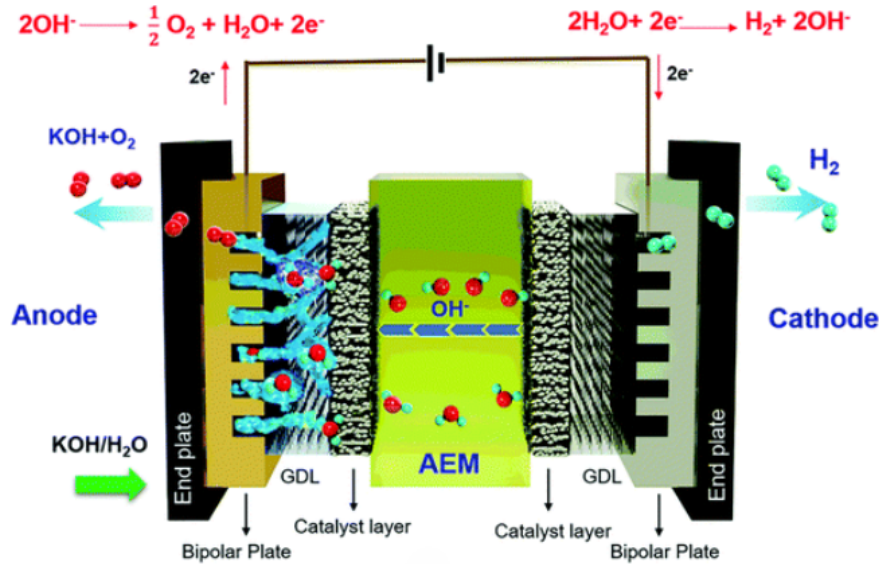
Figure 2.9: Components and schematics of AEMWE [13]
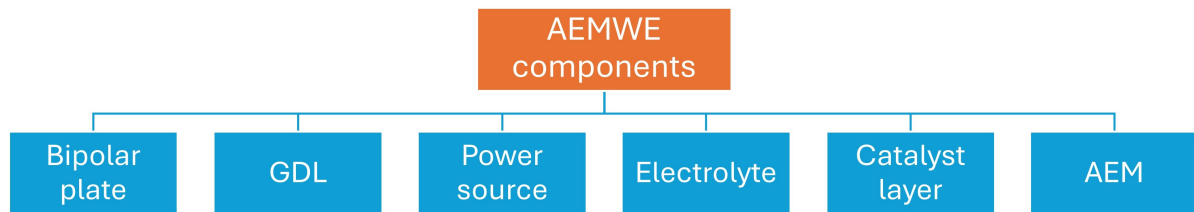
2.5.1. Bipolar plates

The bipolar plates are made of Ni or stainless steel. They help in circulating the electrolyte across the cell, removing the produced bubbles, providing mechanical support, conducting heat, and finally conducting electricity [14].

2.5.2. Power source

The total energy required for the AEMWE process is supplied by applying a constant DC through an external source. Typically, a lab-scaled testing system (LSTS) uses a potentiostat coupled with a current booster for all the electrochemical processes [11].

2.5.3. Gas Diffusion Layer

The gas diffusion layer (GDL), also referred to as, the porous transport layer (PTL), assists the flow of electrolytes to the reaction sites at the electrocatalyst surface. Typically, GDLs are placed on both sides of an MEA when assembling the electrolysis cell. They also act as a current collector sending the electrons to the bipolar plate. At high current densities, the bubbles formed at the anode and cathode sites block the contact between electrolyte and catalyst and hence increase the mass transfer resistance [67]. This can be avoided using a fiber, foam or woven metal GDL with a large surface area to increase the contact between catalyst layers and the AEM [68].

2.5.4. Catalyst layer

The membrane electrode assembly (MEA) consists of the ionomer, AEM, anode catalyst and cathode catalyst. The catalyst layers are made into an MEA using the catalyst-coated substrate (CCS) or the catalyst-coated membrane (CCM) method. In the CCM approach, the catalyst mixed with the ionomer is spray-coated on the membrane. Whereas, In the CCS approach, the porous transport layers are deposited with the catalyst ink and then sintered [12].

In this thesis, MEA is assembled using the CCS method for AEMWE testing. The ionomers, anode catalyst and cathode catalyst used in AEMWE processes are briefly explained below.

Ionomers: They are the binders that typically assist in creating pathways between the AEM and the reaction sites in the catalyst layer. Poly sulfone is widely used due to its high thermal and chemical stability in alkaline processes [16].

Anode catalyst Layer: The oxygen evolution reaction (OER) happens at the anode. This 4-step process has poor kinetics and a high overpotential compared to HER. Anode catalysts are made using PGM-free transition metals, Among the many such catalyst options, NiFe alloy shows the highest activity in alkaline medium [64].

Cathode catalyst Layer: Hydrogen evolution reaction (HER) occurs at the cathode layer. This is a 3-step process. Volmer step splits water into M-H_{ads} intermediate and hydroxyl ion, and the Heyrovsky step reacts the intermediate M-H_{ads} with water to form hydrogen, In the Tafel step M-H_{ads} is directly used to produce hydrogen gas. NiCo alloy showed the highest activity for HER in alkaline medium [64].

2.5.5. Electrolyte

The electrolyte plays an important role in improving the efficiency of the AEMWE process. For AEMWE, pure water, 1M KOH, 1M K_2CO_3 and 1M K_2CO_3/$KHCO_3$ is used as the circulating electrolyte.
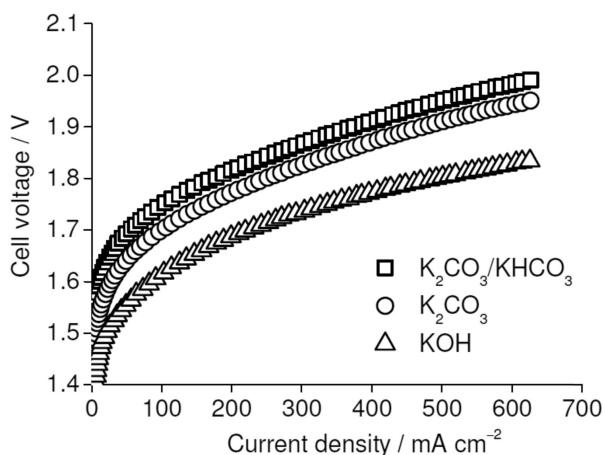
Figure 2.10: Polarization curves obtained while using different electrolyte solutions [16]

1M KOH was found to be the best electrolyte, as pure water has significantly fewer hydroxyl ions, and K_2CO_3 performs better only at lower pH values [12] which has been directly linked to the rate constant of OER [16].

2.5.6. Anion Exchange Membrane (AEM) Introduction

The AEM is one of the key components of the AEMWE setup. It helps in the transport of hydroxyl groups across the cathode to the anode as shown in figure 2.9. Unlike an alkaline water electrolysis separator/membrane, an AEM does not allow the crossover of gases produced at the two sides of the cell. A good AEM must have good ionic conductivity (>100 mS/cm), mechanical, thermal and chemical properties [66]. Section 2.6 explains the stability, components and problems faced by AEMs in more detail as it is the main topic of interest.

2.6. Anion Exchange Membrane (AEM)

This section introduces anion exchange membranes (AEMs) with their components and functions explained in detail. Some commercial AEM are explained with their use in different domains. Later, Poly Co-Aryl Piperidinium polymer is introduced and a benchmark comparison of different membranes. Finally, some state-of-the-art work done on improving AEM performance is given below.

2.6.1. Components of AEM

The AEM has an important function of transporting hydroxyl ions across the MEA. Typically AEM consists of two parts, a main chain polymer backbone and a cationic side group for ion transfer.

Polymer backbone

The AEM backbone is typically made of polymers which provide the chemical stability, mechanical stability and solubility of the AEM. Some polymers used in AEMs are poly-olefins, poly-phenylene, poly-benzimidazolium, and poly-arylene ether as shown in fig 2.11. The transfer of OH^- ions in AEM is relatively slow when compared to H^+ ions in PEM electrolysers, due to moving a bigger and heavier hydroxyl ion. When the AEM absorbs water and swells, the AEM is split into two parts, the hydrophilic channels that conduct the ion transfer and the hydrophobic part that holds the structural integrity of the channels.
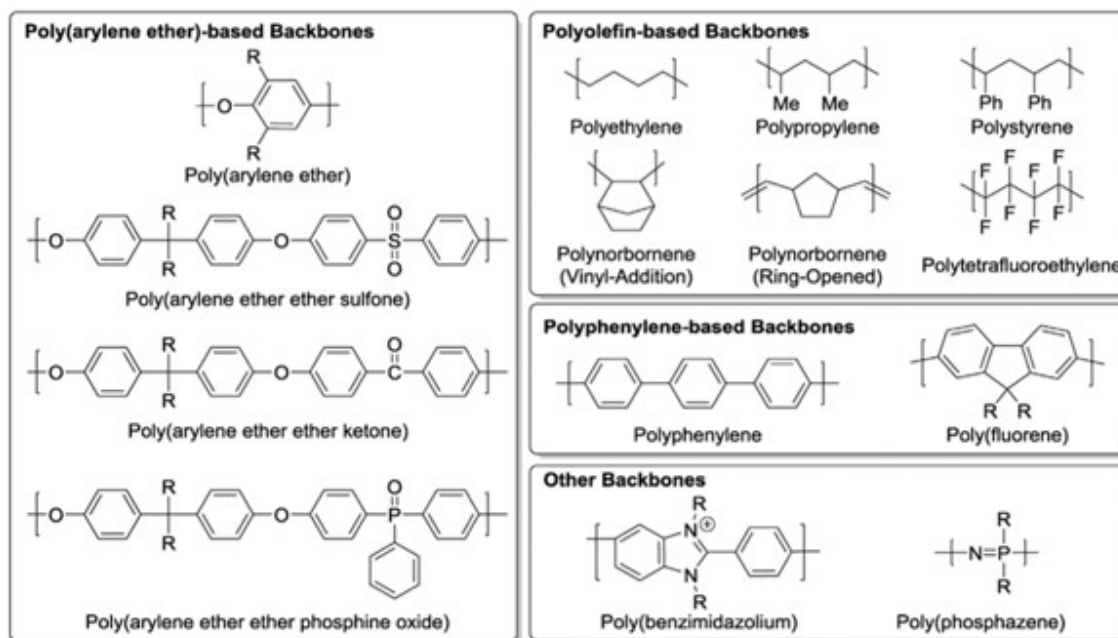
Figure 2.11: Polymer backbones used in AEMs [17]

The stability of the backbone is an important factor for the long-term operation and industry-wide adoption of AEMWE. The presence of cationic groups along the backbone could increase the degradation rate [12]. Studies show that AEM consisting of ether-containing polymers and electron-withdrawing groups in polymers lead to faster degradation of the polymer chains [17]. Studies show that adding long aryl or electron-donating polymer backbone groups to quarternary ammonium or imidazolium head group improves the chemical stability and lifetime of the AEMs even at high temperatures (80° C) [69].

Cationic groups

The cationic head is mainly made up of ammonium, diammonium and phosphonium groups. These groups are hydrophilic and help in conducting the hydroxyl ions and water diffusion through the membrane. Quaternary ammonium (QA) ions are preferred as they have high stability and a simple synthesis route. In contrast, other cationic head groups such as quarternary phosphonium and tertiary sulphonium have been found to have lower thermal and chemical stability when compared to QA groups [17].
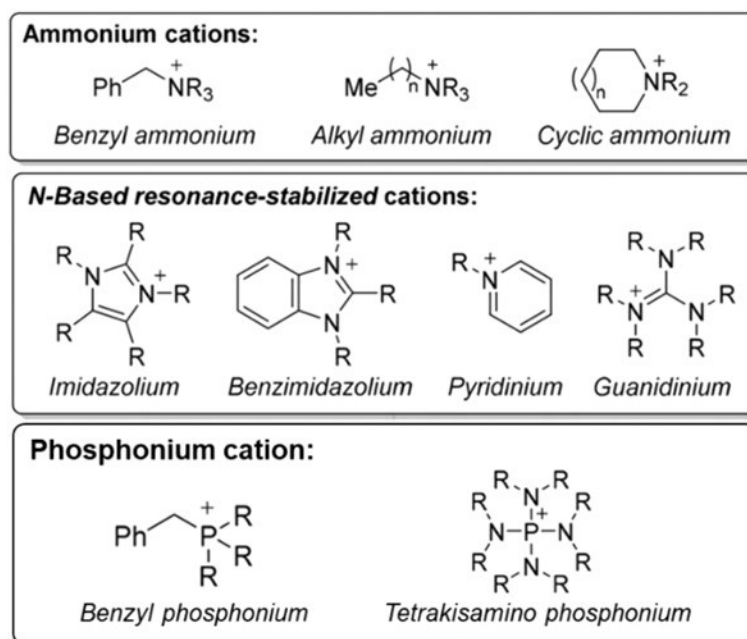
Figure 2.12: Cationic groups used in AEMs [17]

During the AEMWE operation, the quarternary ammonium groups degrade under poor chemical stability as they experience a nucleophile attack due to the sudden increase in hydroxyl groups. The sudden increase in hydroxyl groups could be attributed to the increase in electrolyte concentration due to the consumption of water at the cathode surface [66].

2.6.2. Hydroxyl ion Conductivity in AEM

The most important function of AEM is to conduct OH^- anions. The OH^- ions pass from the cathode side to the anode side through the Grotthuss and vehicular mechanisms. In the Grotthuss proton mechanism, as shown in Fig 2.13, protons are transferred from water molecules to the adjacent OH^- ions. Here, proton holes are transferred from the OH^- ions to water molecules. Hence, the series of proton hole transfer hopping to transport OH^- ions is called the Grotthuss proton mechanism [18].
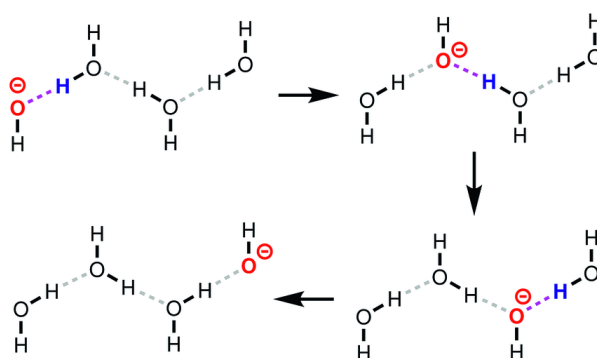
Figure 2.13: Schematics of Grotthuss mechanism for the transport of OH^- ions [18]

The vehicular mechanism is attributed to the standard diffusion of OH^- ions across the AEM. The vehicular mechanism, shown in Fig 2.14 has been found to contribute more than the Grotthuss proton-hopping mechanism for OH^- ions transport.
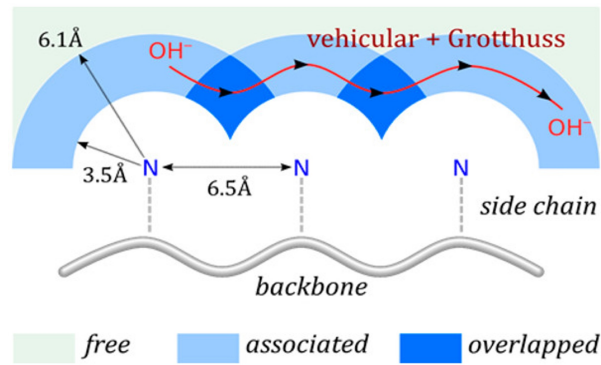
Figure 2.14: Schematics of Grotthuss mechanism combined with Vehicular mechanism for the transport of OH$^-$ ions [15]

Vehicular diffusion and the Grotthuss proton exchange depend on the hydration number of the hydroxyl ions. Hydration number stands for the number of water molecules surrounding the OH$^-$ anion during its movement across the AEM. At low hydration, the transportation of OH$^-$ ions has been found to follow the slower vehicular mechanism, whereas at high hydration the conductivity was determined mainly by the faster Grotthuss mechanism. This highlights the importance of maintaining certain hydration to maintain the operating efficiency of the AEMWE process [66].

2.6.3. AEM applications and potential

AEM's future potential and promising applications in different technologies are listed down below. In addition to being used in anion-exchange membrane water electrolysis (AEMWE) and anion-exchange membrane fuel cells (AEMFC), AEMs could be used in flow batteries, electrocatalytic CO_2 reduction, and electrochemical synthesis of NH_3 [70]. The performance of some AEMs are given in table 2.2 below,

Table 2.2: Comparison of some available AEMs

Membrane	Anode	Cathode	Temperature	Current density @2V (A/cm^2)	Electrolyte	Ref
FAA-3-50	IrO2	Pt/C	80	2.1	1M KOH	[71]
Sustanion 37-50	IrO2	Pt/C	60	1.75	1M KOH	[71]
PFTE Sustanion	IrO2	Pt/C	60	1.90	1M KOH	[71]
QCP-TMA	IrO2	Pt/C	60	4.50	1M KOH	[71]
PCAP-8	IrO2	Pt/C	60	3.50	1M KOH	[71]
PCAP	IrO2	Pt/C	60	7.68	1M KOH	[29]
PCAP	Ni-Fe	Ni-Fe	60	1.2	1M KOH	[32]

2.6.4. Introduction to PCAP

PCAP stands for Poly(co-aryl piperidinium). This class of polymer was first introduced in 2021 when research on biphenyl and terphenyl groups in poly(Aryl Piperidinium) yielded significantly good results [13], [29]. The polymer fell under the spotlight when they were reported to have better current density during AEMWE than state-of-the-art PEMWE by yielding 7.68 A/cm^2 at 2.0 V. [13].
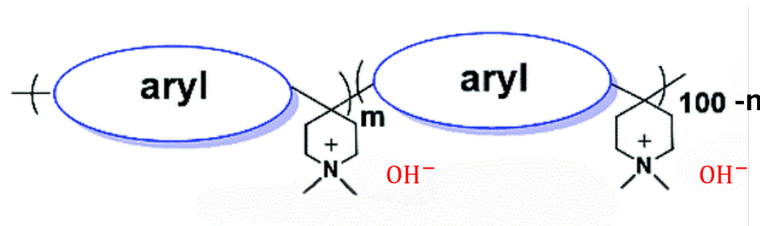
Figure 2.15: PCAP chemical structure [13]

The PCAP polymer shown in fig 2.15 has two different aryl backbone groups. Di-methyl Piperidinium (DMP) is the cationic group for this AEM [29].

2.6.5. State-of-the Art: Improving conductivity in AEMs

The conductivity of an AEM in this context refers to the hydroxyl ion (OH^-) conductivity. Improving the ion conductivity of AEM leads to a decrease in overpotential across the membranes, this is crucial in improving the overall efficiency of the AEMWE process. Some methods that have been used to improve the ion conductivity of the AEMs are given below.

- **Increasing IEC**: The IEC is increased by adding more cationic head groups to the polymer backbone, thereby increasing the ion exchange capacity (IEC). Research on increasing the IEC (mmol/g) of the AEM shows an increase in conductivity but reduces the chemical and mechanical stability due to excessive swelling and degradation of the AEM [72].
- **Changing Cationic group**: Di-methyl piperidinium (DMP) combined with fluorenyl group has a rigid structure with improved phase separation morphology in the AEM. This has increased the mechanical stability and ion conductivity of the polymer AEM. [29].
- **Changing Polymer backbone**: The addition of some aryl groups have been found to increase the rigidity and the phase separation of the AEM [29]. The addition of electron-donating polymer groups to quarternary ammonium groups has been found to increase the alkaline stability of the AEM [69].
- **Aligning the micro-structure**: Aligning the ion channels of poly(2,6-dimethyl-1,4-phenylene oxide) (SPPO) polymer membranes has resulted in a 12 fold increase in ion conductivity [25]. The alignment of polymer PEMs and AEMs to improve the membrane properties is further given below.

This thesis focuses on aligning the microstructure of the polymer to improve the AEM conductivity. Microstructure alignment to improve hydroxyl ion transport and water diffusion can be done using 4 pathways.
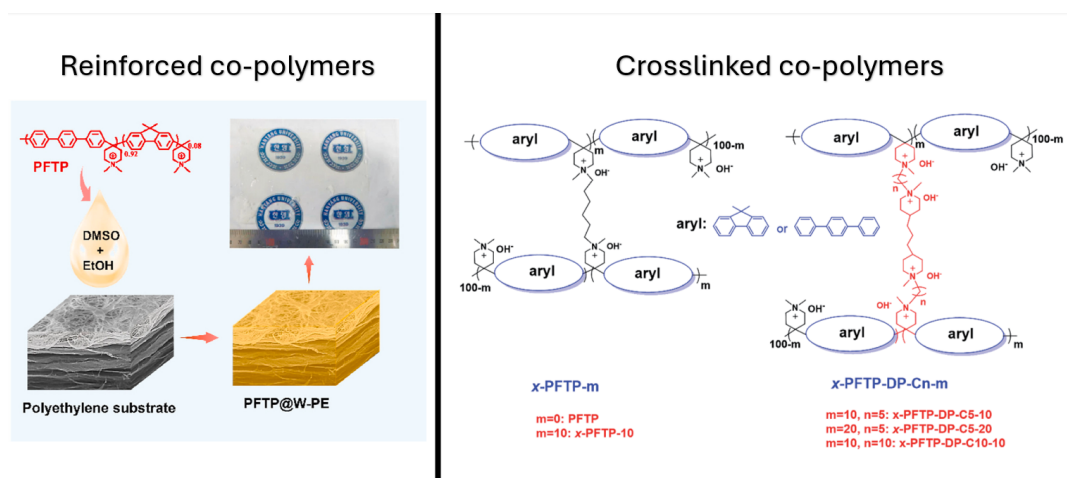
Figure 2.16: Improving ion conductivity using Reinforced co-polymer [19] and Crosslinked co-polymer [20] AEMs

1. Reinforced co-polymers

Studies show that reinforced composite membranes (RCMs) actually improve the mechanical stability of the AEM by reducing the swelling ratio and water uptake. Polyethylene (PE) reinforced PCAP anion-exchange membranes, as shown in fig 2.16 have been found to have excellent mechanical stability while retaining a moderate ion conductivity [19].

2. Crosslinked co-polymers

The PCAP membrane is crosslinked using di-piperidinium, with n and m denoting the length of the alkyl spacer and the degree of crosslinking. These crosslinked AEMs show excellent ion conductivity (> 180

mS/cm), and chemical and mechanical stability. Crosslinking the AEMs also shows an increase in the fuel cell peak power density (PPD) [20].
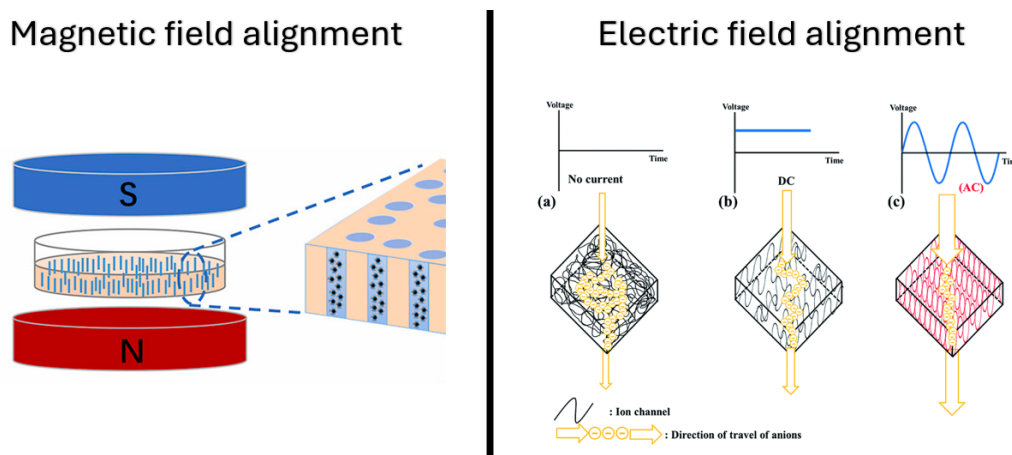
Figure 2.17: Improving ion conductivity by aligning the polymer using a Magnetic field [21] and an Electric field [22]

3. Magnetic field alignment
In this study, Phosphotungstic acid-loaded magnetic nanoparticles are incorporated into sulfonated poly(ether ether ketone) (SPEEK) polymer. The magnetic field applied in the through-plane direction increaaases the ion conductivity by 1.57 times compared to the pristine SPEEK membranes [21].

4. Electric field alignment
The results of improving the ion conductivity through electric field application are given below. An electric field was applied to a bipolar membrane used in a flow battery. Quaternary aminated poly (2,6-dimethyl 1,4-phenylene oxide) (QPPO) solution was poured onto a metal plate where an electric field in the through-plane direction aligned the QPPO polymer. This increased the QPPO conductivity from 26 mS/cm to 120 mS/cm [22].

In another study, A sulfonated poly(2,6-dimethyl-1,4-phenylene oxide) (SPPO) polymer cation-exchange membrane is aligned using an AC electric field. The improvement in conductivity showed a staggering increase from 6 mS/cm for pristine to 207 mS/cm for AC electric field [30].

2.7. Research formulation
A research gap in improving the hydroxyl ion conductivity has been identified during the literature analysis. The research objective is established after the problem statement is identified. Finally, the problem statement is broken down into research questions to answer the research gap.

2.7.1. Identifying research gap
In 2021, research by [32] showed that PCAP AEM had achieved a significant breakthrough when the current density of the AEMWE process reached 7.68 A/cm^2 at 2.0 V. The stability of PCAP showed negligible degradation in voltage when operated at a constant current of 0.5 A/cm^2. This resulted in more focus on improving the microstructure of PCAP even further. [19] has worked on improving the OH$^-$ conductivity by adding a reinforcement polymer. Work on crosslinking [73] and branching [74] the PCAP AEMs have shown positive results, due to an increase in chemical and mechanical stability.

The results from this state-of-the-art research have led us to the current research gap. "Enhancing the conductivity of PCAP". This thesis focuses on improving the conductivity of PCAP by applying an AC electric field in the through-plane direction during the synthesis of the AEM.

2.7.2. Problem statement

> Applying an alternating current (AC) electric field to improve the ion conductivity of an anion-exchange membrane (AEM), while retaining stability, thereby increasing the overall performance of AEM water electrolysis.

2.7.3. Research objective

The Anion Exchange Membrane (AEM) is made of a polymer backbone with cationic functional groups that assist in hydroxide ion conductivity. AEMs have some problems like low durability and low ionic (hydroxyl ion) conductivity. Recent progress in research has been made in improving the mechanical stability, chemical stability, and ionic conductivity of the membrane.

This thesis focuses on increasing the ion-conductivity of the membrane, by applying an electric field in the through-plane direction to align the polymer. Alternating Current is applied in different configurations (Frequency, Electric field strength, and Waveforms), which applies a force on the dipole (cation head and iodide group) present in the AEMs. This aligns the membrane in the through-plane direction, which increases the ion conductivity of the AEM by creating micro-channels and ion pathways that promote hydroxyl conductivity. These changes are made to the AEM without compromising the chemical and mechanical stability.

The characterization of the synthesized membranes would be done by the methods given below.

- **Mechanical characterisation**: Swelling Ratio (SR), Water Uptake (WU), Universal Testing Machine (UTM) and Dynamic mechanical analysis (DMA)
- **Chemical characterisation**: Proton-nuclear magnetic resonance (H-NMR), Fourier-transform infrared spectroscopy (FT-IR), Alkaline stability, and Ion exchange capacity (IEC)
- **Thermal characterisation**: Differential Scanning Calorimetry (DSC) and Thermogravimetric analysis (TGA)
- **Morphology analysis**: Wide-angle x-ray scattering (WAXS) and Atomic force microscopy (AFM)

Finally, the AEMs produced are tested in a single zero-gap electrolyser by performing different electrochemical techniques. Linear sweep voltammetry (LSV) is conducted to measure the ion conductivity of the membrane. Chrono-amperometry (CA) is conducted to measure the (short-term) stability of the membrane, and Cyclic voltammetry (CV) is done to obtain the polarisation curves which present us with the limiting current density at a given voltage. Finally, electrochemical impedance spectroscopy is used to measure the different resistances of the membrane.

2.7.4. Research question

Combining the answers to the research question leads to the solution for the problem identified in the research objective.

> 1. How does the polymer align in the presence of an electric field?

> 2. What is the performance of pristine and electrically aligned AEM during electrolysis ?

> 3. What are the "ideal" AC parameters to electrically align the PCAP polymer?

> 4. What are the methods to characterise the pristine and electrically aligned membranes ?

> 5. How do we determine the stability of the PCAP AEM?

3

Experimental Framework

This chapter gives an introduction to all the experimental setups and methodologies used. Section 3.1 explains the complete AEM synthesis process from membrane casting to activation. Section 3.2 explains the principle of polymer alignment using an electric field and the alignment in the through-plane direction. Section 3.3 introduces the different characterisation techniques used to analyse the polymer membrane. Finally, Section 3.4 explains the different electrochemical setups and techniques performed to test the performance of different PCAP AEMs during water electrolysis.

3.1. AEM synthesis

The AEM synthesis consists mainly of four parts. The first and second step involves preparing the polymer solution followed by the casting setup preparation to produce electrically aligned membranes. The third part explains the casting of the polymer solution followed by the drying and activation in the final part.

3.1.1. Polymer solution preparation

The Poly(co-aryl piperidinium) (PCAP) polymer solution is prepared with the right viscosity for casting into thin membranes. PCAP polymer present in the iodide form as shown in fig 3.1b is dissolved in dimethyl sulfoxide (DMSO) to produce a 22 wt % PCAP polymer solution. The polymer solution is stirred at 45°C for 3 hours. Finally, the polymer solution is left overnight to remove the air bubbles produced during stirring. This process could be sped up using a desiccator and a vacuum pump.

(a) PCAP in the I⁻ form

(b) Preparing the stainless steel casting plate and PCAP solutin
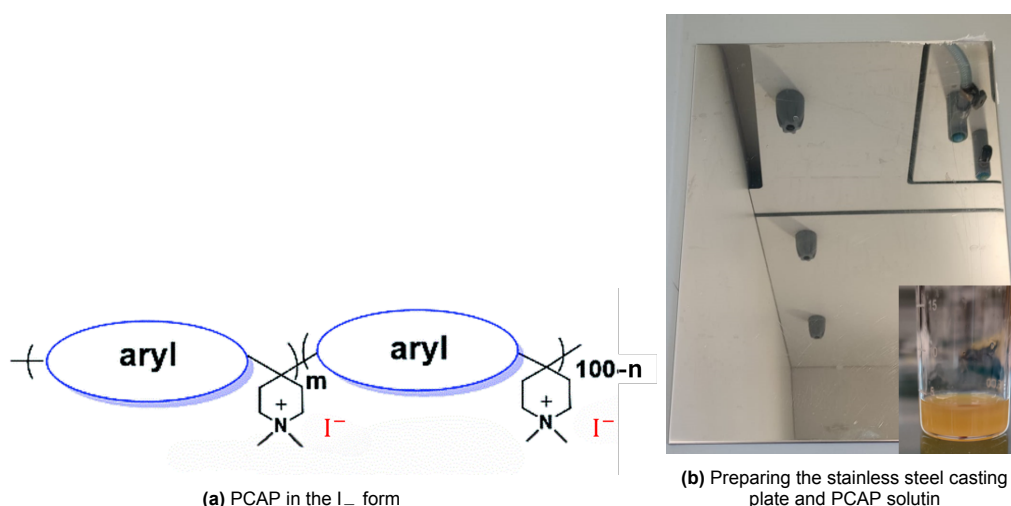
Figure 3.1: Polymer solution preparation

A smooth stainless steel plate with a mirror finish shown in figure 3.1b is used for casting the AEMs.

The casting plate used in this method must be electrically conductive. A few drops of DMSO are added to the casting plate to dissolve the leftover PCAP after which the plate is washed with acetone. The plates are completely cleaned three times using acetone to remove the trace DMSO and impurities.

3.1.2. Casting setup preparation

The electrically assisted membrane casting setup consists of four main components, as shown in fig 3.2: A doctor blade setup, a function generator, an oscilloscope, and a multi-meter. The functions of these four components are given below,
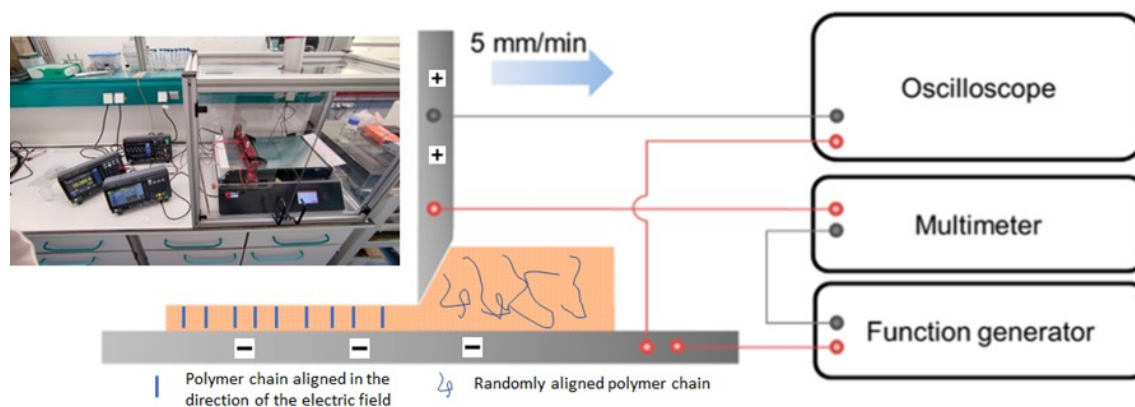
Figure 3.2: Schematics of the doctor blade setup

Doctor blade setup

The doctor blade setup (fig 3.2) consists of a moving hand, an adjustable doctor blade, and a casting plate. The adjustable doctor blade only has a conductive blade part, whereas the other parts such as the body and support do not conduct electricity. This prevents a short circuit when a voltage is applied across the setup.

Function generator

The function generator (fig 3.2) generates the for the casting setup. Its functions also include adjusting the parameters of the electric field applied between two parts. Some of the programmable parameters are voltage, frequency, and waveform of the given electric signal.

Oscilloscope

The Oscilloscope (fig 3.2) displays the resulting electric voltage applied between the casting plate and the doctor blade by the function generator. It can be used to track multiple parameters such as peak-peak voltage, root mean square (RMS) voltage, frequency, and waveform during the application of the electric field.

Multi-meter

The multi-meter shown in fig 3.2 records the resulting electric current produced, across the membrane, between the casting plate and the doctor blade. They can be used to measure the voltage, current, resistance, and capacitance. The signals from the multi-meter is used to find the alignment of the polymer as discussed in section 3.2.

3.1.3. Casting the AEM

The polymer solution is poured next to the blade in a 2cm x 2cm square-shaped droplet after which the setup is turned on. The casting plate is clamped into a fixed position once the setup is turned on. The moving hand in the setup moves the doctor blade at a constant rate. The voltage source is turned on once the doctor blade comes in contact with the polymer on the plate.

The doctor blade setup is connected with all the positive components potential and the negative potential of the function generator, oscilloscope and multi-meter is connected to the casting plate. This

creates an electric field as shown in fig 3.5 between the doctor blade and the plate where the alignment takes place in the direction of the applied electric field.

3.1.4. Drying and activation of the AEM

Once the electrically aligned polymer AEM is cast using a doctor blade setup, The casting plate is removed and the AEM with DMSO in the polymer matrix is dried in a hot oven at 80° C for 12 hours. The dry membrane is soaked in water for 30 minutes, after which they are peeled from the casting plate. Finally, Water is removed from the peeled membrane by drying it in a vacuum oven at 40° C for 16 hours.
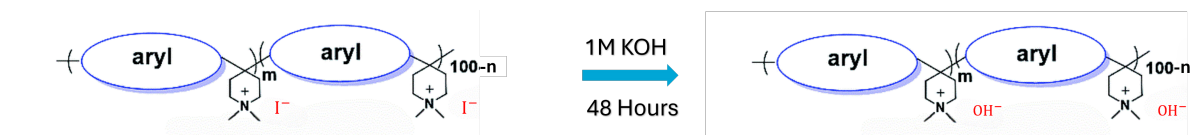
Figure 3.3: Activation of the AEM for electrolysis [23]

To begin experimental work on the synthesized AEM, the PCAP-I$_-$ membranes are soaked in the electrolyte to activate the membrane. Activation refers to changing the PCAP in I$^-$ form to OH$^-$ as shown in fig 3.3. This is done by soaking the polymer in 1M KOH with an abundance of OH$^-$ ions for 48 hours. The activation time was determined with the results from ion exchange capacity and swelling ratio. The activated polymer is then used in the AEM water electrolysis process to produce hydrogen and oxygen gases.

3.2. Applying Electric field

In this section, the principle of aligning the charged AEM is explained. The different setups used for a through-plane and in-plane alignment are discussed further. Finally, the membranes planned are presented in a table for better understanding.

3.2.1. Principle of electric field alignment

In this work, an electric field is applied to fabricate uniform ion channels in a desired direction. A dimethyl-piperidinium (DMP) cationic group with a positive charge and an iodine group with a negative charge act as a counter-ion with a negative charge. The DMP is bound to the polymer as shown in fig 3.3 is considered. The two charged form a dipole (fig 3.4) which could be moved through an external electric field.
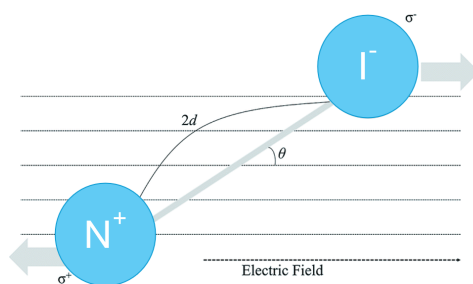
Figure 3.4: A dipole in the polymer solution under an external electric field [24]

The energy experienced by the dipole in an electric field is calculated using the equation given below [24].

$$E_{rot} = nEqd(1 - cos\Theta)$$

Here the rotational energy (E_{rot}) is obtained from the number of dipoles (n), the external electric field (E), the charge (q), the distance between two dipoles (d), and the dipole angle between the electric field and the dipole (θ).

3.2.2. Alignment in the through-plane direction

The PCAP polymer forms a dipole in the I^- form as shown in fig 3.4. In the doctor blade setup, the electric field is applied in the direction perpendicular to the casting plate. The application of an electric field inside the polymer plane is called through-plane direction (fig 3.5). The doctor blade moves at a constant speed. The electric field produced by the function generator is applied in the through-plane direction using the doctor blade and the stainless steel casting plate to produce an aligned membrane.
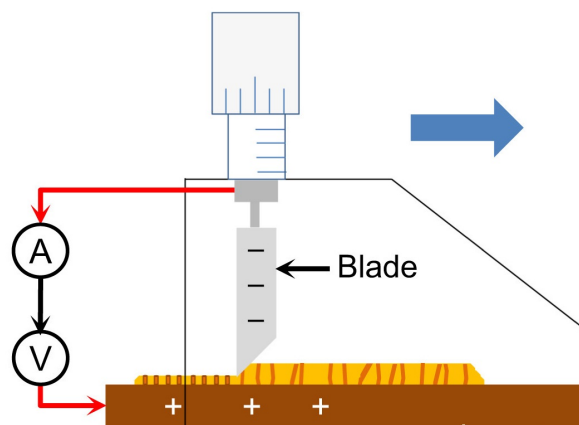
Figure 3.5: Through-plane polymer alignment using doctor blade [25]

The polymer membranes are cast using different parameters. Table 4.1 gives the different conditions used to cast the AEMs. For this thesis three parameters are tested for optimization.

- Electric field strength (V/cm): This value is calculated using the applied absolute voltage and the doctor blade height. This represents the magnitude of force applied to the dipole.
- Frequency (Hz): This is related to the movement frequency of the dipoles.
- Waveform: This determines the magnitude of the force experienced by the dipole with time.

The electric field strength for AC signals is calculated using the V_{RMS}, an equivalent to V_{DC}. The V_{RMS} mean is the root mean squared voltage of the AC waveform taken into consideration. This is taken to calculate the total energy applied to the dipole.

Table 3.1: Planned membranes for synthesis with different parameters

Membrane	Electric field strength (V/cm)	Frequency (Hz)	Waveform
MPris	0	0	0
Variable: Electric field strength (V/cm)			
ME1	8	100	Sin
ME2	32	100	Sin
ME3	45	100	Sin
ME4	60	100	Sin
ME5	75	100	Sin
Variable: Frequency (kHz)			
MF1	8	100	Sin
MF2	8	1000	Sin
MF3	8	10000	Sin
MF4	8	100000	Sin
Variable: Waveform			
MW1	8	100	Sin
MW2	8	100	Square

3.3. AEM characterisation

In this section, The stability of AEMs produced during casting and the properties of the AEMs are determined using various characterisation techniques. The membranes are classified based on mechanical, chemical and thermal characterisation techniques as given in fig 3.6. Finally, the morphology of the AEM is obtained using AFM.
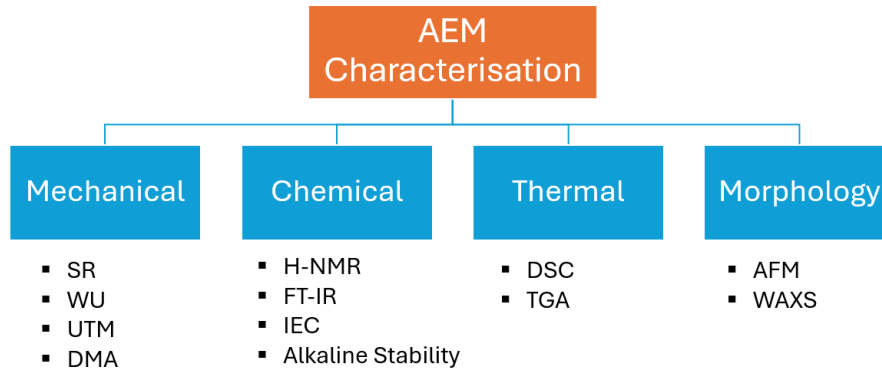
Figure 3.6: Classification of different characterisation techniques used in this thesis

3.3.1. Mechanical characterisation

The mechanical properties of different AEMs are measured to see the rigidity and the strength of the membrane.

1. Swelling Ratio (SR): Thickness change

The swelling ratio is a parameter used in determining the dimensional stability of the membrane. It is calculated by comparing the thickness of the wet polymer and the dry polymer. The wet thickness is calculated using a digital micrometer after the PCAP AEM is soaked in 1M KOH for 48 hours. The dry thickness is obtained after the sample is washed in DI water and dried in a vacuum oven for 16 hours at 40°C [72].

$$SR = \frac{L_{wet} - L_{dry}}{L_{dry}} * 100 (\%)$$

SR calculated from the equation given shows that PCAP membranes with thickness around 20±5 μm have an SR of 16±3 % [29].

2. Water Uptake (WU): Mass change

Water uptake of the different AEM are calculated by comparing the weight of the dry sample and the activated wet sample. The wet weight of the sample was obtained after the sample was soaked in 1M KOH for 48 hours. The dry weight of the sample is obtained after the sample is washed in DI water and dried in a vacuum oven for 16 hours at 40°C.

$$WU = \frac{M_{wet} - M_{dry}}{M_{dry}} * 100 (\%)$$

The WU is calculated using the equation described above. Research on PCAP membranes with thickness around 20±5 μm show a WU of 45±5 % [29].

3.3.2. Chemical characterisation

The chemical characterisation is done to obtain data on the chemical stability of the polymer AEMs. Another important purpose of these characterisation techniques is to examine the degradation of the AEM synthesized using an AC electric field.

1. Proton-Nuclear Magnetic Resonance (H-NMR)

The H-NMR is a technique where the different proton nuclei within the molecules are identified to determine the chemical structure. First, the protons are aligned with a magnetic field (3.7). Second, small

perturbations (disturbances) in the form of radio frequency energy are caused by a weak oscillating magnetic field. Finally, the electromagnetic waves emitted by the nuclei due to this perturbation is detected and analysed [26].
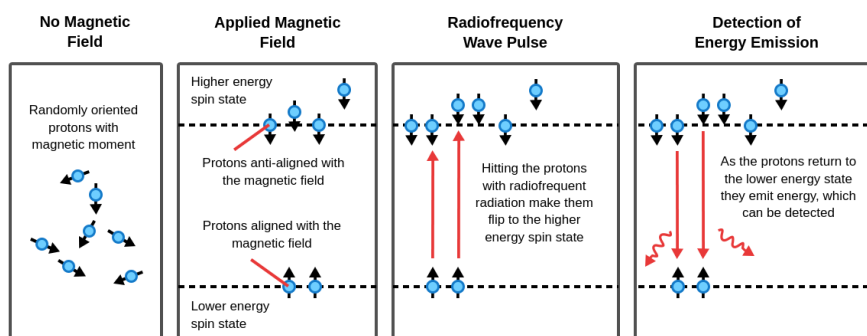
Figure 3.7: Operating principle of H-NMR spectroscopy [26]

The chemical structures of the AEMs are confirmed using he H-NMR device. A piece of the reference membrane is dissolved in d6-DMSO, the solvent. To eliminate the water peaks 20 µl of TFA is added inside the solution. The solution is stirred for 1 hour and then poured inside clean NMR tubes for analysis [29].

2. Fourier-Transform Infrared Spectroscopy (FT-IR)

The FT-IR spectroscopy is a technique where beams of light with various frequencies are shined on the sample and the absorption of light in each wavelength is recorded to identify the different bonds present in the sample [27].
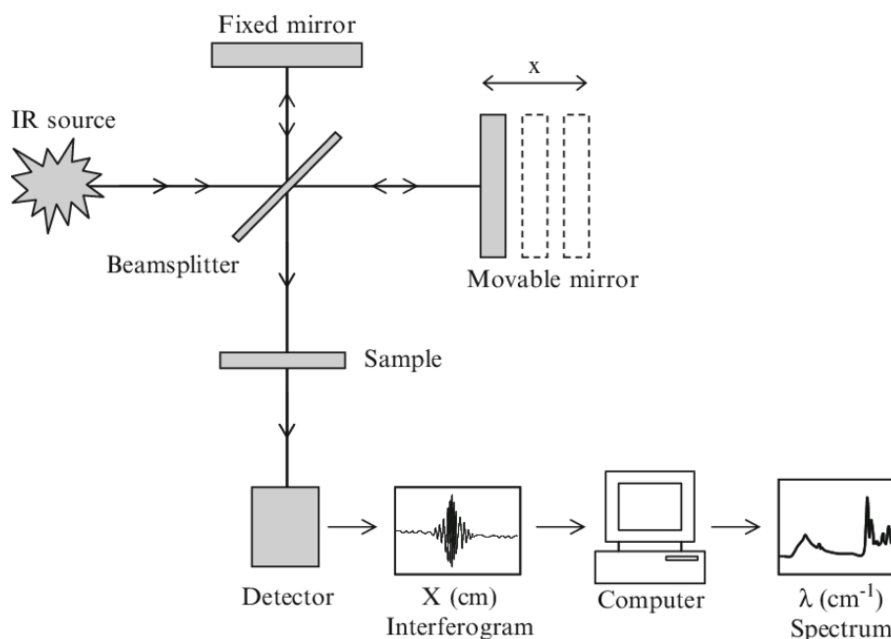
Figure 3.8: Operating principle of FT-IR spectroscopy [27]

Fourier transform converts the interferogram data in the time domain to the frequency domain 3.8. Here, each wavelength's absorbance or transmittance is seen and could be further analysed to verify if new bonds are created in the electrically aligned polymer membranes [72].

3. Ion Exchange Capacity (IEC)

The Ion Exchange Capacity of the polymer is used to determine the concentration of cationic side

groups present in the polymer. These side groups provide the exchange sites for OH^- transport across the AEM. Initially, the functional group of the membrane that exists as I^- form, are replaced by Cl^- by soaking the sample in 40ml 1M NaCl for 48 hours. The membrane is taken out and washed thoroughly using deionized (DI) water to remove the NaCl present on the surface. The membrane in the Cl^- form is converted to CO_3^{2-} by soaking the membrane in 1M $NaNO_3$ for 48 hours.
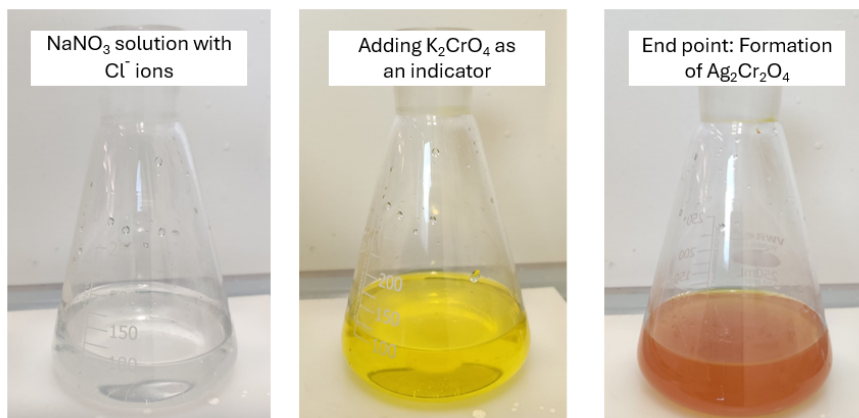
Figure 3.9: Determining the IEC using Mohr's titration

Finally, The concentration of chloride (Cl^-) ions in the $NaNO_3$ solution is titrated using 0.02266M silver nitrate ($AgNO_3$) to obtain the IEC values [29]. Potassium Chromate K_2CrO_4 is used as an indicator, where the initial colour of yellow changes to brick red due to the formation of AgCl precipitate [75]. The IEC values are calculated by using the equation given below.

$$IEC \left(\frac{mmol}{g} \right) = \frac{V_{AgNO_3} * C_{AgNO_3}}{m_{dry}}$$

Here, the concentration of $AgNO_3$ (C_{AgNO_3}), the volume of $AgNO_3$ (V_{AgNO_3}), and the dry weight (m_{dry}) is used to calculate the IEC.

4. Alkaline stability

The alkaline stability of the membrane is done to verify the chemical stability of the membrane in the electrolyte during AEMWE operation. During electrolysis, the concentration of electrolyte increases at the contact surface of the electrocatalyst and the membrane, and has been found to vary between 1 M and 5 M. This is due to the decrease in local water concentration at the cathode during water splitting [66].

Here, 4 samples of electrically modified membranes are prepared to be analysed. Every sample undergoes 2 chemical characterisation tests FT-IR and H-NMR. The base FT-IR and H-NMR are obtained from the first sample. The second, third and fourth samples are soaked in 1M, 5M and 10M KOH respectively. The samples are left inside the electrolytes for 300 hours before the final analysis. In the end, an FT-IT is done on all the membranes before they are dissolved in d6-DMSO for H-NMR spectroscopy [29].

3.3.3. Thermal characterisation

The thermal characterisation of the polymer AEM is done to obtain data on the glass transition temperature and high-temperature stability of the electrically aligned membranes.

1. Differential scanning calorimetry (DSC)

The DSC is a technique where the difference in heat capacity of the sample and the reference is measured as a function of temperature. Heat capacity refers to the energy in the form of heat required to increase the temperature of the sample by 1°C. The reference considered here must be stable at

different temperatures and must have a stable heat capacity over the range of different temperatures [76].

In the heat flux DSC setup, the changes in heat flow are measured between the sample and the reference crucible to obtain data on different parameters such as the glass transition temperature (T_g). When a polymer crosses the glass transition temperature the amorphous rigid phase of the polymer turns to a rubbery phase as shown in fig 3.10. This is due to an increased mobility of the ions at high temperatures and an increase in heat capacity. This change in heat capacity is used to determine the T_g of the polymer [77].
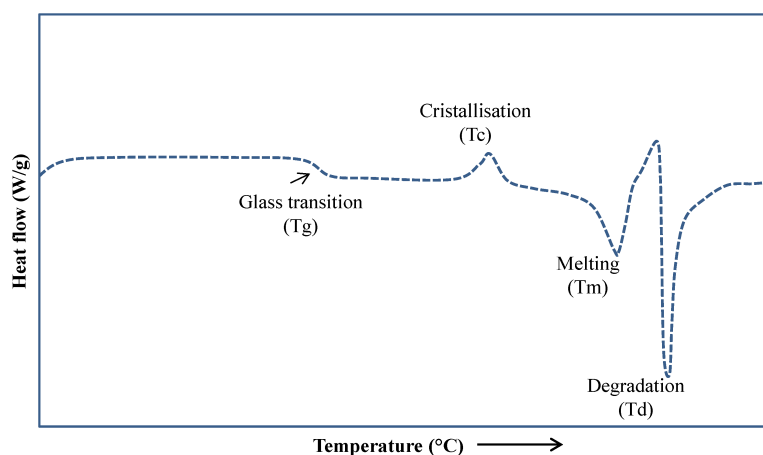
Figure 3.10: Schematic of different thermal transition obtained from DSC [28]

The T_g of a polymer is measured to determine the curing temperature of the PCAP cast polymer matrix. Studies have shown that the cast structure is not maintained when the curing temperature is above the T_g [29]. DSC is also done to notice a trend in the crystallinity of the polymer AEM cast using an AC electric field.

2. Thermo Gravimetry Analysis (TGA)

The TGA is a technique for measuring the thermal stability of the sample. Here, the mass of the sample is measured over time with constant temperature change. TGA is used to measure the thermal degradation of the different components in the PCAP polymer sample [78].
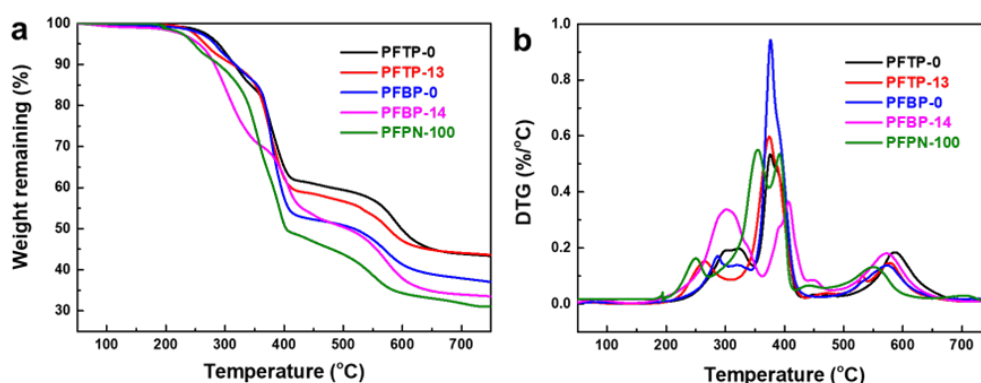
Figure 3.11: TGA and DTG plot of different anion exchange membranes under an inert (N_2) atmosphere [29]

In this study, a small piece of sample is cut and placed on a clean crucible for analysis. The sample is heated from 30 to 800° C at a heating rate of 10° C/min. The results obtained from TGA could be used to plot the derivative thermogravimetry (DTG), as shown in fig 3.11, to understand the thermal degradation route of the AEM polymer [29].

3.3.4. Morphology analysis

The morphology characterisation is used to understand the surface morphology of the polymer sample. It is also used to analyse the final structure created by the AC electric field.

Atomic Force Microscopy

The AFM is a type of microscopy that uses a sharp probe (tip) to analyse nanoscale structures and surface morphology. In the tapping AFM mode, the tip oscillating at a fixed frequency is moved across the sample surface. A laser is shone on the back of the tip, which is reflected to a position-sensitive detector that measures the displacement of the tip and records the surface morphology [79].
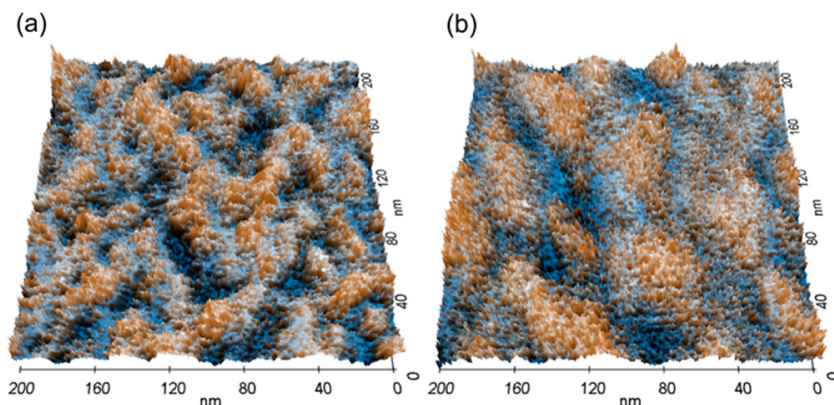
Figure 3.12: AFM images of the (a) pristine membrane (b) electrically aligned membrane [30]

In this thesis, The membranes synthesized using the in-plane setup are analysed using an AFM under tapping mode. AFM analysis is done on the activated polymer in the OH^- form (dry state). Research shows that ion channels are formed, as shown in fig 3.12, during the application of an electric field in polymers in the in-plane direction.

3.4. Electrochemical testing

In this section, the electrochemical testing which gives an insight into the performance of the membrane AEMWE is briefly explained. Two different setups are used to measure different properties of the membranes such as the ion conductivity, polarisation curves, ohmic resistance, and charge transfer resistance [29], [32].

3.4.1. Ion Conductivity (IC) setup

The hydroxyl ion (OH^-) conductivity of the synthesized membranes is measured using using a four-probe cell. The membrane is initially soaked in 1M KOH for 48 hours for activation. Later, the surface of the membrane is cleaned with DI water and placed in the IC setup [32].

First, the membrane is placed between the anode and the cathode compartments. The electrolyte is circulated into the setup with a flow rate of 15.5 ml/min. The reference and the sense electrodes are placed at the ends of the two capillaries. Finally, the four electrodes the working, the counter, the reference, and the sense electrodes are connected to the potentiostat setup as shown in fig 3.13(left) to prepare for the electrochemical tests.
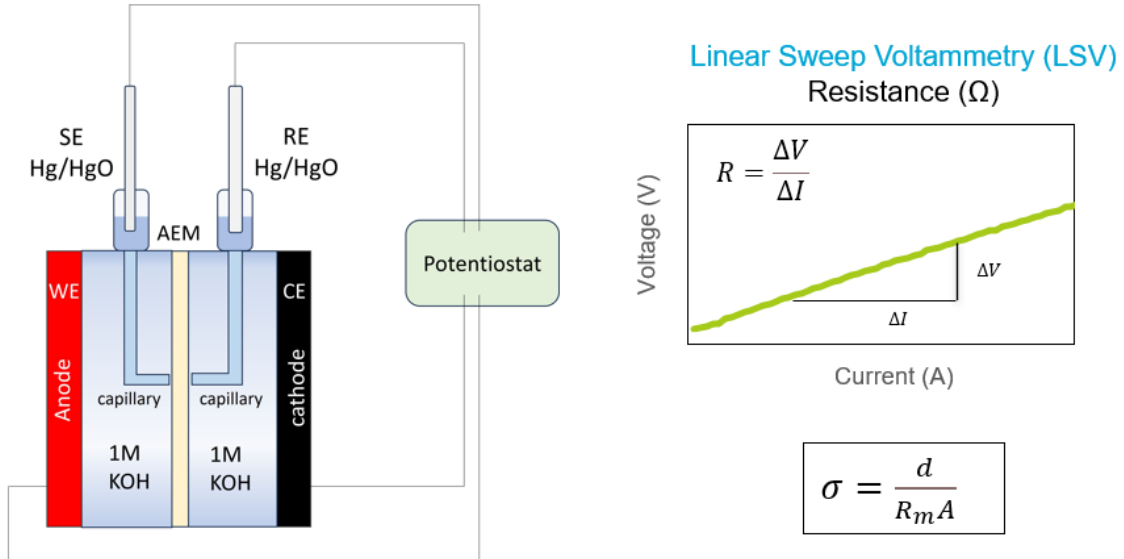
Figure 3.13: Schematics of the Ion conductivity setup and the LSV plot for the resistance calculation

In this test, the four-probe cell is connected to a potentiostat and a 10-A booster from Metrohm [80] to run the experiments. The ion conductivity measurement is done using linear sweep voltammetry (LSV). A small current is applied to the cell and the resulting voltage is measured to obtain a current-voltage (I-V) plot. The slope obtained from the I-V plot shown in fig 3.13 gives the overall resistance ($R_{overall}$) of the cell.

$$R_{overall} = R_{blank} + R_m$$

Here, a blank run is done without an AEM to obtain the blank resistance (R_{blank}). The membrane resistance (R_m) is calculated using the equation given above. Finally, the ion conductivity σ (mS/cm), is found using the thickness of the membrane (d[cm]), the membrane resistance ($R_m[\Omega]$, and the membrane area (A[cm^2]) [25].

3.4.2. Electrolyser setup

The electrolyser setup used in this thesis is a zero-gap single-cell setup that operates under industrial AEM water electrolysis conditions (60°C). The schematics of the setup are given below in fig 3.14. The main components of the AEMWE explained in 2.5 are the electrolyser, the pump, the heating pad, two heating plates, and a potentiostat with a 10A booster. Some electrochemical tests done using this setup are cyclic voltammetry (CV), chrono-potentiometry (CP), and electrochemical impedance spectroscopy (EIS) at different temperatures. [29].

The setup preparation begins with loading the anode and cathode electrocatalysts on the AEM. The catalysts are loaded on the polymer using the catalyst-coated substrate (CCS) method, where the gas diffusion layers (nickel felt) with a small layer of anode and cathode electrocatalyst are placed on both sides of the membrane. NiFeO$_4$ and NiFeCo are used as anode and cathode electrocatalysts respectively. The zero-gap cell is assembled with appropriate gaskets. An electrolyte, 1M KOH, with a flow rate of 10ml/min is used for all the zero-gap electrochemical tests.

The electrolyser setup could be run at room temperature (20°C) and 60°C respectively as the activation energy for OH$^-$ diffusion in AEMs exhibit Arrhenius behaviour at elevated temperatures [15]. This could be done by using the heating pad and a thermocouple connected to the body of the cell as shown in Fig 3.14.
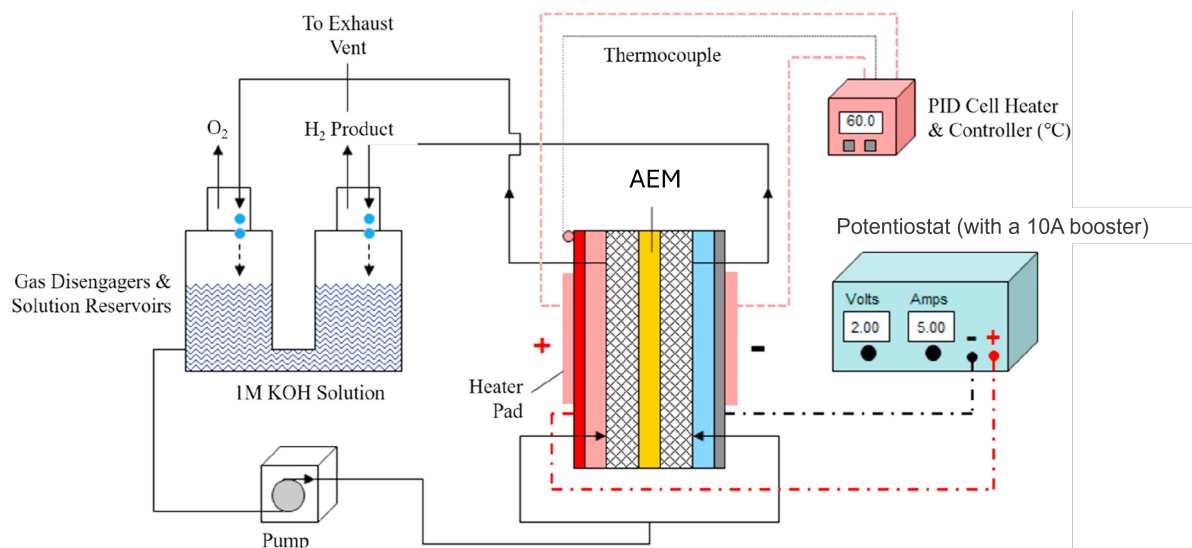
Figure 3.14: Schematics of a single cell AEMWE testing setup [31]

Cyclic voltammetry (CV)

The CV is an electrochemical test where an increasing potential is applied to a zero-gap electrochemical cell and the resulting current is measured. The potential is applied between the initial potential (E_i) and the final potential (E_f), at a set ramp rate (V/s). Here, unlike linear sweep voltammetry, once the E_f is reached the working potential starts going in the opposite direction to return to E_i [81].
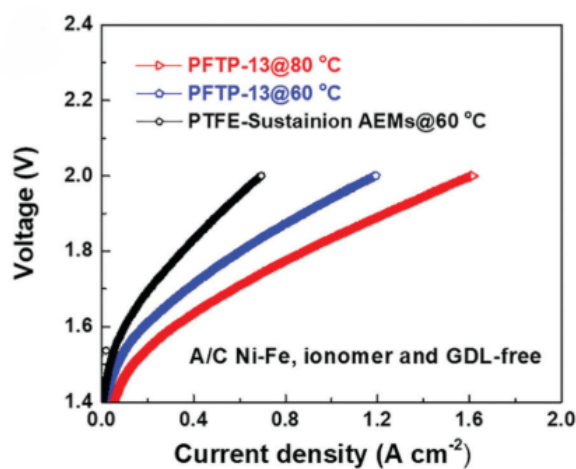
Figure 3.15: Polarisation curves of PCAP AEMs at different temperatures in 1M KOH [32]

In this experiment, the CV is run between 1.3 V and 2.3 V, at a ramp rate of 0.00244 V/s. The data obtained during the CV is used to plot the polarisation current density. This is mainly used to measure the maximum current density obtained at a given voltage. The polarisation curves of different membranes are plotted together, as shown in fig 3.15, to compare and select an AEM with the best performance [32].

Chrono Potentiometry (CP)

In CP, the current is kept constant at the working electrode and the potential is measured over time. The CP is run for 2000 seconds to verify the system's equilibrium. This is an important technique in determining the steady state of the zero-gap AEMWE system mainly during the three scenarios described below [82].

- Determining the system stability When the electrocatalysts are loaded on both sides of the MEA (short-term) using the catalyst-coated substrate (CCS) method.
- Determining the system stability when the temperature of the AEM water electrolysis setup is changed (short-term).
- Determining the stability of the membrane (long-term) when the AEM water electrolysis system is in operation.

Electrochemical Impedance Spectroscopy (EIS)

The EIS is a technique that measures the impedance of the AEMWE system at different frequencies. The EIS impedance values could be used to identify and quantify various losses in a cell such as ohmic loss, charge transfer loss and mass transport loss. The impedance values are evaluated by plotting the Nyquist plot as shown in fig 3.16 [11].
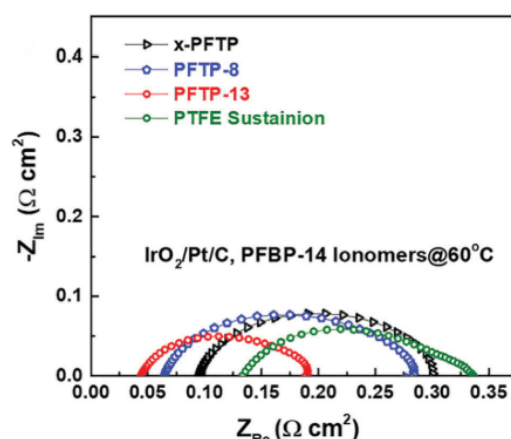
Figure 3.16: A Nyquist plot obtained from the EIS spectra [32]

In this thesis, EIS measurements are done at 1.8 V at room temperature (RT). As shown in fig 3.16, the initial intercept point of the Nyquist plot at high frequencies is the ohmic resistance, and the diameter of the semi-circle represents the charge transfer resistance. The improvements in the reduction of ohmic loss and charge transfer losses at high alignment could be determined using this technique [32].

4

Results and Discussion

This chapter presents the results obtained from the characterisation techniques and the information inferred from them. Section 4.1 briefly explains the membrane preparation. Section 4.2 presents the electrochemical results of the different electrochemical techniques performed. The results from mechanical, chemical and thermal characterisation techniques are presented in sections 4.3, 4.4 and 4.5. Section 4.6 gives us the morphology of the membrane.

4.1. Membrane preparation

This section explains the casting parameters used and the method for preparing and activating the membrane for AEM electrolysis.

4.1.1. Casting: Doctor blade thickness (H_{blade})

In this experiment, the casting thickness of the doctor blade height is optimised. The wet thickness needed for operating at medium-pressure (30 bar) AEM water electrolysis is 40 to 50 microns [83]. The doctor blade height determining the thickness of the wet membrane is given here.
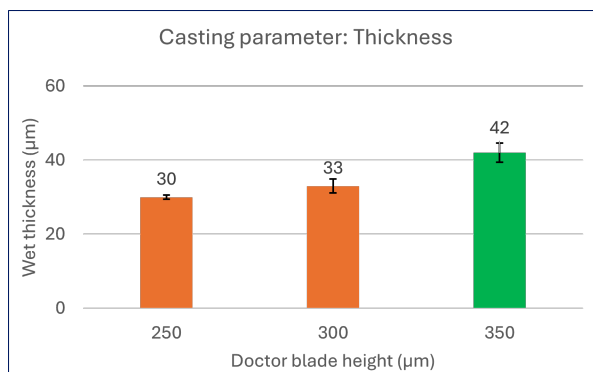
Figure 4.1: Dry AEM thickness obtained for different doctor blade height

The doctor blade thickness (H_{blade}) used to produce an AEM with a wet thickness between 40 and 50 microns was found to be 350 microns as shown in fig 4.1

4.1.2. Membrane activation

To determine the right activation time of the PCAP membrane, IEC and SR are done on the pristine membrane under different time scales as shown in fig 4.2.
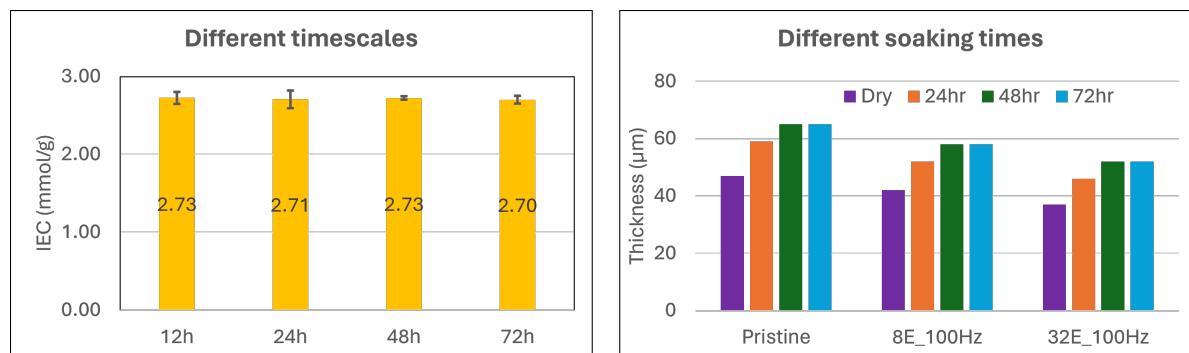
Figure 4.2: Activation time calculated from IEC (left) and swelling (right)

The IEC results shown in fig 4.2 explain that the membrane activation happens before 12 hours. However, the difference in wet thickness measured with different soaking times shows that the swelling of the membrane only stops after 48 hours as seen in fig 4.2. Although all the I^- ions are replaced by OH^- ions, the membrane is allowed to swell as preventing the swelling of membranes may additional stress and eventually damage the membrane. Hence, the activation time (t_{act}) of the PCAP membrane was fixed as 48 hours,

4.2. Electrochemcial testing

In this section, the AEMs synthesized by applying an AC electric field are tested for their ion conductivity and AEM water electrolyser performance.

4.2.1. Ion Conductivity (IC)

The IC values of the AEM are obtained from the two-compartment setup using linear sweep voltammetry (LSV). The results obtained after processing the LSV data gives the IC of the membrane.

#	Pristine	8E-100Hz	32E-100Hz	45E-100Hz	60E-100Hz	75E-100Hz
μm	65 ± 3	49 ± 2	52 ± 3	50 ± 2	66 ± 3	44 ± 2
V_{DC}	0 V	0.3 V	1.1 V	1.6 V	2.1 V	2.6 V
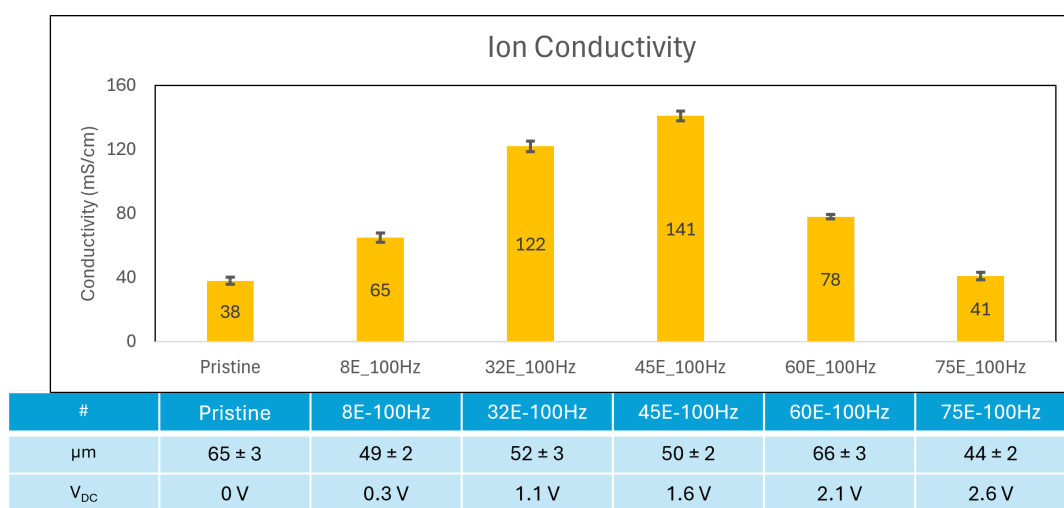
Figure 4.3: Ion Conductivity of membranes with different electric field strength

In the modifying electric field (ME) series, the ion conductivity increases with increasing electric field strength until it reaches an electric field strength of 45V/cm. The reason for an improvement in IC could be attributed to the increase in force applied to the molecule by changing the electric field strength.

When the electric field strength crosses above 75 V/cm a visible colour change of the polymer membrane is visible during casting as shown in fig 4.4. This could be due to the degradation of the piperidinium groups by the ring-opening reaction due to nucleophilic substitution or Hoffmann elimination [17]. Another reason could be the replacement of I^- ions in the polymer by the OH^- when water splitting happens at high voltages.
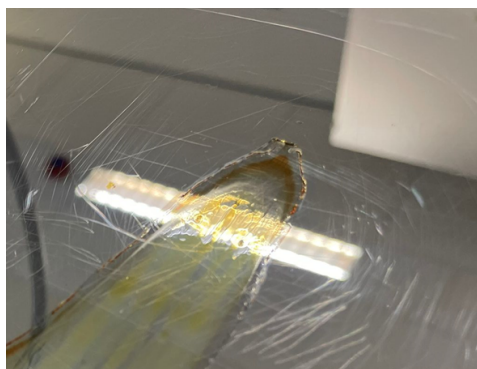
Figure 4.4: Degradation of the polymer AEM when applying higher electric field strength

#	Pristine	8E-100Hz	8E-1000Hz	8E-10000Hz	8E-100000Hz
μm	65 ± 3	49 ± 2	25 ± 2	59 ± 2	35 ± 3
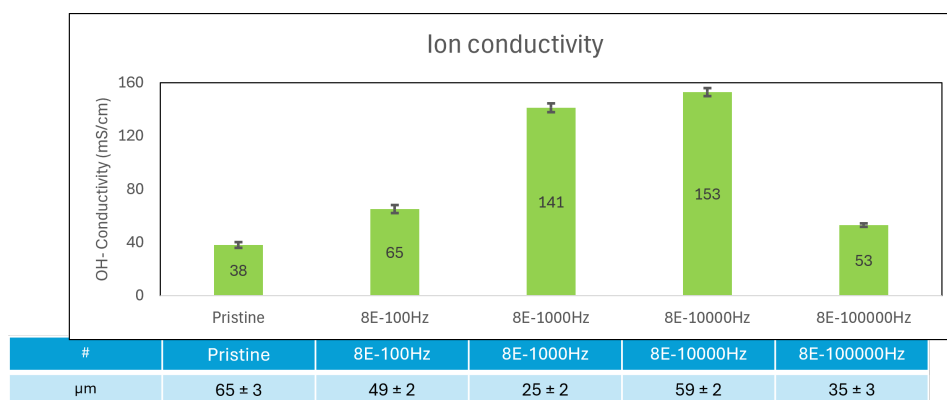
Figure 4.5: Ion Conductivity of membranes with different frequency

In the modifying frequency (MF) series, the frequency is increased exponentially from 100 Hz to 100000 Hz. The ion conductivity data obtained shows that the conductivity value increases until 10000Hz and decreases rapidly after that. This could be attributed to alignment when an increase in the overall energy is applied to the molecule.

#	Pristine	8E-100Hz-Sin	8E-100Hz-Square
μm	65 ± 3	49 ± 2	66 ± 2
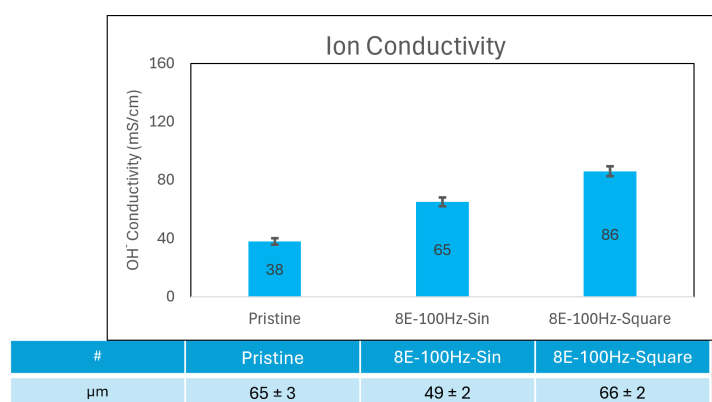
Figure 4.6: Ion Conductivity of membranes with different waveform

In the modifying waveform (MW) series, a square waveform is applied while AEM synthesis. This AEM shows a small increase in conductivity when compared to applying a sin waveform.

The ion conductivity (IC) of the electrically aligned samples shown in fig 4.3, 4.5, & 4.6 is found to have a higher hydroxyl ion (OH^-) conductivity when compared to a pristine membrane. Under the application of an AC electric field, the AEMs show an improvement in conductivity due to the alignment of the polymer towards the electric field and the formation of ion channels. Similarly, increasing the energy supplied ($\frac{dE}{dt}$) during casting increases ion conductivity by enhancing the alignment of the polymer. The ideal parameters for aligning the PCAP polymer are given below,

- Electric field strength - 32 V/cm
- Frequency - between 1000 Hz and 10000 Hz

4.2.2. Chrono potentiometry (CP)

In CP a fixed current (1.5 A) is applied at the working electrode and the resulting voltage change is measured with time. At constant current at the working electrode, the voltage is directly proportional to the resistance according to Ohm's law. An increasing voltage shown in fig 4.7 relates to an increase in membrane resistance.

#	Pristine	8E-100Hz	32E-100Hz	45E-100Hz	60E-100Hz	75E-100Hz
µm	65	49	52	50	66	44
V_{RMS}	0 V	0.3 V	1.1 V	1.6 V	2.1 V	2.6 V
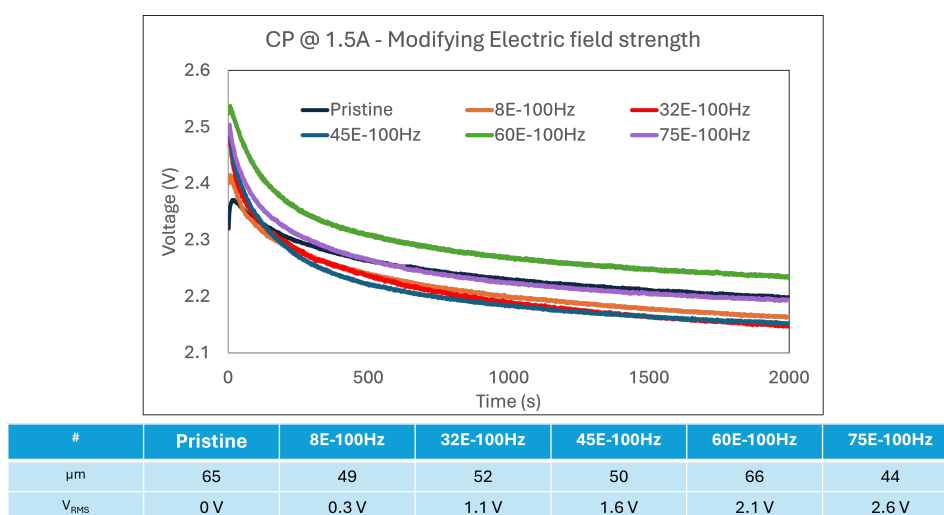
Figure 4.7: Chrono Potentiometry (1.5 A, RT) of membranes with different electric field strength

#	Pristine	8E-100Hz	8E-1000Hz	8E-10000Hz	8E-100000Hz
µm	65	49	25	59	35
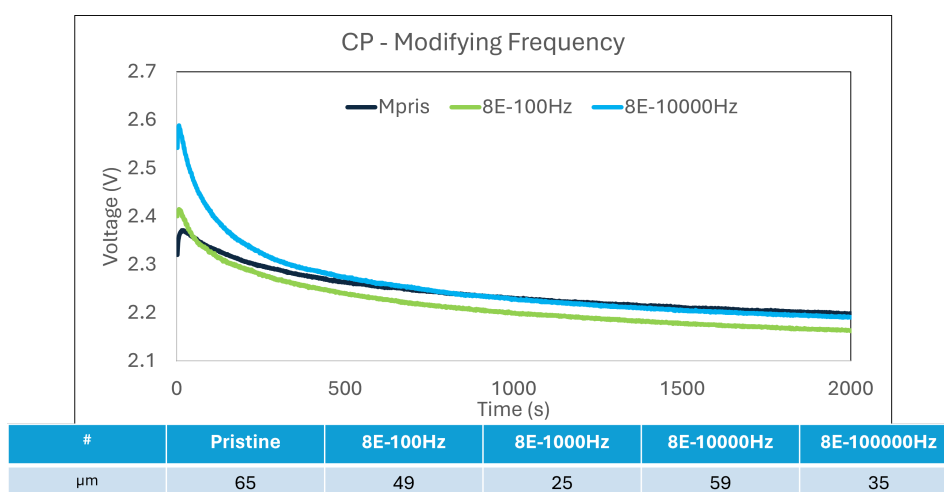
Figure 4.8: Chrono Potentiometry (1.5 A, RT) of membranes with different frequency

#	Pristine	8E-100Hz-Sin	8E-100Hz-Square
μm	65	49	66
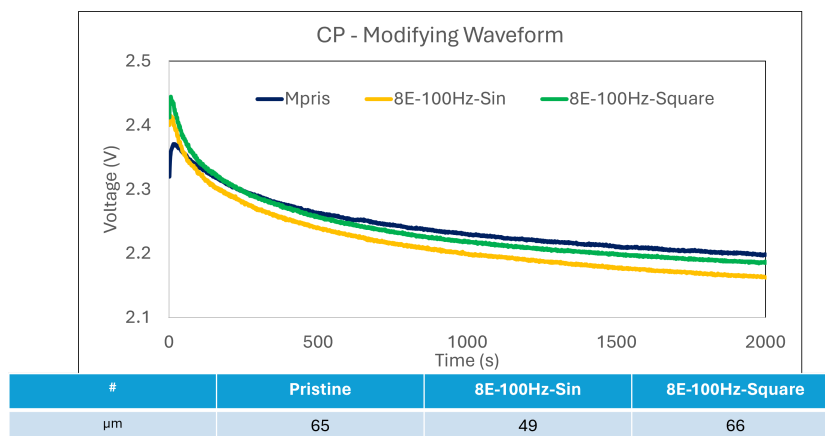
Figure 4.9: Chrono Potentiometry (1.5 A, RT) of membranes with different waveform

The CP curves in fig 4.9 show that the sin waveform shows better performance when compared to the square waveform. The results obtained cannot be confirmed easily as they have different thicknesses.

Chrono Potentiometry is an electrochemical technique that monitors the voltage with a constant current. The main function of using CP is to determine the short-term stability of the system. The CP curves in fig 4.7 show that increasing the electric field strength until 45 V/cm gives a higher performance when compared to a pristine membrane. The 60 V/cm membrane showed a higher voltage due to a higher thickness resulting in a high resistance. The CP curves shown in fig 4.8 indicate that increasing the frequency increases the performance of the membrane compared to the pristine membranes.

4.2.3. Cyclic Voltammetry (CV)

A CV is done on an electrolyser to determine the polarisation current of the membrane. This gives the maximum current at any applied voltage. The CV is run for five cycles to improve the statistics of the results. The results from the fourth cycle are plotted to obtain the polarisation curves.

#	Pristine	8E-100Hz	32E-100Hz	45E-100Hz	60E-100Hz	75E-100Hz
μm	65	49	52	50	66	44
V_{RMS}	0 V	0.3 V	1.1 V	1.6 V	2.1 V	2.6 V
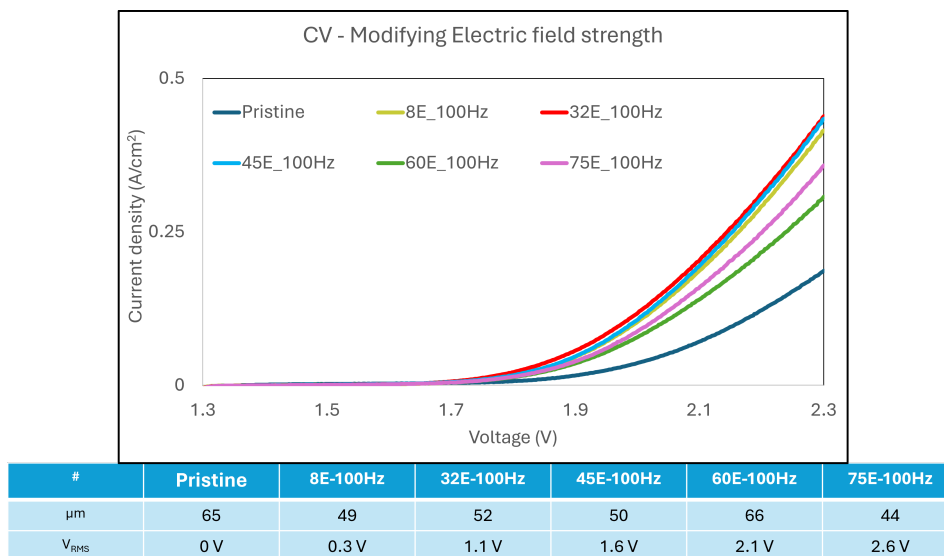
Figure 4.10: Polarization (CV) curves of membranes with different electric field strength

#	Pristine	8E-100Hz	8E-1000Hz	8E-10000Hz	8E-100000Hz
µm	65	49	25	59	35
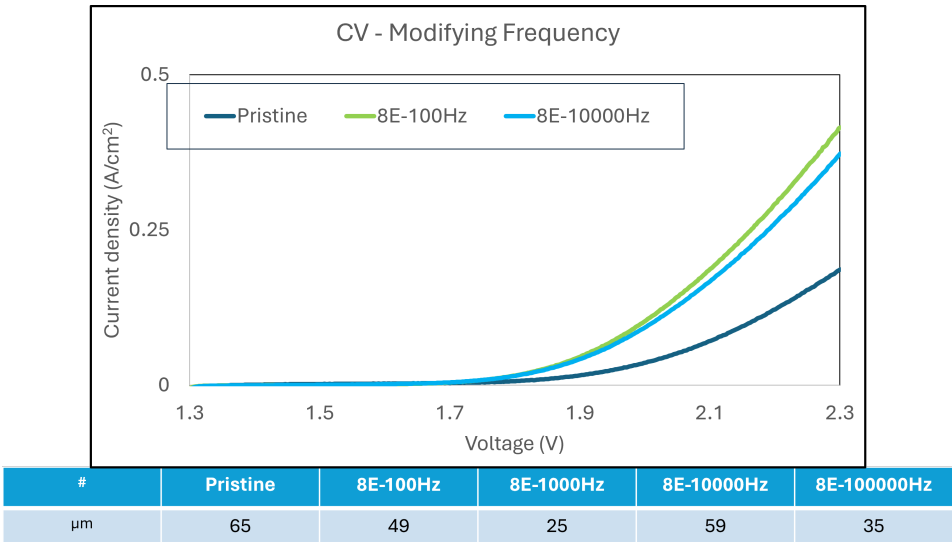
Figure 4.11: Polarization (CV) curves of membranes with different frequency

#	Pristine	8E-100Hz-Sin	8E-100Hz-Square
µm	65	49	66
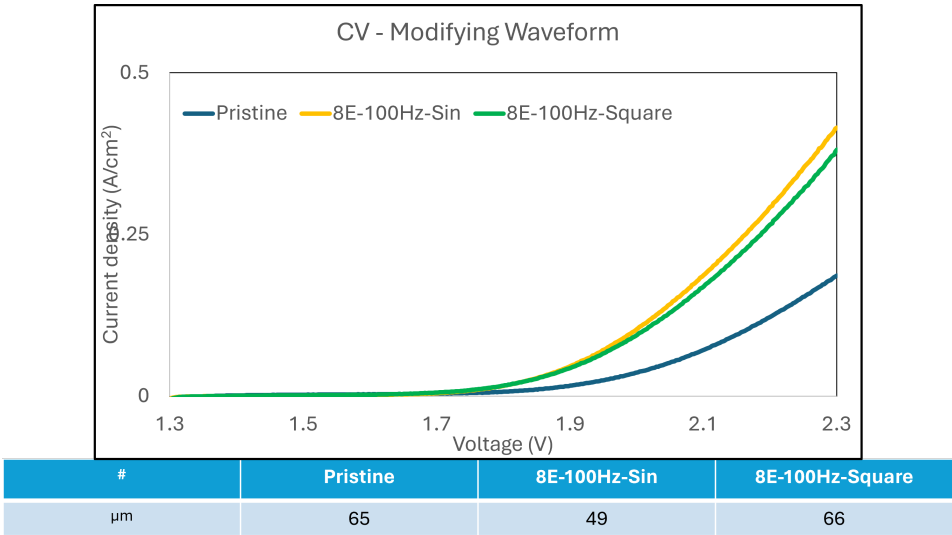
Figure 4.12: Polarization (CV) curves of membranes with different waveform

Cyclic Voltammetry (CV) is done to obtain the polarization current or the electrically aligned and pristine membranes. A higher current value at the same voltage shown in CV represents a higher performance of the membrane. We see an increase in current after 1.8 V as water electrolysis starts in the AEMWE system. The CV curves start diverging when the effects of ion transfer enter the picture. The CV curve of membranes modified with different electric field strengths (fig 4.10) show that the 8 V/cm, 32 V/cm, and 45 V/cm membranes show better performance than pristine membranes. Fig 4.11 indicate that 8E-10000Hz has a similar performance to 8E-100Hz although the thickness of the membranes differs by more than 10 microns. Fig 4.12 show that membranes produced with sine waveform have a higher performance than pristine.

4.2.4. Electrochemical Impedance Spectroscopy (EIS)

The EIS is done on the zero-gap electrolysers to track the changes in ohmic and charge transfer resistances. The EIS data of different membranes are hard to compare as the thickness of the samples is different.

#	Pristine	8E-100Hz	32E-100Hz	45E-100Hz	60E-100Hz	75E-100Hz
µm	65	49	52	50	66	44
V_{RMS}	0 V	0.3 V	1.1 V	1.6 V	2.1 V	2.6 V

Figure 4.13: Nyquist (EIS) plot of membranes with different electric field strength

The ohmic resistance is found to be 0.05 (Ω) and the charge transfer resistance is found to be very high for pristine membranes. The charge transfer resistance obtained from the diameter of the semi-circle decreases with an increase in conductivity as shown in fig 4.13. The thickness of the membrane has been found to have a slight influence on the charge transfer resistance. The EIS curves in fig 4.13 give an insight into the performance of the whole electrolysis system, where the improvement in AEMs could be observed. The EIS data on the electrical alignment is seen to be effective until an electric field strength of 32 V/cm. The electrolyser experiments have been done once and should be done multiple times to improve the reliability and the statistics of these results.

#	Pristine	8E-100Hz	8E-1000Hz	8E-10000Hz	8E-100000Hz
µm	65	49	25	59	35
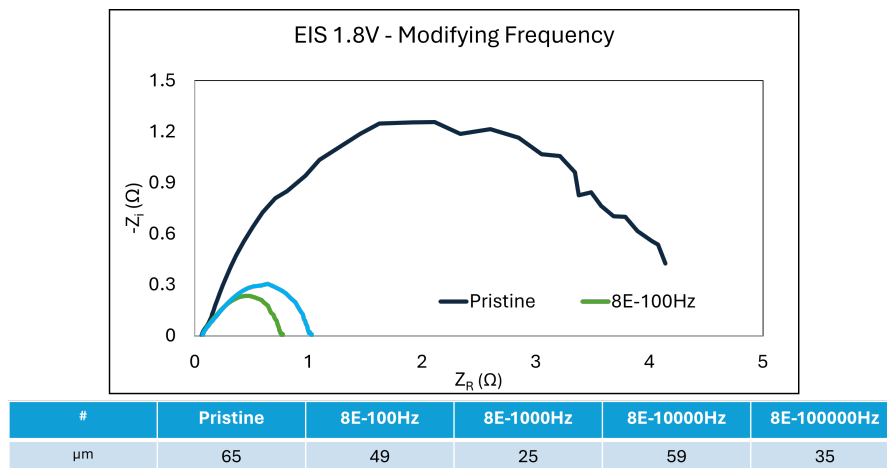
Figure 4.14: Nyquist (EIS) plot of membranes with different frequency

The ohmic resistance is found to be 0.05 (Ω) and the charge transfer resistance is found to be very high for pristine membranes. When the AEMs are electrically aligned with different frequencies, the charge transfer resistance of 8E-10000Hz is found to be higher than 8E-100Hz as the thicknesses are different for both AEMs.

Figure 4.15 chart title: EIS 1.8V - Modifying Waveform

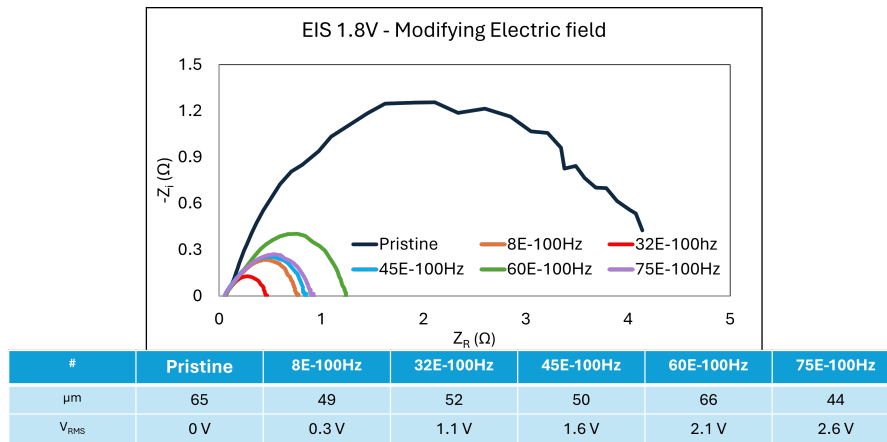| #	Pristine	8E-100Hz-Sin	8E-100Hz-Square
µm	65	49	66
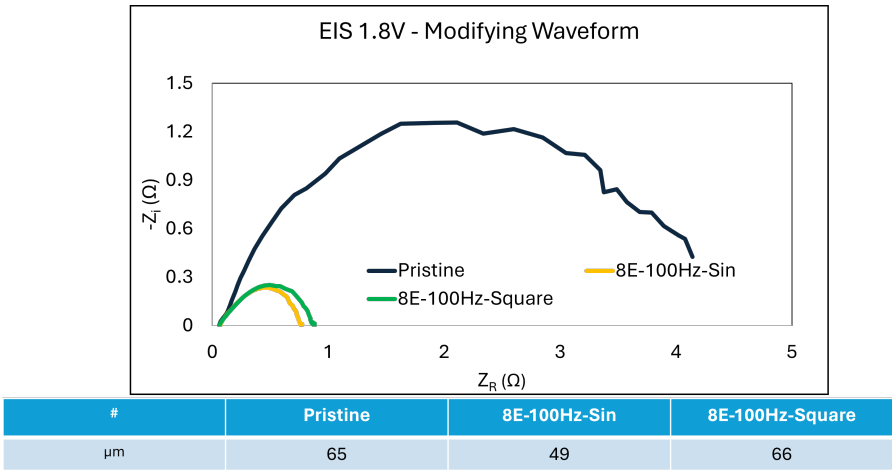
Figure 4.15: Nyquist (EIS) plot of membranes with different waveform

The ohmic resistance is found to be 0.05 (Ω) and the charge transfer resistance is found to be very high for pristine membranes. When the AEMs are electrically aligned with different waveforms, the charge transfer resistance of the membrane decreases rapidly to 0.95 (Ω).

> The EIS analysis is done to understand the changes in the ohmic resistance and the charge transfer resistance of the electrically aligned. Fig 4.13, 4.14 & 4.15 show that the electrically aligned polymer membranes have a very lower charge transfer resistance when compared to pristine membranes.

4.3. Mechanical characterisation

In this section, the mechanical characterisation techniques of a polymer are done to determine the physical properties such as swelling ratio, water uptake and tensile strength. A high mechanical strength in AEMs reduces swelling.

4.3.1. Swelling Ratio (SR): Thickness change

The membrane was soaked in 1M KOH for 48 hours and the dry and wet thickness were recorded to calculate the SR. Studies have shown that the swelling ratio of pristine PCAP is around 16$\pm$3 % [29].
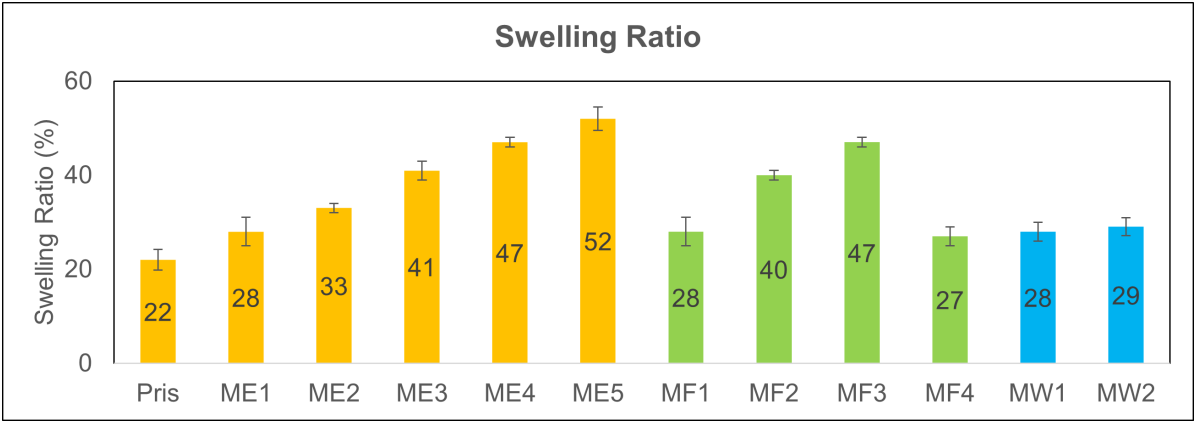
Figure 4.16: Swelling ratio (Thickness change) of different membranes cast using the setup

> The electrically aligned membranes show a higher swelling ratio than the literature as shown in fig 4.16. This could happen during alignment when the PCAP molecules rearrange towards the electric field in the through-plane direction. This causes a decrease in the interlinking of polymer molecules in the in-plane direction, thereby decreasing the mechanical strength between layers. This reduction in strength in the in-plane direction causes a higher swelling ratio for membranes and decreases the mechanical stability.

4.3.2. Water Uptake (WU): Mass change

The water uptake of pristine PCAP polymer membrane in 1M KOH is 45±5 % [29]. In this study, the weight of the polymer before and after activation is used to calculate the WU values. During the activation, the polymer matrix expands when water molecules enter the polymer matrix to facilitate hydroxyl ion transport.
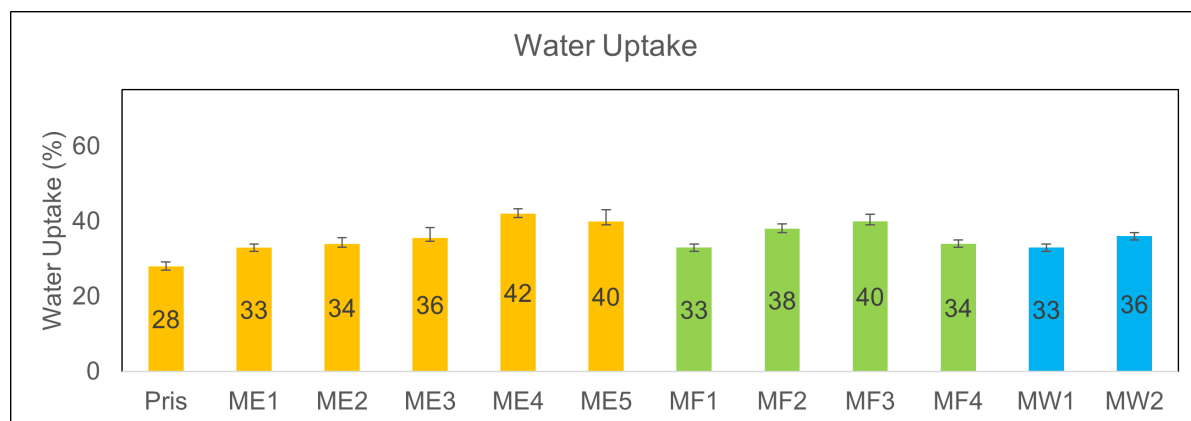
Figure 4.17: Water uptake (Mass change) values of different membranes obtained

> The Water Uptake (WU) of the polymer as shown in fig 4.17 increases with polymer alignment in the through-plane direction. This shows that the alignment of the polymer does affect the total water molecules present in the electrically aligned polymer membranes.

4.4. Chemical characterisation

In this section, the chemical stability of the polymer membranes are analysed using various characterisation techniques such as ion exchange capacity, FT-IR and H-NMR spectroscopy. Here, the chemical stability of the cationic head group (piperidinium) and the polymer groups are analysed under casting and electrolyser conditions.

4.4.1. Ion Exchange Capacity (IEC)

The IEC of the polymer membranes is measured using Mohr's titration method, where silver nitrate is used as titrant and potassium chromate is used as the indicator as shown in fig 3.9. The concentration of Chloride ions (Cl^-) is calculated to get the IEC (mmol/g) of the polymer sample. The IEC of each sample was measured three times to obtain the error bars.
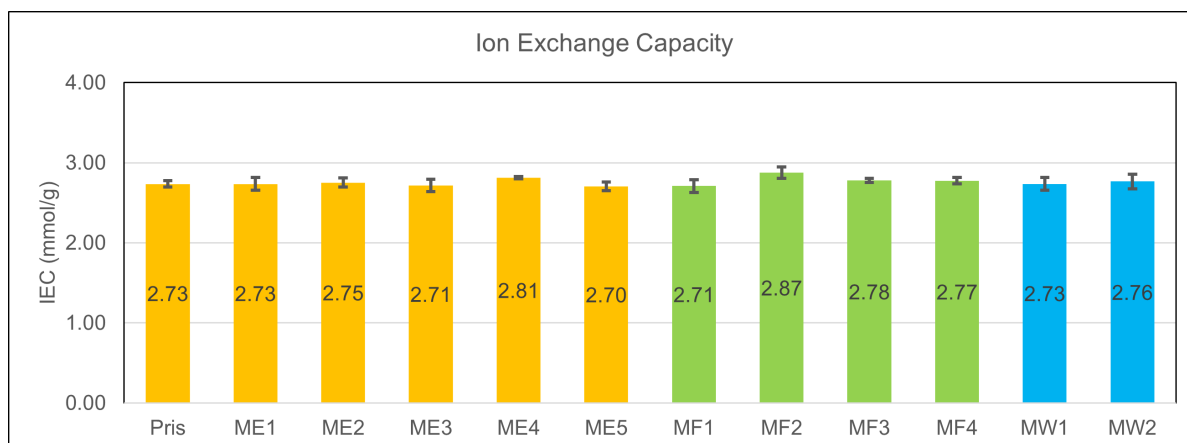
Figure 4.18: IEC of the different membranes cast using the setup

The ion Exchange Capacity (IEC) of the polymer shown in fig 4.18 is found to remain constant during the alignment of the polymer using the electric field. This concludes that the electrically aligned membranes do not have any changes in the number of cationic groups in the polymer structure.

4.4.2. Fourier Transform Infrared Spectroscopy (FT-IR)

The FT-IR spectra are used to identify the different types of bonds present in the sample and the degradation of the polymer during electric field application. The values from both graphs have no Y-axis as an arbitrary number (25) has been added to the Y-axis values of each sample to split them for analysis.
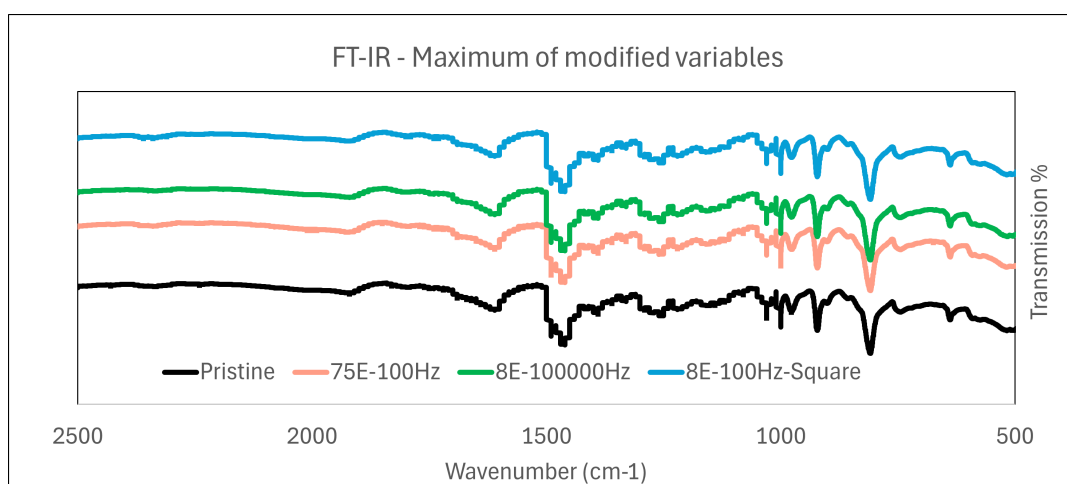
Figure 4.19: FTIR spectra of samples with the maximum parameters (Electric field, Frequency and Waveform)

The FT-IR analysis as shown in fig 4.19 shows no change while the maximum values of every parameter are analysed. This indicates that no additional degradation reaction happens when modifying the electric field strength (ME), frequency (MF), and waveform (MW) while casting the PCAP polymer.

4.4.3. Nuclear Magnetic Resonance (NMR)

NMR spectroscopy is used to identify the different types of protons present in the sample. This technique gives a clear signal towards the chemical degradation of the polymer. The H-NMR graph of the pristine membrane shown in fig 4.20 confirm that the polymer used during this thesis is PCAP.
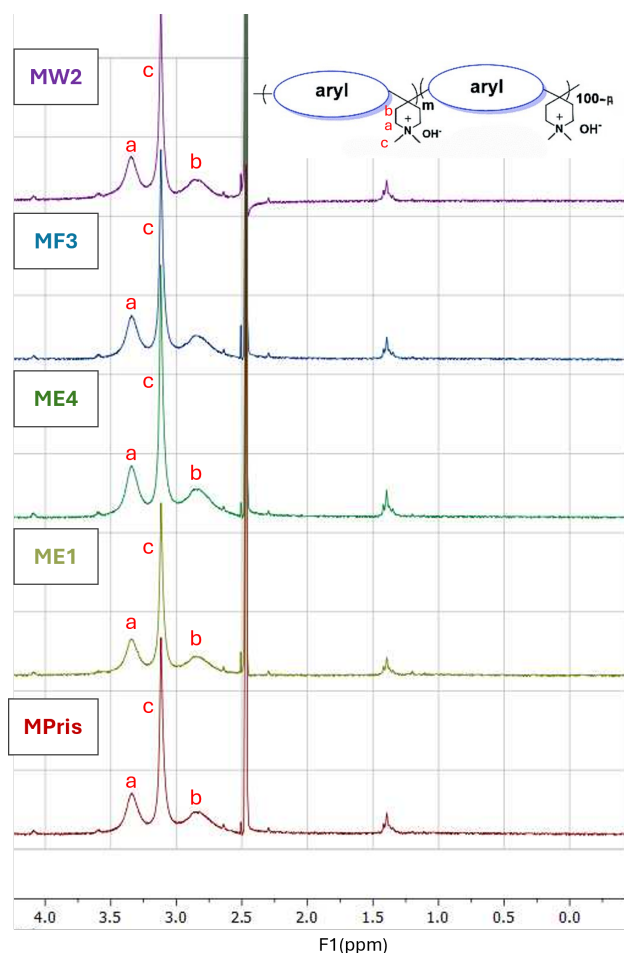
Figure 4.20: H-NMR of pristine and Electrically cast PCAP membranes

> Then H-NMR spectroscopy is done to monitor the chemical stability of the polymer while casting. The H-NMR spectra shown in fig 4.20 indicate no change in the chemical structure while modifying electric field strength (ME), frequency (MF), and waveform (MW). This confirms that additional reactions do not happen while synthesizing the PCAP membrane using an AC electric field.

4.4.4. Alkaline stability

The alkaline stability test is conducted to analyse the chemical stability of the polymer in AEMWE operation conditions. The polymer pieces are soaked in 1M, 5M and 10M KOH for 300 hours and the final polymer AEM is analysed using H-NMR. Apart from 1M KOH, higher concentrations of electrolytes are used to simulate the effect of an increase in electrolyte concentration such as during the water-splitting reaction at the cathode. The H-NMR of MF3 (10000 Hz) shows additional peaks due to improper removal of acetone from the H-NMR tube.
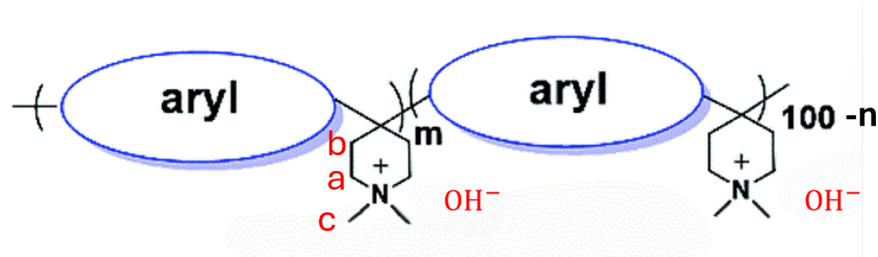
Figure 4.21: Protons associated with the Piperidinium group
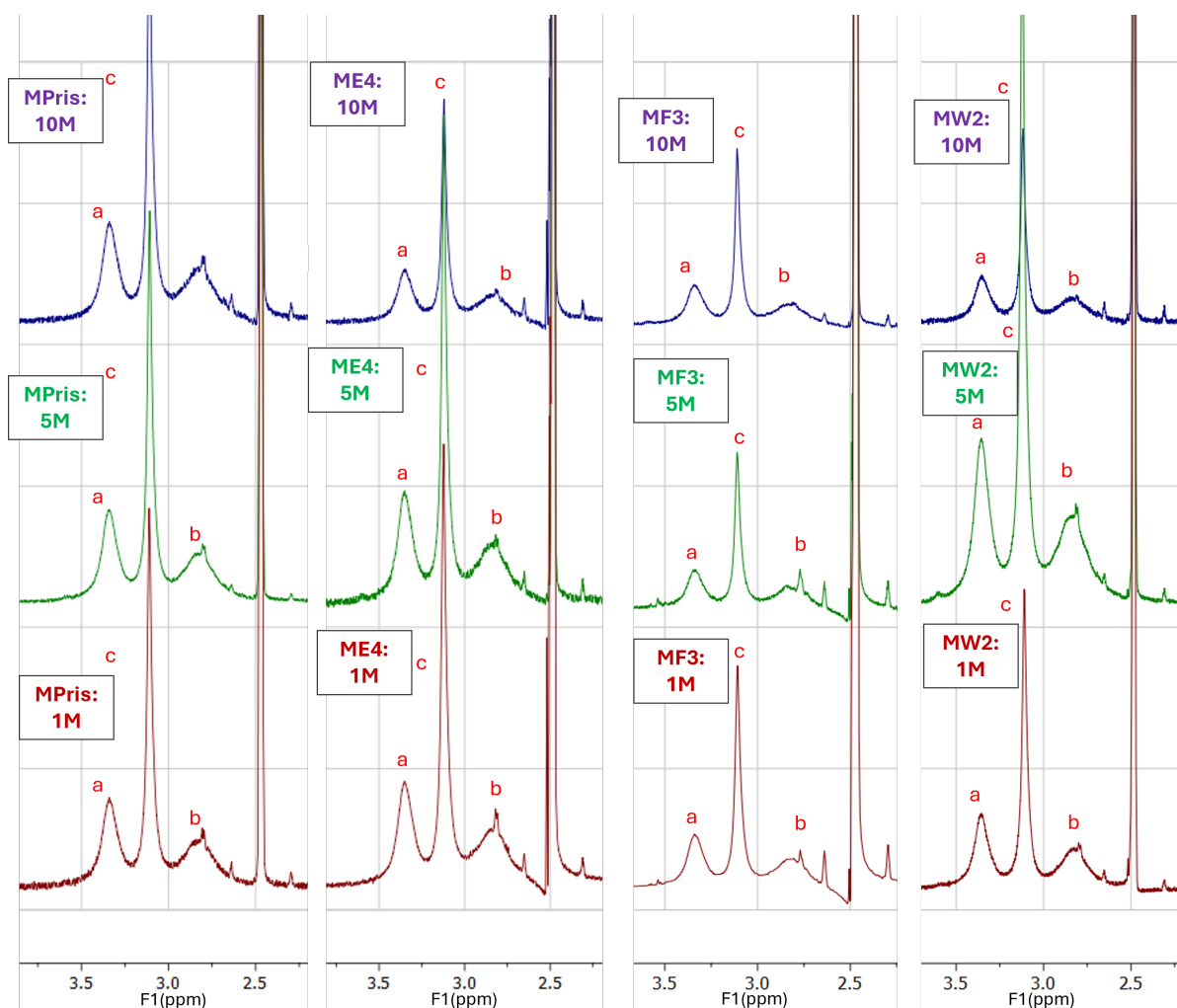
Figure 4.22: Alkaline stability of Pristine, ME5, MF3 and MW2 membranes in 1M, 5M and 10M KOH

The alkaline stability test is done to monitor the chemical stability of the polymer under AEM water electrolysis conditions. The H-NMR comparison of Pristine and electrically cast membranes shows no additional peaks. From this, the polymer degradation rate can be assumed to be the same. This shows that applying an electric field to align ion channels using electric field does not decrease the chemical stability of the PCAP membranes.

4.5. Thermal characterisation

The thermal characterisation techniques are done on the membrane to monitor the glass transition temperature (T_g) change in the electrically aligned membranes. This was done to verify that no changes happened in the membrane structure while drying the polymer AEM at 80° C. The degradation temperature of the polymer is also monitored to check for any changes in the degradation temperature.

4.5.1. DSC

Differential Scanning Calorimetry is used to measure the changes in physical properties of the polymer material with temperature against time. The DSC analysis is performed on the polymer sample with a heating rate of 2° C/min to identify the T_g.
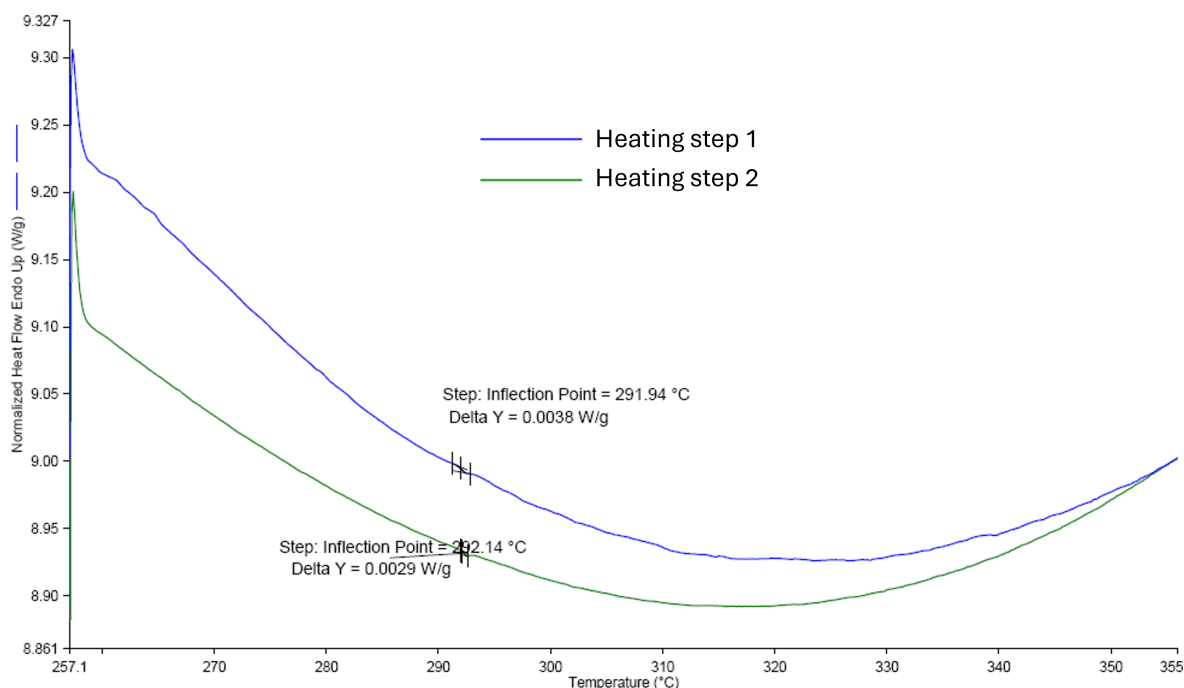
Figure 4.23: DSC heating curves of a pristine membrane

Table 4.1: Glass transition temperatures obtained from DSC

Sample	Glass transition temperature
MPris	292±0.5 °C
ME1	292±0.5 °C
ME5	292±0.5 °C
MF4	292±0.5 °C
MW2	292±0.5 °C
Polymer Solution	292±0.5 °C

DSC analysis is done to track the change in the glass transition temperature of the electrically aligned sample. Results from DSC of pristine (fig 4.23) and other electrically aligned membranes Table 4.1 shows that electrically aligning the polymer sample does not change the glass transition temperature.

4.5.2. Thermo Gravimetry Analysis (TGA)

TGA analysis was done on the polymer to measure the thermal stability regime of the PCAP membranes. The water present in the polymer matrix of the sample is found to be around $9\pm1\%$ by measuring the weight difference at $105°$ C. The weight loss of the sample and the rate of change in weight loss to temperature (DTG) is obtained. Studies have shown that the first weight loss between 210 to $350°$ C is found to be the decomposition of the cationic head group (ammonium groups), and the weight loss over 350 has been attributed to the decomposition of the two co-polymer backbones [29].
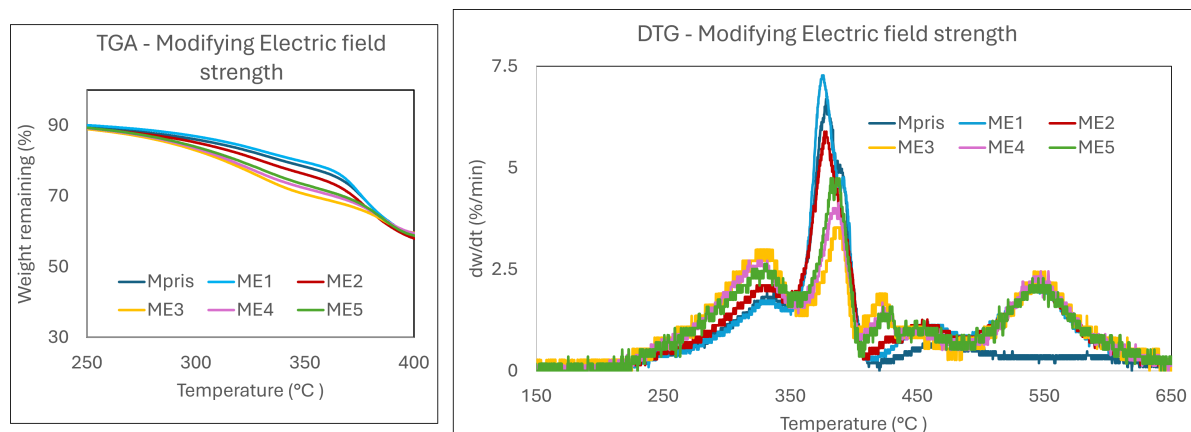
Figure 4.24: TGA and DTG of different electric field strength applied

The TGA and DTG plots show that the membranes synthesized above an electric field of 32 V/cm (V_{DC}=1.12V) degrade faster than pristine membranes. The pristine membrane and membranes synthesised with lower electric field strength show a sharp DTG peak at 390 °C. The initial ammonium degradation peaks become bigger when the polymer is aligned using a higher electric field strength.
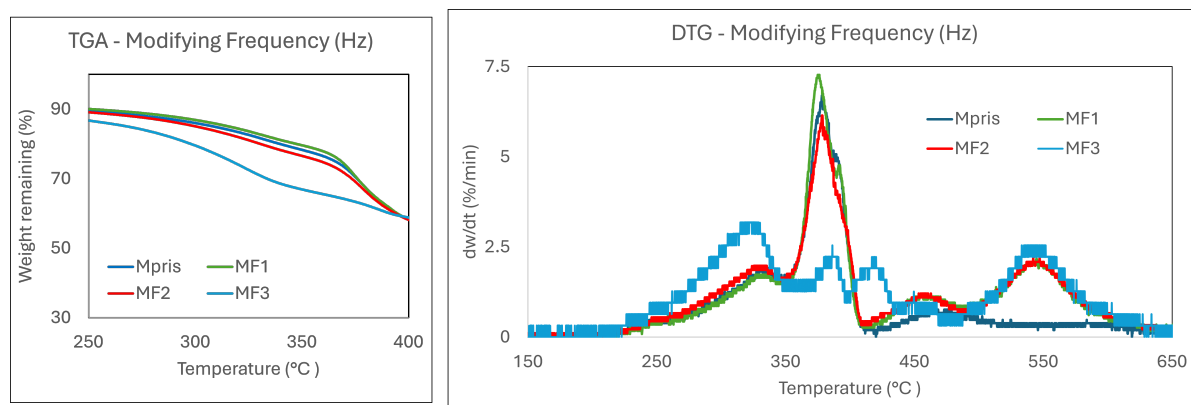
Figure 4.25: TGA and DTG curves of different frequency applied

The TGA plot (fig 4.25) shows that at any given temperature, the membrane synthesized using higher frequency degrades faster. The DTG plot of modifying frequency clearly show that the membranes synthesized above a frequency of 1000 Hz degrade faster than pristine membrane.
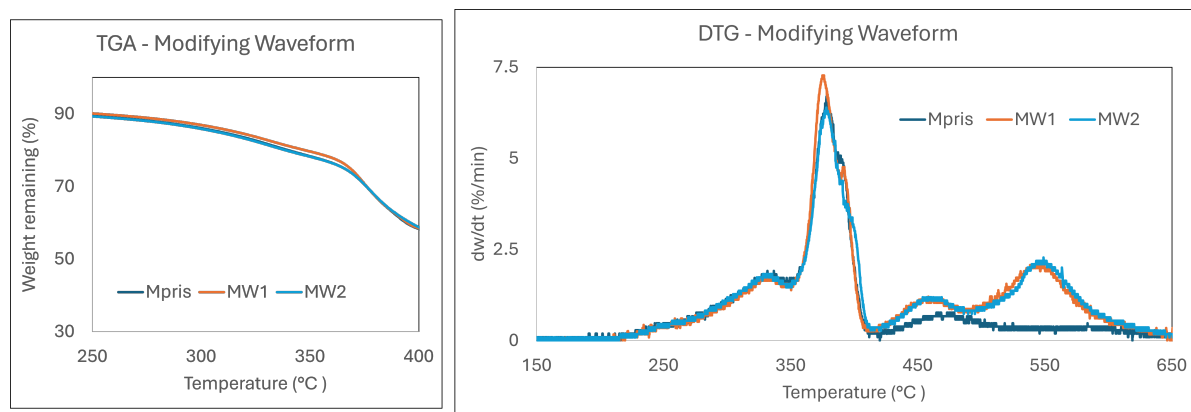
Figure 4.26: TGA and DTG curves of different waveforms applied

The TGA and DTG plot of modifying waveform shows that changing the waveform does not show any difference while the ammonium groups degrade, but the degradation rate of backbones in electrically aligned polymers appear faster.

> The TGA analysis is done to determine the thermal stability of the temperature. Plotting the derivative thermogravimetry (DTG) plot shows that applying a higher electric field strength and frequency above 32 V/cm and 1000 Hz respectively could result in a faster degradation of the ammonium groups. This could be due to the relaxation of the ammonium groups as the PCAP polymer aligns towards the through-plane direction during electrical alignment. This concludes that the thermal stability regime of the electrically aligned membranes change when compared to pristine membranes.

4.6. Morphology analysis

Once the mechanical, chemical and thermal stability of the membrane is analysed, the formation of structures or the change in the morphology of the membrane is analysed. This is done to track the formation of ion-conducting channels with electric field.

4.6.1. Atomic Force Microscopy (AFM)

The surface morphology of the AEMs synthesized using an electric field is observed using an AFM. The sample to produce a surface with aligned polymer is created using the in-plane alignment setup as shown in fig 6.3.
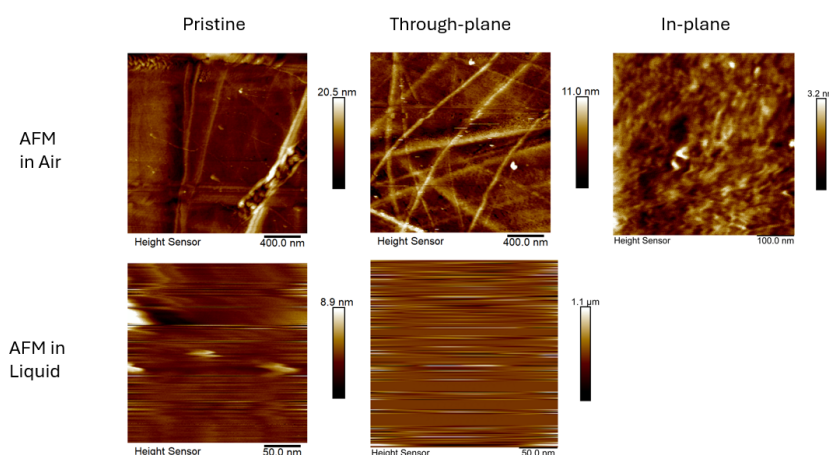
Figure 4.27: Results of AFM analysis of the membrane aligned in through-plane and in-plane directions.

The AFM analysis is done to understand the surface morphology of the polymer sample. A proper conclusion could not be obtained using the AFM analysis. Some ideas to improve the results are given below,

- Creating a larger aligned sample: The gap length must be increased to 2 cm and a 50 V DC regulator must be placed to apply the electric field.
- The polymers could be synthesized on a silica wafer with a smooth surface. This would not add additional morphology to the polymer surface.

4.7. System Integration and socio-economic aspects

As shown in section 1.4, The rapid growth of renewables has led to an increasing demand for hydrogen. Production of hydrogen could be done safely and affordably by using AEM water electrolysis technology. In this thesis, The ion conductivity of the polymer AEM is increased by applying an AC electric field.

The results show an increase in ion conductivity with the potential to increase further. This work done on electrically aligning the polymer could also be integrated into other industrial systems such as flow batteries, fuel cells, water electrolysis, water purification and electrochemical industries that use polymer membranes to improve overall performance.

This work moves the focus from PEM electrolysers to AEM electrolysers, as PEM uses harmful and carcinogenic poly-fluoro substances in int operation. An increase in the development of AEMWE technology could result in an improvement in the lifestyle and well-being of an average citizen affected by the "forever-chemicals". This could also bring investors from large companies and government support on board in adapting the hydrogen economy as one of the solutions.

5
Conclusion

This research focused on improving the performance of an Anion-exchange membrane (AEM) electrolyser. The main disadvantage of the technology lies in the AEM and its low ion conductivity. We tried to improve this by...

"Applying an alternating current (AC) electric field to improve the ion conductivity of an anion-exchange membrane (AEM) while retaining stability".

Here, among the different parameters that could be optimised, three parameters were selected: voltage, frequency and waveform of the AC electric field. The polymer solution was made using DMSO and the membranes were cast using a doctor blade setup. The results from the electrically aligned membranes show a maximum of 300% increase in the ion conductivity of the membrane. This result is also supported by an increase in the electrolyser performance. The ideal AC parameters to align the polymers are a 45 V/cm electric field voltage, a 1000 Hz frequency and a square waveform.

Some key takeaways from the characterisation tests are given here. The electrical alignment of the membrane reduces the mechanical stability due to a decrease in the tensile strength and alignment in the through-plane direction. The chemical stability of the electrically aligned and pristine membranes was found to be the same. Finally, In the thermal stability measurements, the degradation regime of the polymer changed and the electrically aligned polymer degraded faster than the pristine membranes. A reason given here was the reduction in the hindrance for the cationic head groups due to polymer alignment.

The research done in this thesis confirms that the alignment of the polymer using an electric field improves the ion conductivity of the polymer membrane. This solves one of the main problems of AEM water electrolysis technology by improving the conductivity of the AEM, however further research is needed to understand the slight reduction in the stability of the polymer.

6

Outlook

In this chapter, Some interesting new ideas proposed are given in section 6.1. Section 6.2 explains the concepts and things that need some potential improvements and further work to be done.

6.1. Interesting new ideas and directions

Some interesting ideas and research directions proposed during this thesis are given below with a small explanation.

- Applying different AC waveforms: Work must be done on using fully rectified, exponential increasing, and square waves.
- Polymer breakdown: Polymers have been found to break down at higher voltages and higher frequencies. Increasing the frequency has been found to decrease the breakdown strength [84]. The breakdown of thin film polymers is found on the sample electrode interface [85].
- Analysing DMSO: The polymer PCAP at high voltages shows a browning at the surface and the phenomenon must be understood. Pure DMSO must be placed in a glove box and an absolute voltage must be applied to it to check the breakdown strength of DMSO with and without water.
- Capturing the reorientation: The reorientation of the PCAP molecules could be analysed using FE-TEM. Samples must be synthesised using a spin coating setup and a thickness of 20 µm [22].
- Finding the alignment time: The alignment time of the polymer must be analysed to determine the speed of a continuous casting machine that applies an electric field.
- High-temperature setup: A high-temperature setup must be developed with proper reference electrodes to analyse the industrial performance of AEMWE using PCAP membranes.
- Creating proper UTM samples: The mechanical stability of the membranes must be done using samples at uniform thickness cut using an automatic cutter. measurements.
- Molecular simulations: The dipole strength of the polymer and iodide ion could be found to analyse the forces on the polymer chain during AC alignment.

Molecular simulation to get the dipole movement and orientation

6.2. Things with potential improvements

6.2.1. In-plane alignment

In this setup, the electric field is used to align the polymer in the in-plane direction. This alignment in the in-plane direction is mainly done to understand the polymer alignment with electric field. The alignment of the polymer could be monitored by measuring the current during alignment at a constant electric field strength as shown in fig 6.1. The following equations gives the relation between current and the degree of alignment.

$$U_{rot} = nEqd(1 - cos\Theta)$$
$$U_{rot} = I^2RT$$

These two equations are be used to derive the final equation.

$$I = \sqrt{\frac{nEqd(1-cos\theta)}{R_{mem}T}}$$
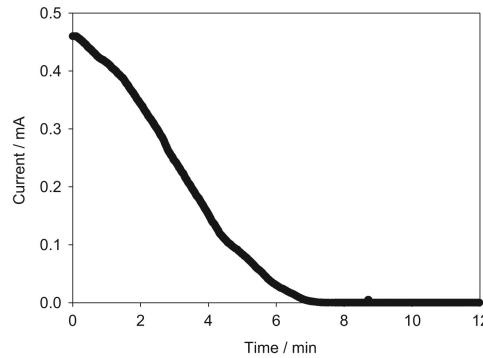
Figure 6.1: Current profile observed during the in-plane alignment [25]

Here the current (I) is obtained from rotational energy (U$_{rot}$), number of dipoles (n), voltage (E), charge (q), the dipoles distance (d), the dipole angle (θ), membrane resistance (R$_{mem}$), and time (t). Plotting a curves between current (I) and time (t) shows an operando (in-situ) alignment of the dipoles to the electric field [72].

In-plane alignment using adjustable setup
The setup shown in fig 6.2 is used to align the polymer in the in-plane direction. Here, the polymer is poured between two copper blocks fixed with a gap of 350 microns. An electric field is applied between the copper blocks after the polymer is poured into the gap. This setup is run for 10 minutes to allow a complete alignment of the polymer. The current values are recorded to visualise the operando alignment of the polymer [25].
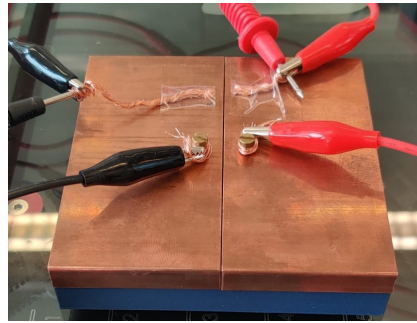
Figure 6.2: Schematics of an In-plane electrical alignment setup with a movable base

Simple In-plane alignment setup
In the setup shown in fig 6.3, two copper wires are placed at a gap of 2.5mm on a glass plate. An electric field is applied between the two wires after some polymer is poured between the platinum wires. The current readings were measured to determine the operando alignment of the polymer as shown in fig 6.3 [25].
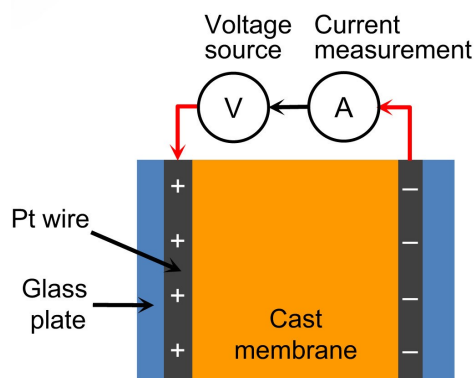
Figure 6.3: Schematics of an In-plane electrical alignment setup [25]

The membranes synthesised using this setup need to be 2 cm wide to get a good result in AFM. A voltage supply of 50 volts, connected with an ammeter in series is needed to obtain the current (I) measurements.

6.2.2. Universal Testing Machine (UTM)

A universal testing machine is used to measure the mechanical strength of the membrane, such as tensile strength and elongation of break. The sample is placed between the grips in the load cell as shown in fig 6.5. After loading the sample, the UTM device starts applying an increasing pulling force (200 mN/min) on the sample to get the tensile strength results.

Figure 6.4: Clamp holding the polymer samples (left), Dumbbell-shaped samples (middle), and a proper fracture at the middle of the polymer (right)

The samples for UTM analysis are prepared by cutting an activated PCAP polymer with 10mm * 30mm dimensions. The samples are then cut to a dumbbell shaped strips (fig 6.5). The prepared strips are then tested using the UTM device. For this thesis, the Instron 5kN Universal Testing Machine with a 1kN load cell is used to measure the tensile strength and elongation at break [29].

The polymer samples (10mm * 30mm) are placed between the clamps of a 1kN UTM machine (fig 6.4) to obtain the tensile strength (TS) and elongation at break measurements.

The tensile strength measurement from UTM shows that activated pristine membranes have a maximum tensile strength of 26 MPa. In contrast, the activated electrically aligned membranes show a

maximum tensile strength less than the pristine membrane as shown in fig 6.5. This could be attributed to the decrease in cross-linking as the polymer gets aligned in the through-plane direction. Some insights learned from the using the 1kN UTM are,

- The different polymer samples must have a uniform thickness to make a reasonable comparison.
- The polymer must be cut into a perfect dumbbell shape to prevent inducing additional stresses in the polymer. A metal punch with a fixed shape would produce uniform samples for analysis.
- The force experienced by the sample ranges between 0 and 15 N. Using the UTM setup in the range of 1% of its capacity increases the error percentage in the values obtained.
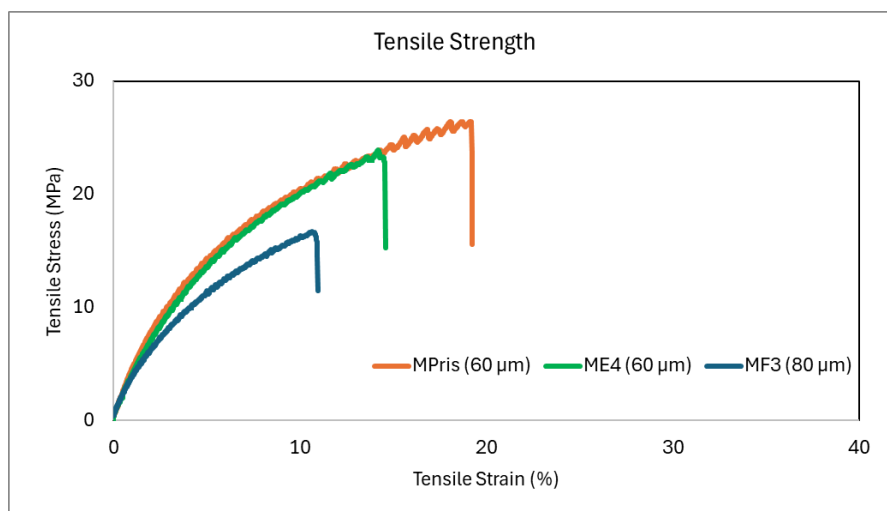

Figure 6.5: Stress Strain curve obtained for different Membranes

The tensile strength measured using UTM shows that the electrically aligned membrane shows lower mechanical strength (TS = 16-23 MPa) when compared to the pristine membrane (TS = 26 MPa) in the activated state. A large error margin in the results leads to an unclear conclusion due to improper sample preparation. Improper cutting adds additional stresses on the polymer that could add errors to the UTM. A uniform sample cutter with ASTM standards must be used for comparable results.

6.2.3. Dynamic Mechanical Analysis (DMA)

The DMA is a device used to characterise polymers based on mechanical strength. Here, an oscillatory force is applied to the material and its response is measured to calculate different parameters such as viscosity and glass transition temperatures and tensile strength. In addition to obtaining the complex modulus, DMA also provides information of the samples at high temperatures [86]. The DMA is done to obtain the glass-transition temperature (T_g) of the polymer, Storage modulus and the loss modulus of the AEMs

Samples with dimensions 30mm * 10mm are cut and placed between the clamps to run the DMA system. DMA testing is performed with a 1Hz single-frequency strain mode, a preload force of 0.01 N and a force track of 125%. The maximum temperature was set at 400° with a heating rate of 10° C/min [29].

the DMA is a technique used to measure the physical properties of the polymer sample by applying an oscillator force to measure the response. This could be used to calculate the glass transition temperature (T_g) and the storage modulus with increasing temperature. The PCAP co-polymer with two different backbone groups should show two T_gs as they have different thermomechanical stability regimes.
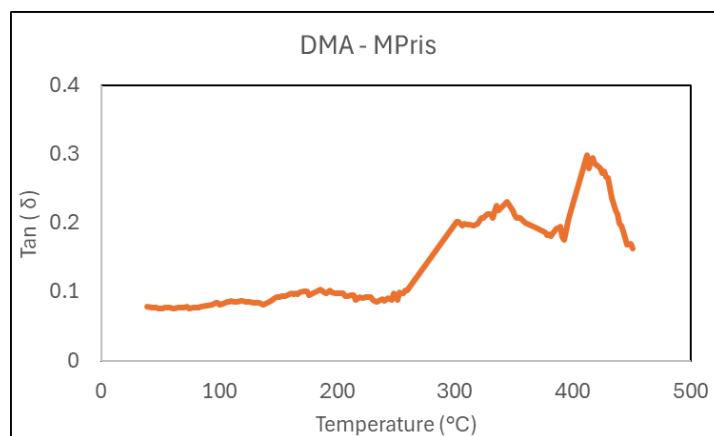
Figure 6.6: DMA data for pristine membrane (MPris)

The pristine membrane analysed using DMA showed that PCAP polymers have two glass transition temperatures as it is a co-polymer. The reliability of this data must be improved with further changes to the DMA testing parameters.

6.2.4. Wide-angle X-ray scattering (WAXS)

The WAXS is a technique used in determining the crystalline nature of the polymer sample using Bragg peaks. The WAXS analysis was done at ESRF, France. In this experiment, electrically aligned samples, in the I$^-$ form is analysed. WAXS gives detailed information of the nano-scale structures available in the aligned polymers.
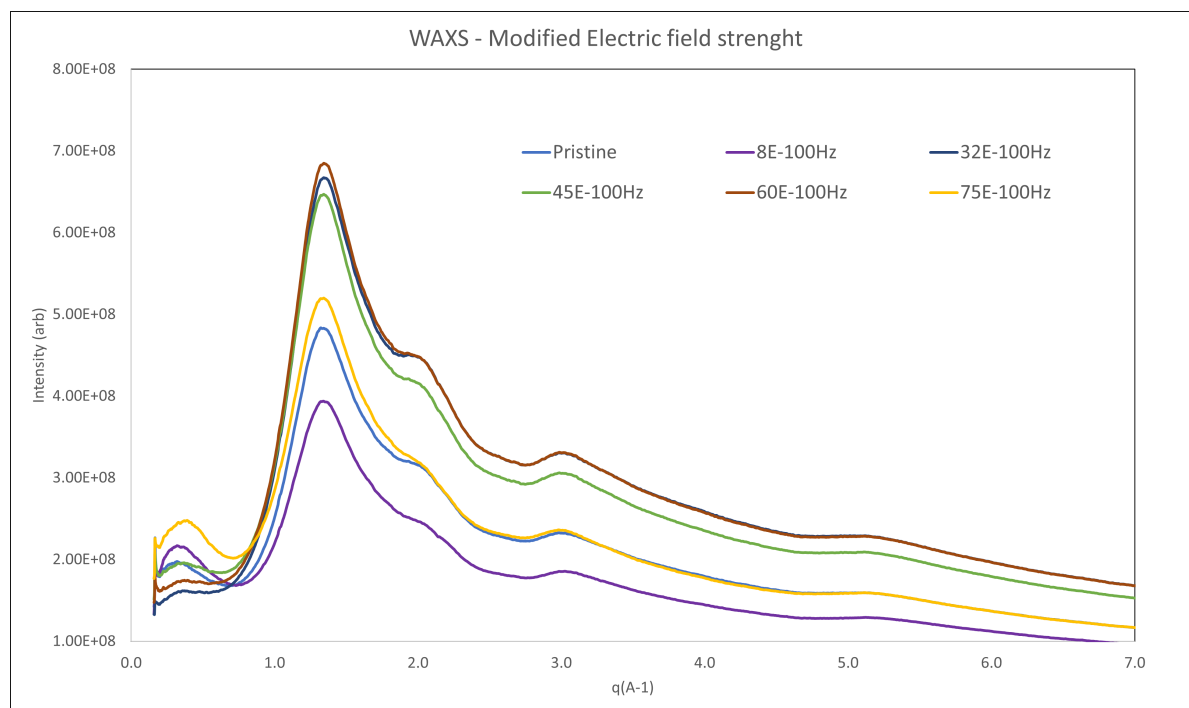
Figure 6.7: WAXS of membranes with modified electric field strength

The fig 6.7 shows that polymer membranes modified with higher electric field has a higher peak intensity and clear shoulder when compared to pristine membranes. Finally, the membrane at 75 V/cm shows a peak comparable to pristine without the second shoulder.
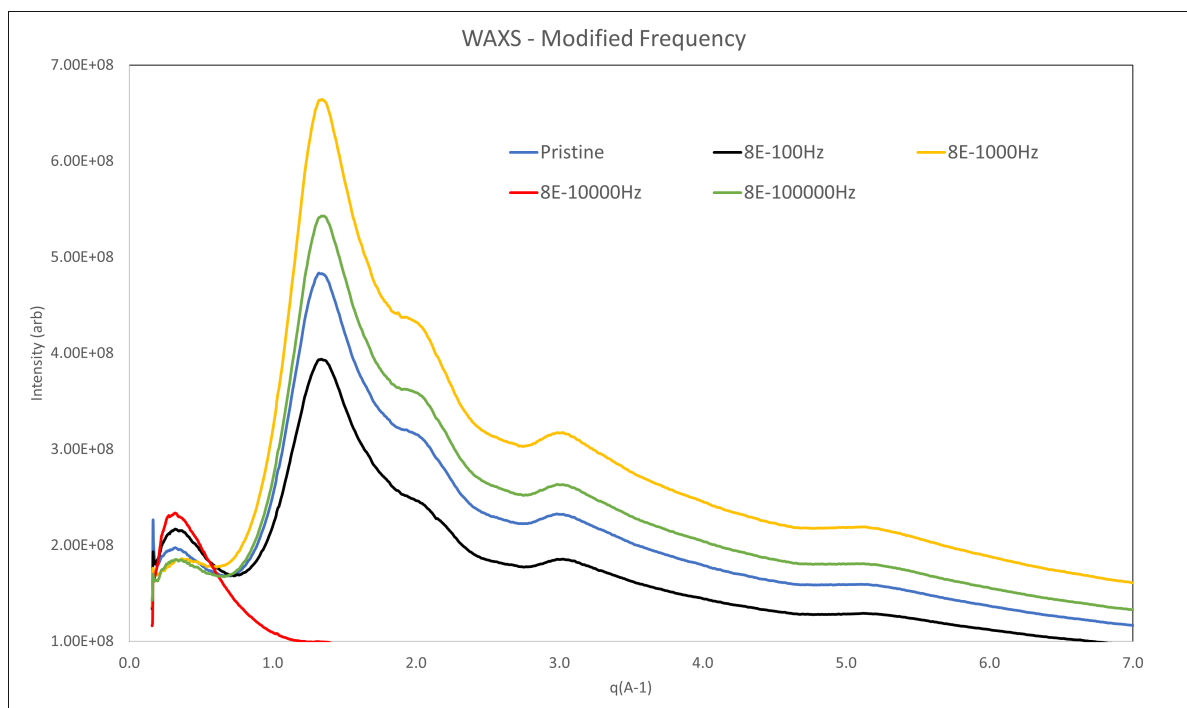
Figure 6.8: WAXS of membranes with modified electric field strength

Fig 6.8 shows that the membranes with 1000Hz show a higher peak when compared to Pristine. The sharp increase in the first peak intensity and sharp shoulders indicate that the polymer PCAP membrane has developed some crystallinity during alignment. This could be proof of the electrical alignment of the PCAP polymers.

> The electrically aligned and pristine membranes were tested using WAXS for crystallinity formation. From fig 6.7 we were able to observe that the crystallinity improved until 60 V/cm and an absolute V_{RMS} of 2.1V. When modifying the frequency the membrane showed a higher order of crystallinity for the 1000Hz sample. Unfortunately, the 10000Hz with the highest conductivity couldn't be analysed due to problems in the sample. Although the increase in peak intensity could be due to a higher degree of crystallinity, further analysis has to be conducted to understand the peaks and the WAXS data.

Bibliography

[1] H. Ritchie, P. Rosado, and M. Roser, "Co☐ and greenhouse gas emissions," *Our World in Data*, 2023. https://ourworldindata.org/co2-and-greenhouse-gas-emissions.

[2] NASA, "Carbon dioxide: Vital signs of the planet," 2024.

[3] IPCC, "Climate change 2013: The physical science basis," ipcc fifth assessment report (ar5), Intergovernmental Panel on Climate Change, 2013.

[4] Delphi, "Global energy potential. comparing renewable and non-renewable energy sources by their potential.," 2014.

[5] IRENA, "Renewable energy capacity statistics 2023, by international renewable energy agency," 2023.

[6] M. Tawalbeh, S. Z. Murtaza, A. Al-Othman, A. H. Alami, K. Singh, and A. G. Olabi, "Ammonia: A versatile candidate for the use in energy storage systems," *Renewable Energy*, vol. 194, pp. 955–977, 2022.

[7] F. Ustolin, A. Campari, and R. Taccani, "An extensive review of liquid hydrogen in transportation with focus on the maritime sector," *Journal of Marine Science and Engineering*, vol. 10, no. 9, p. 1222, 2022.

[8] I. Abbasi, "How safe is hydrogen in shipping?," 2022.

[9] A. Riaz, M. A. Qyyum, A. Hussain, and M. Lee, "Significance of ortho-para hydrogen conversion in the performance of hydrogen liquefaction process," *International Journal of Hydrogen Energy*, vol. 48, no. 68, pp. 26568–26582, 2023.

[10] M. Jaradat, O. Alsotary, A. Juaidi, A. Albatayneh, A. Alzoubi, and S. Gorjian, "Potential of producing green hydrogen in jordan," *Energies*, vol. 15, no. 23, p. 9039, 2022.

[11] Q. Xu, L. Zhang, J. Zhang, J. Wang, Y. Hu, H. Jiang, and C. Li, "Anion exchange membrane water electrolyzer: electrode design, lab-scaled testing system and performance evaluation," *EnergyChem*, vol. 4, no. 5, p. 100087, 2022.

[12] C. Li and J.-B. Baek, "The promise of hydrogen production from alkaline anion exchange membrane electrolyzers," *Nano Energy*, vol. 87, p. 106162, 2021.

[13] N. Chen, S. Y. Paek, J. Y. Lee, J. H. Park, S. Y. Lee, and Y. M. Lee, "High-performance anion exchange membrane water electrolyzers with a current density of 7.68 a cm- 2 and a durability of 1000 hours," *Energy & environmental science*, vol. 14, no. 12, pp. 6338–6348, 2021.

[14] C. Santoro, A. Lavacchi, P. Mustarelli, V. Di Noto, L. Elbaz, D. R. Dekel, and F. Jaouen, "What is next in anion-exchange membrane water electrolyzers? bottlenecks, benefits, and future," *ChemSusChem*, vol. 15, no. 8, p. e202200027, 2022.

[15] C. Chen, Y.-L. S. Tse, G. E. Lindberg, C. Knight, and G. A. Voth, "Hydroxide solvation and transport in anion exchange membranes," *Journal of the American Chemical Society*, vol. 138, no. 3, pp. 991–1000, 2016.

[16] I. Vincent and D. Bessarabov, "Low cost hydrogen production by anion exchange membrane electrolysis: A review," *Renewable and Sustainable Energy Reviews*, vol. 81, pp. 1690–1704, 2018.

[17] S. A. Lee, J. Kim, K. C. Kwon, S. H. Park, and H. W. Jang, "Anion exchange membrane water electrolysis for sustainable large-scale hydrogen production," *Carbon Neutralization*, vol. 1, no. 1, pp. 26–48, 2022.

[18] M. Hellström, V. Quaranta, and J. Behler, "One-dimensional vs. two-dimensional proton transport processes at solid–liquid zinc-oxide–water interfaces," *Chemical Science*, vol. 10, no. 4, pp. 1232–1243, 2019.

[19] H. H. Wang, C. Hu, J. H. Park, H. M. Kim, N. Y. Kang, J. Y. Bae, W. H. Lee, N. Chen, and Y. M. Lee, "Reinforced poly (fluorenyl-co-terphenyl piperidinium) anion exchange membranes for fuel cells," *Journal of Membrane Science*, vol. 644, p. 120160, 2022.

[20] N. Chen, J. H. Park, C. Hu, H. H. Wang, H. M. Kim, N. Y. Kang, and Y. M. Lee, "Di-piperidinium-crosslinked poly (fluorenyl-co-terphenyl piperidinium) s for high-performance alkaline exchange membrane fuel cells," *Journal of Materials Chemistry A*, vol. 10, no. 7, pp. 3678–3687, 2022.

[21] D. Han, J. Sun, J. Ge, H. Guo, J. Zhang, C. Wang, P. Hu, and Y. Liu, "Magnetically aligned composite membranes based on sulfonated poly (ether ether ketone) and phosphotungstic acid-loaded magnetic nanoparticles for fuel cell," *International Journal of Hydrogen Energy*, vol. 57, pp. 301–314, 2024.

[22] J.-H. Kim, I. S. Chang, and S.-H. Moon, "High performance acid–base junction flow batteries using an asymmetric bipolar membrane with an ion-channel aligned anion exchange layer," *Journal of Materials Chemistry A*, vol. 9, no. 12, pp. 7955–7966, 2021.

[23] N. Chen, S. P. Kim, C. Hu, H. H. Wang, J. H. Park, H. M. Kim, and Y. M. Lee, "High-performance poly (fluorenyl aryl piperidinium)-based anion exchange membrane fuel cells with realistic hydrogen supply," *Journal of Power Sources*, vol. 512, p. 230474, 2021.

[24] S. Ryu, J.-H. Kim, J.-Y. Lee, and S.-H. Moon, "Investigation of the effects of electric fields on the nanostructure of nafion and its proton conductivity," *Journal of Materials Chemistry A*, vol. 6, no. 42, pp. 20836–20843, 2018.

[25] J.-Y. Lee, J.-H. Lee, S. Ryu, S.-H. Yun, and S.-H. Moon, "Electrically aligned ion channels in cation exchange membranes and their polarized conductivity," *Journal of membrane science*, vol. 478, pp. 19–24, 2015.

[26] Labster, "Proton nmr spectroscopy," 2024.

[27] J. J. Ojeda and M. Dittrich, "Fourier transform infrared spectroscopy for molecular analysis of microbial cells," *Microbial Systems Biology: Methods and Protocols*, pp. 187–211, 2012.

[28] C. Leyva-Porras, P. Cruz-Alcantar, V. Espinosa-Solís, E. Martínez-Guerra, C. I. Piñón-Balderrama, I. Compean Martínez, and M. Z. Saavedra-Leos, "Application of differential scanning calorimetry (dsc) and modulated differential scanning calorimetry (mdsc) in food and drug industries," *Polymers*, vol. 12, no. 1, p. 5, 2019.

[29] N. Chen, H. H. Wang, S. P. Kim, H. M. Kim, W. H. Lee, C. Hu, J. Y. Bae, E. S. Sim, Y.-C. Chung, J.-H. Jang, *et al.*, "Poly (fluorenyl aryl piperidinium) membranes and ionomers for anion exchange membrane fuel cells," *Nature communications*, vol. 12, no. 1, p. 2367, 2021.

[30] J.-Y. Lee, J.-H. Kim, J.-H. Lee, S. Kim, and S.-H. Moon, "Morphologically aligned cation-exchange membranes by a pulsed electric field for reverse electrodialysis," *Environmental science & technology*, vol. 49, no. 14, pp. 8872–8877, 2015.

[31] B. Motealleh, Z. Liu, R. I. Masel, J. P. Sculley, Z. R. Ni, and L. Meroueh, "Next-generation anion exchange membrane water electrolyzers operating for commercially relevant lifetimes," *International journal of hydrogen energy*, vol. 46, no. 5, pp. 3379–3386, 2021.

[32] N. Chen, S. Y. Paek, J. Y. Lee, J. H. Park, S. Y. Lee, and Y. M. Lee, "High-performance anion exchange membrane water electrolyzers with a current density of 7.68 a cm- 2 and a durability of 1000 hours," *Energy & environmental science*, vol. 14, no. 12, pp. 6338–6348, 2021.

[33] M. Al-Breiki and Y. Bicer, "Liquified hydrogen vs. liquified renewable methane: Evaluating energy consumption and infrastructure for sustainable fuels," *Fuel*, vol. 350, p. 128779, 2023.

[34] A. Midilli, H. Kucuk, M. E. Topal, U. Akbulut, and I. Dincer, "A comprehensive review on hydrogen production from coal gasification: Challenges and opportunities," *International Journal of Hydrogen Energy*, vol. 46, no. 50, pp. 25385–25412, 2021.

[35] C. Lea, "Derbyshire's oil and refining history: the james 'paraffin' young connection," 2018.

[36] J. Ockershausen, "The valley that changed the world: visiting the drake well museum," *Pennsylvania Heritage Magazine*, vol. 21, no. 3, 1995.

[37] IOGP, "Oil in everyday life," 2024.

[38] D. E. Kissel *et al.*, "The historical development and significance of the haber bosch process," *Better Crops With Plant Food*, vol. 98, no. 2, p. 31, 2014.

[39] IPCC, "Climate change 2021: The physical science basis. summary for policymakers," ipcc sixth assessment report (ar6), Intergovernmental Panel on Climate Change, 2023.

[40] Copernicus, "Copernicus: 2023 hottest year on record," 2023.

[41] J. Wise, "Climate change: Window to act is closing rapidly, warn scientists," 2023.

[42] A. Ruiz, "45 carbon dioxide, greenhouse gas climate change statistics," 2023.

[43] QERY, "Renewable energy capacity tracker," 2023.

[44] H. Eroğlu, E. Cuce, P. M. Cuce, F. Gul, and A. Iskenderoğlu, "Harmonic problems in renewable and sustainable energy systems: A comprehensive review," *Sustainable Energy Technologies and Assessments*, vol. 48, p. 101566, 2021.

[45] P. Balakumar and S. Sathiya, "Demand side management in smart grid using load shifting technique," in *2017 IEEE International conference on electrical, instrumentation and communication engineering (ICEICE)*, pp. 1–6, IEEE, 2017.

[46] B. Urishev, "Decentralized energy systems, based on renewable energy sources," *Applied Solar Energy*, vol. 55, pp. 207–212, 2019.

[47] L. Asri, W. Ariffin, A. Zain, J. Nordin, and N. Saad, "Comparative study of energy storage systems (esss)," in *Journal of Physics: Conference Series*, vol. 1962, p. 012035, IOP Publishing, 2021.

[48] J. M. Moradi-Shahrbabak, Zahra lam, "A new index for techno-economical comparison of storage technologies considering effect of self-discharge," *IET Renewable Power Generation*, vol. 17, no. 7, pp. 1699–1712, 2023.

[49] IEA, "Grid-scale storage," 2023.

[50] U. Bossel, "Hydrogen economy: What future?," in *Current Trends and Future Developments on (Bio-) Membranes*, pp. 421–451, Elsevier, 2020.

[51] IEA(2023), "Global hydrogen review 2023, iea, paris," 2023.

[52] Z. Du, C. Liu, J. Zhai, X. Guo, Y. Xiong, W. Su, and G. He, "A review of hydrogen purification technologies for fuel cell vehicles," *Catalysts*, vol. 11, no. 3, p. 393, 2021.

[53] X. Y. Chen, L. X. Wei, L. Deng, F. S. Yang, and Z. X. Zhang, "A review on the metal hydride based hydrogen purification and separation technology," *Applied Mechanics and Materials*, vol. 448, pp. 3027–3036, 2014.

[54] G. AlZohbi, A. Almoaikel, and L. AlShuhail, "An overview on the technologies used to store hydrogen," *Energy Reports*, vol. 9, pp. 28–34, 2023.

[55] J.-Q. Li, Y. Chen, Y. B. Ma, J.-T. Kwon, H. Xu, and J.-C. Li, "A study on the joule-thomson effect of during filling hydrogen in high pressure tank," *Case Studies in Thermal Engineering*, vol. 41, p. 102678, 2023.

[56] A. Elgowainy, K. Reddi, E. Sutherland, and F. Joseck, "Tube-trailer consolidation strategy for reducing hydrogen refueling station costs," *International journal of hydrogen energy*, vol. 39, no. 35, pp. 20197–20206, 2014.

[57] H. Ritchie, "Sector by sector: where do global greenhouse gas emissions come from?," *Our World in Data*, 2020. https://ourworldindata.org/ghg-emissions-by-sector.

[58] IRENA, "Hydrogen: Overview," 2023.

[59] J. N. M. W. Chiara Gulli, Bernd Heid and M. Wilthaner, "Global energy perspective 2023: Hydrogen outlook, mckinsey energy solutions," 2024.

[60] E. Commission, "European hydrogen bank pilot auction: 132 bids received from 17 european countries," 2024.

[61] T. Smolinka, H. Bergmann, J. Garche, and M. Kusnezoff, "The history of water electrolysis from its beginnings to the present," in *Electrochemical power sources: fundamentals, systems, and applications*, pp. 83–164, Elsevier, 2022.

[62] M. El-Shafie, "Hydrogen production by water electrolysis technologies: a review," *Results in Engineering*, p. 101426, 2023.

[63] A. S. Emam, M. O. Hamdan, B. A. Abu-Nabah, and E. Elnajjar, "A review on recent trends, challenges, and innovations in alkaline water electrolysis," *International Journal of Hydrogen Energy*, vol. 64, pp. 599–625, 2024.

[64] S. A. Lee, J. Kim, K. C. Kwon, S. H. Park, and H. W. Jang, "Anion exchange membrane water electrolysis for sustainable large-scale hydrogen production," *Carbon Neutralization*, vol. 1, no. 1, pp. 26–48, 2022.

[65] C. V. Pham, D. Escalera-López, K. Mayrhofer, S. Cherevko, and S. Thiele, "Essentials of high performance water electrolyzers–from catalyst layer materials to electrode engineering," *Advanced energy materials*, vol. 11, no. 44, p. 2101998, 2021.

[66] D. Hua, J. Huang, E. Fabbri, M. Rafique, and B. Song, "Development of anion exchange membrane water electrolysis and the associated challenges: A review," *ChemElectroChem*, vol. 10, no. 1, p. e202200999, 2023.

[67] B. Huang, C. Lei, X. Sun, L. Luo, G. Wang, L. Zhuang, and L. Xiao, "Improving mass transfer in anion exchange membrane water electrolysis by ordered gas diffusion layer," *International Journal of Hydrogen Energy*, vol. 48, no. 91, pp. 35453–35462, 2023.

[68] N. Du, C. Roy, R. Peach, M. Turnbull, S. Thiele, and C. Bock, "Anion-exchange membrane water electrolyzers," *Chemical reviews*, vol. 122, no. 13, pp. 11830–11895, 2022.

[69] C. G. Arges and L. Zhang, "Anion exchange membranes' evolution toward high hydroxide ion conductivity and alkaline resiliency," *ACS Applied Energy Materials*, vol. 1, no. 7, pp. 2991–3012, 2018.

[70] W. Song, X. Zhang, C. Yang, Z. Yang, L. Wu, X. Ge, and T. Xu, "Alkaline membranes toward electrochemical energy devices: recent development and future perspectives," *ACS Central Science*, vol. 9, no. 8, pp. 1538–1557, 2023.

[71] A. Caprì, I. Gatto, C. Lo Vecchio, S. Trocino, A. Carbone, and V. Baglio, "Anion exchange membrane water electrolysis based on nickel ferrite catalysts," *ChemElectroChem*, vol. 10, no. 1, p. e202201056, 2023.

[72] J.-H. Kim, S. Ryu, J.-Y. Lee, and S.-H. Moon, "Preparation of high-conductivity qppo (quaternary-aminated poly (2, 6-dimethyl-1, 4-phenyleneoxide)) membranes by electrical treatment," *Journal of membrane science*, vol. 553, pp. 82–89, 2018.

[73] N. Chen, C. Hu, H. H. Wang, J. H. Park, H. M. Kim, and Y. M. Lee, "Chemically & physically stable crosslinked poly (aryl-co-aryl piperidinium) s for anion exchange membrane fuel cells," *Journal of Membrane Science*, vol. 638, p. 119685, 2021.

[74] X. Wu, N. Chen, H.-A. Klok, Y. M. Lee, and X. Hu, "Branched poly (aryl piperidinium) membranes for anion-exchange membrane fuel cells," *Angewandte Chemie*, vol. 134, no. 7, p. e202114892, 2022.

[75] K. Mark, "Titration of a newtown creek environmental water sample to determine the amount of chloride ions [chemistry]," 2019.

[76] Wikipedia, "Differential scanning calorimetry," 2024.

[77] S. Affolter, A. Ritter, and M. Schmid, "Interlaboratory tests on polymers by differential scanning calorimetry (dsc): determination of glass transition temperature (tg)," *Macromolecular Materials and Engineering*, vol. 286, no. 10, pp. 605–610, 2001.

[78] S. Ebnesajjad, "Surface and material characterization techniques," in *Handbook of adhesives and surface preparation*, pp. 31–48, Elsevier, 2011.

[79] D. Johnson, D. Oatley-Radcliffe, and N. Hilal, "Atomic force microscopy (afm)," in *Membrane characterization*, pp. 115–144, Elsevier, 2017.

[80] Metrohm, "Booster 10a," 2023.

[81] N. Elgrishi, K. J. Rountree, B. D. McCarthy, E. S. Rountree, T. T. Eisenhart, and J. L. Dempsey, "A practical beginner's guide to cyclic voltammetry," *Journal of chemical education*, vol. 95, no. 2, pp. 197–206, 2018.

[82] T. W. Napporn, Y. Holade, B. Kokoh, S. Mitsushima, K. Mayer, B. Eichberger, and V. Hacker, "Electrochemical measurement methods and characterization on the cell level," in *Fuel Cells and Hydrogen*, pp. 175–214, Elsevier, 2018.

[83] R. Hancke, T. Holm, and Ø. Ulleberg, "The case for high-pressure pem water electrolysis," *Energy Conversion and Management*, vol. 261, p. 115642, 2022.

[84] S. Li, Y. Zhu, D. Min, and G. Chen, "Space charge modulated electrical breakdown," *Scientific reports*, vol. 6, no. 1, p. 32588, 2016.

[85] Z.-H. Shen, J.-J. Wang, J.-Y. Jiang, S. X. Huang, Y.-H. Lin, C.-W. Nan, L.-Q. Chen, and Y. Shen, "Phase-field modeling and machine learning of electric-thermal-mechanical breakdown of polymer-based dielectrics," *Nature communications*, vol. 10, no. 1, p. 1843, 2019.

[86] L. De Nardo and S. Farè, "Dynamico-mechanical characterization of polymer biomaterials," in *Characterization of Polymeric Biomaterials*, pp. 203–232, Elsevier, 2017.